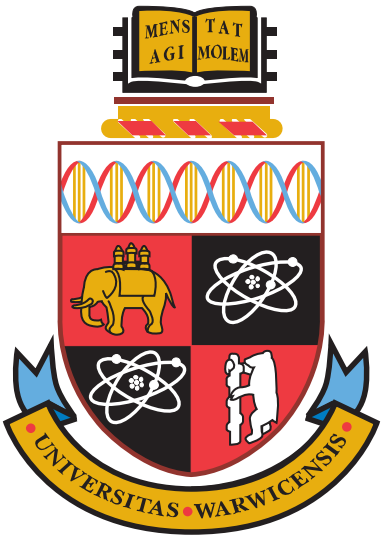

Magnetic properties of the $M_3V_2O_8$ compounds

by

Nicola R. Wilson

Thesis

Submitted to the University of Warwick

for the degree of

Doctor of Philosophy

Department of Physics

October 2007

THE UNIVERSITY OF
WARWICK

Contents

List of Figures

List of Tables

Acknowledgments

First and foremost, I would like to thank my supervisor Oleg Petrenko for his support, patience and encouragement. I have very much enjoyed working with you, and the rest of the S&M Group: Don Paul, Geetha Balakrishnan and Martin Lees. Thanks to Geetha for all of the crystal growth help, and to Martin for all of his help in the labs, and his pedantic proof reading of all of my posters! My gratitude also goes to all of the students of the S&M Group, past and present, and our technician Tom. Sonya, Jenny, Andrew, Dan, and recently Catherine and Tom, you have all made the mezzanine a fun and supportive place to work.

I am grateful to all of my local contacts and collaborators (Laurent Chapon, Björn Fåk, Pascal Manuel, Jean-Michel Mignot and Garry McIntyre) for their valued help in running experiments. Particularly, I would like to thank Laurent for his extensive efforts in teaching me how to refine my data.

I would also like to thank my family: Mum, Dad, Hazel and Rob for their support. Special thanks go to Martin for his support, for proof reading my entire thesis, and for being my personal LaTeX helpline!

Declarations

The work presented in this thesis was carried out by me except where explicitly stated. All of the work took place between September 2004 to October 2007 and was carried out at the University of Warwick Physics Department, the ISIS facility at the Rutherford-Appleton Laboratory, the Institut Laue Langevin and the Laboratoire Leon Brillouin (LLB). All large scale facility experiments were performed with the assistance of a local contact, where I was either the sole experimentalist or a leading member of the experimental team. The LLB experiments were performed in collaboration with Dr. Björn Fåk (Sections 4.5 and 5.4). All Rietveld refinements were performed under the guidance of Dr. Laurent C. Chapon. The refinements performed on the GEM data in an applied field were started by me, but completed by Dr. Chapon (Section 4.3.2). The specific heat measurements only of $Co_3V_2O_8$ taken in applied fields were performed by Dr. Oleg A. Petrenko before the start of my PhD (Figure 4.7).

No part of this thesis has been submitted for examination at any other institute. Parts of the work described in this thesis have been published in the following articles:

- N. R. Wilson, O. A. Petrenko and G. Balakrishnan, *J. Phys.: Condens. Matter*, 19:145257, 2007.
- N. R. Wilson, O. A. Petrenko and L. C. Chapon, *Phys. Rev. B*, 75:094432, 2007.
- N. R. Wilson, O. A. Petrenko, G. Balakrishnan, P. Manuel and B. Fåk, *J. Magn. Magn. Mater.*, 310:1334, 2007.

Abstract

The Kagomé lattice is a very important structure in the field of frustrated magnetism. The lattice has a two dimensional corner-sharing triangular structure, which creates macroscopic degeneracy when combined with antiferromagnetic interactions. Experimentally it is difficult to find a perfect example of this lattice. $Ni_3V_2O_8$ and $Co_3V_2O_8$ are the first compounds found to adopt a buckled version of the Kagomé lattice by their magnetic atoms, called the Kagomé staircase. The staircase lattice differs from the two dimensional lattice in a number of ways: the magnetic layers have lower symmetry and the further neighbour interactions, with the resulting anisotropic exchange interactions, become more important. These factors cause the relief of geometrical frustration and establish long-range magnetic order.

Powders and large single crystals, both of very high quality, of these compounds have been prepared. Magnetisation and specific heat measurements have been used to produce the magnetic field vs temperature phase diagrams and neutron diffraction has been used to determine the different magnetic structures present in the materials. Inelastic neutron scattering was also employed to investigate the magnetic excitations of the systems.

$Co_3V_2O_8$ possesses a very complex phase diagram where the sequence of the phase transitions is of particular interest. The system has two main phases below 11 K: a spin density wave structure with $\mathbf{k} = (0,\ \delta,\ 0)$, where δ varies around $\frac{1}{2}$ above 6 K and a commensurate $\mathbf{k} = 0$ ferromagnetic structure below. The narrow region between 5.8 and 6.1 K in zero applied field was found to have Bragg peaks at positions forbidden by c-centring symmetry restrictions. Diffraction measurements in an applied field uncovered a further magnetic structure not found in zero field. Multiple magnetic excitations have been observed using inelastic neutron scattering measurements on powder and single crystals. Below 5 meV, four excitations branches were observed and a further collection of at least five branches were seen between 10 meV and 68 meV in energy transfer.

The phase diagram of $Ni_3V_2O_8$ shows that four magnetic phases exist in this material in applied fields of up to 120 kOe. On cooling, the material is paramagnetic then enters a high temperature incommensurate phase, next is a low temperature incommensurate phase, then a commensurate antiferromagnetic phase, and finally a very similar commensurate phase where a slight increase of the magnetic moments is observed. The inelastic measurements have detected up to five excitation branches below 6 meV. They also show that the quasi-elastic scattering is $\mathbf{Q}$ dependent in the incommensurate phases of the material.

Abbreviations

C: Commensurate phase found in $Ni_3V_2O_8$ between 2 and 4 K

C': Commensurate phase found in $Ni_3V_2O_8$ below 2 K

EDX: Electron dispersive X-ray analysis

HTI: High temperature incommensurate phase found in $Ni_3V_2O_8$ between 6 and 9.1 K

HT_{inc}: High temperature incommensurate phase found in $Co_3V_2O_8$ between 6 and 11 K, surrounds the $HT_{\delta=\frac{1}{2}}$ phase

$HT_{\delta=\frac{1}{2}}$: High temperature antiferromagnetic commensurate phase found in $Co_3V_2O_8$ between 8.7 and 6.7 K

LTI: Low temperature incommensurate phase found in $Ni_3V_2O_8$ between 4 and 6 K

LT_F: Low temperature ferromagnetic phase found in $Co_3V_2O_8$ below 6 K

PPMS: Physical properties measurement system

SEM: Scanning electron microscope/microscopy

SQUID: Superconducting quantum interference device

VSM: Vibrating sample magnetometer/magnetometry

Note on units

The units used within this thesis are those that are conventionally used in the field of magnetism. Where the units used are not SI units, the conversions are shown below.

$\mathbf{H}$ Magnetic field strength, 1 Oe $= 10^3 \times 4\pi$ A/m

χ Susceptibility, e.g. 1 emu/Oe mol Cobalt $= (4\pi)^2 \times 10^{-13}$ Hm^2/mol Cobalt

Chapter 1

Introduction

1.1 Magnetism

The magnetic properties of materials are the basis for many significant advances in technology. Magnetism is used in motors, hard disks, bank cards, speakers and cathode ray televisions and monitors, to name a few. The first technological use of magnetism was the compass, which has been in used in Western Europe since at least the twelfth century, and in China from at least the eleventh [1]. However, it has been proposed that an artefact from the Olmec people shows that they used a form of compass earlier than 1000 BC [2]. These early devices were made from lodestone, a name given to many iron oxides. The specific oxides used would have been ferro- or ferrimagnetic. Such materials are what most people would commonly think of as magnets: they would stick to a fridge or allow you to pick up paperclips! There are, however, many forms of magnetism which will be introduced in the following sections.

1.1.1 Magnetic moments

Intended here is an introduction to the field of magnetism as a means to understanding the particulars of specific samples. Many texts are available with a more comprehensive covering of the large subject area of magnetism, such as references [3, 4, 5].

The magnetic moment can be derived from the angular momentum of a particle. Using quantum mechanics, the orbital angular momentum $\mathbf{L}$ of an electron is $\hbar\sqrt{l(l+1)}$, where the orbital quantum number $l = 0, 1, 2, 3...$ and $\hbar$ is Planck's constant with a value of 1.054×10^{-34} Js^{-1}. The projected magnitude of the angular momentum along the z direction (the orbit is in the xy plane) is $\hbar m_l$, where the magnetic quantum number $m_l = -l, -l+1, ..., l-1, l$. Because of the charge on an electron, this angular momentum gives rise to a magnetic moment of magnitude $\mu_B\sqrt{l\,(l+1)}$. μ_B is the Bohr magneton and is equal to $\frac{e\hbar}{2m_e}$, where m_e is the mass of an electron. The projection onto the z axis of this magnetic moment is $-\mu_B m_l$.

An electron also possesses an intrinsic angular momentum, as if it were not a point source but a rotating body. This property is know as spin, $\mathbf{S}$, and has a magnitude of $\hbar\sqrt{s(s+1)}$. For an electron, the spin quantum number $s = 1/2$, so $S = \sqrt{3}\hbar/2$. The projection of this angular momentum onto the z axis is $\hbar m_s$, which for an electron equals $\hbar/2$ as $m_s = \pm 1/2$. The magnetic moment associated with this angular momentum component is $\sqrt{3}\mu_B$, and the component along the z axis is $\pm\mu_B$. The total angular momentum $\mathbf{J}$ is the sum of the two angular momentum components $\mathbf{L}$ and $\mathbf{S}$.

1.1.2 Paramagnetism & diamagnetism

An important quantity when considering a magnetic material is the magnetisation. A magnetic material will comprise many individual magnetic moments. The magnetisation, $\mathbf{M}$, is defined as the magnetic moment per unit volume. It is related to the surrounding magnetic field by Equation 1.1, where μ_0 is the permeability of free space with a value of $4\pi \times 10^{-7}$ Hm^{-1}. $\mathbf{H}$ and $\mathbf{B}$ are both vector fields; they are measurements of magnetic field and are related by the factor μ_0. $\mathbf{H}$ is known as the magnetic field strength, and $\mathbf{B}$ is known as the magnetic flux density.

$$\mathbf{B} = \mu_0(\mathbf{H} + \mathbf{M}) \tag{1.1}$$

In the presence of a linear magnetic material, $\mathbf{B}$ is redefined as $\mu_0\mu_r\mathbf{H}$, where μ_r

is the relative permeability of the material. μ_r is equal to $1 + \chi$, where χ is the dimensionless quantity called susceptibility. The susceptibility of a material is its magnetisation divided by the magnetic field $\mathbf{H}$.

All materials have a negative response to a magnetic field; an applied field causes the magnetic moments to align in such a way that opposes that applied field. This is called a diamagnetic response. The susceptibility resulting from this response is given in Equation 1.2 [6]. Z is the atomic number of the atom, N is the number of atoms in the sample, e is the charge on an electron and $< r^2 >$ is the mean square distance of the electrons from the nucleus.

$$\chi_{dia} = -\frac{\mu_0 N Z e^2}{6 m_e} \left\langle r^2 \right\rangle \tag{1.2}$$

Some materials also exhibit a positive susceptibility that overpowers the negative diamagnetic response. This is called paramagnetism. In these systems, an applied magnetic field causes the magnetic moments of ions and atoms to align along the direction of the applied field. This occurs in systems with unpaired electrons, metals, transition elements and even molecular oxygen. These materials contain randomised magnetic moments in zero applied magnetic field. They do not interact strongly enough to align, but instead they are dynamic. When a magnetic field is applied, alignment occurs, dependent upon the strength of the applied field.

The susceptibility in this case is defined in Equation 1.3.

$$\chi_{para} = \frac{N \mu_0 \mu_{\text{eff}}^2}{3 k_B T} = \frac{C}{T} \tag{1.3}$$

k_B is Boltzmann's constant with a value of 1.3807×10^{-23} JK^{-1}, T is the temperature and μ_{eff} is the effective magnetic moment on each of the atoms. The constant C is known as Curie's constant and is often used to determine the effective magnetic moment in a sample from its susceptibility. It leads to the approximation that $\chi \propto 1/T$. This form is an acceptable approximation unless extremely low temperatures or high fields are considered.

The effective moment is related to the angular momentum as shown in Equation 1.4.

$$\mu_{\text{eff}} = g\mu_B \left[\mathbf{J}(\mathbf{J}+1)\right]^{1/2} \tag{1.4}$$

Where the g factor is given by the Landé Equation:

$$g = 1 + \frac{\mathbf{J}(\mathbf{J}+1) + \mathbf{S}(\mathbf{S}+1) - \mathbf{L}(\mathbf{L}+1)}{2\mathbf{J}(\mathbf{J}+1)} \tag{1.5}$$

For an electron, $g = 2.0023$, but is usually approximated to 2.

1.1.3 Spin interactions

Magnetic moments may interact through numerous different methods. These interactions can then give rise to a multitude of different magnetic structures in a system. The most basic interaction is the magnetic dipolar interaction. This is, however, a weak effect in a material when considering the separation and typical size of moments on atoms or ions. A much larger effect comes from exchange interactions between spins. Equation 1.6 gives the Heisenberg Hamiltonian for any spin system.

$$\mathscr{H} = -\sum_{ij} J_{ij}\mathbf{S}_i \cdot \mathbf{S}_j \tag{1.6}$$

J_{ij} is the exchange constant (or integral) for the system dependent upon the possible states of the two spins i and j. J_{ij} is defined so that a positive value corresponds to a parallel preference between the alignment of the spins, and a negative value to an anti-parallel preference.

If the two interacting moments are from electrons on the same atom, the exchange constant results in favouring the triplet state and reducing the Coulomb repulsion. This separates the parallel aligned spins and satisfies Hund's first rule. If the moments are from neighbouring atoms, the resulting exchange constant is most likely to be negative, preferring anti-parallel alignments of spins. Such an interaction is known as direct exchange, but is not often responsible for the formation of long-range magnetic order. This is because the orbitals of the electrons involved are mostly too localised to

overlap sufficiently. Indirect exchange is the next step in considering exchange paths, the most common form is known as superexchange. Such interactions are extended by non-magnetic intermediary atoms, often oxygen. These interactions can be favourable due to a reduction in the kinetic energy when the electrons involved are delocalised over the group of two magnetic and one non-magnetic atoms. The strength of the interaction is dependent upon the angle that this group makes along with the orbital symmetry and electron configuration of all atoms in the group.

The last exchange path to be considered here is that of the anisotropic exchange interaction, also know as the Dzyaloshinsky-Moriya interaction [7]. This path stems from an interaction between the spin and orbital components of electrons' wave functions. It introduces the term shown in Equation 1.7 into the Hamiltonian.

$$\mathscr{H}_{DM} = -\sum_{ij} \mathbf{D} \cdot \mathbf{S}_i \times \mathbf{S}_j \tag{1.7}$$

Depending on the symmetry relation of the magnetic ions, $\mathbf{D}$ can only exist parallel or perpendicular to the line connecting the ions. The interaction aims to produce a negative energy contribution by aligning the spins at 90° to each other within the plane perpendicular to $\mathbf{D}$. This is usually not the most significant interaction in a system, but can result in canting the magnetic moments by a small amount.

Other forms of indirect exchange can also be observed, such as the RKKY interaction in metals. This occurs when the conduction electrons are the intermediary between the magnetic ions. One further route of exchange is that of double exchange. This can happen when magnetic ions show mixed valency. These mechanisms do not, however, need to be considered for the materials studied here.

1.1.4 Long-range magnetic order

The most well known magnetic structure is ferromagnetism, which occurs when J_{ij} is positive. Here, all magnetic moments align in the same direction, as shown in Figure 1.1. The material has a net magnetic moment below a certain temperature even in zero

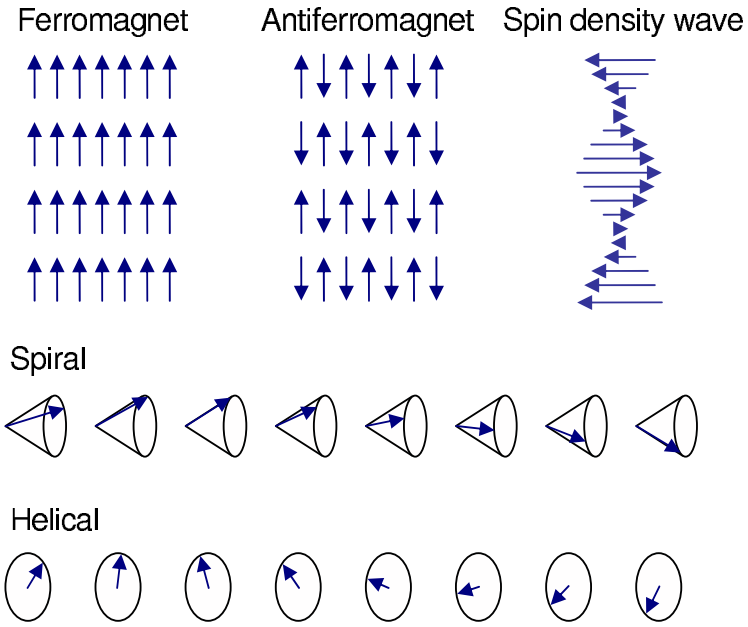

Figure 1.1: Various possible magnetic structures with long-range order, the spins are represented by arrows indicating their orientation. Image reproduced from Fig. 5.1 of reference [3].

applied field. In an applied field, $\mathbf{B}$, an extra term is required to solve the Hamiltonian of the system as shown in Equation 1.8.

$$\mathscr{H}_{mag} = -\sum_{ij} J_{ij}\mathbf{S}_i \cdot \mathbf{S}_j + g\mu_B \sum_j \mathbf{S}_j \cdot \mathbf{B} \tag{1.8}$$

The new term added to the exchange contribution is the Zeeman energy - the energy of an electron in a magnetic field.

Above a particular temperature, thermal fluctuations break down the magnetic order in a ferromagnet. This transition temperature is know as the Curie temperature, T_C. The susceptibility curve of a ferromagnet tends to infinity at T_C on reducing the temperature. Above T_C in the paramagnetic phase of a material, the susceptibility is described by the Curie-Weiss dependence,

$$\chi \propto \frac{1}{T-\theta}. \tag{1.9}$$

Therefore, plotting $1/\chi$ against T will give the Weiss temperature, θ, as the x-intercept. For an ideal ferromagnet, this is a positive value equal to T_C, and for a paramagnet, $\theta = 0$. The value will be negative for an antiferromagnet.

The structure of an antiferromagnet comprises spins oriented anti-parallel to their nearest neighbour, as shown in Figure 1.1. Antiferromagnets have a negative value of J_{ij} and no net magnetisation in zero applied field. The susceptibility of an antiferromagnet is dependent upon the direction of the applied field. The temperature at which thermal fluctuations no longer dominate and magnetic order is achieved is known as T_N. The susceptibility will increase and reach a maximum at T_N. If the field is parallel to the direction of the spins, χ then reduces to zero with decreasing temperature. If the field is perpendicular to the spins then χ remains constant with reducing temperature.

These are the most basic forms of long-range magnetic order, many more complicated structures exist. The next logical step is that the moments are not all of the same magnitude, meaning that an antiferromagnet can have a net magnetisation. This kind of structure is known as ferrimagnetism and is found in the ferrite compounds with chemical formula $MOFe_2O_3$ where M is Zn^{2+}, Co^{2+}, Fe^{2+}, Ni^{2+}, Cu^{2+} or Mn^{2+}, amongst others. Other more complex structures involve rotation and modulation of the spins such as that found in the spiral, helical and spin density wave structures shown in Figure 1.1.

1.1.5 Phonons & magnons

At any finite temperature the atoms in a lattice will undergo thermal vibrations. These vibrations are quantised into discrete packets called phonons; they have angular frequency ω that is proportional to the wave vector $\mathbf{q}$, at low values of $\mathbf{q}$. As long as the wavelength of the phonon is long enough, it takes only an infinitesimal amount of energy to be produced. These acoustic phonons are the Goldstone modes of the system [8]. Another kind of phonon can be also be produced, called the optical phonon. These modes have an energy gap and often the energy ($\hbar\omega$) is less variable with momentum

($\hbar\mathbf{q}$) than in an acoustic mode. The two modes are distinguished by comparison of their $\omega(\mathbf{q})$ dispersion relation.

The equivalent excitations also appear in spin systems. These excitations are termed spin waves and are quantised into magnons. For the simple model of a one dimensional chain of ferromagnetic moments separated by a, ω is related to $\mathbf{q}$ as shown in Equation 1.10.

$$\hbar\omega = 4\mathbf{JS}(1 - \cos\mathbf{q}a) \tag{1.10}$$

For an isotropic ferromagnet, there is no energy gap in the dispersion relation of a magnon. However, many systems are not perfectly isotropic and this introduces a gap into the dispersion.

1.2 Frustrated magnetism

So far, only simple examples of structures on a cubic lattice have been given. Complications arise when different lattice types are considered or interaction types are mixed. For example, consider antiferromagnetic exchange interactions on a triangular lattice. The most basic example of just one triangle with an Ising spin on each vertex is given in Figure 1.2. The interactions between each of these spins cannot be satisfied. The system has degenerate ground states and is said to be frustrated.

Frustration occurs on many different lattices, most often based on triangles. When the form of the lattice causes the degeneracy in a material, the effect is known as geometric frustration [9]. Even when the assumptions are relaxed to allow Heisenberg moments (three dimensional), frustration still occurs. Frustrated magnets are known to exist with structures such as the three dimensional pyrochlore lattice based on linked tetrahedra, and the two dimensional Kagomé lattice based on linked triangles, both shown in Figure 1.3. The most simple solution of frustrated XY moments (two dimensional) on a triangular lattice is the 120° model, where the three moments in each triangle all point at 120° from each other [10]. However, this simple model can not

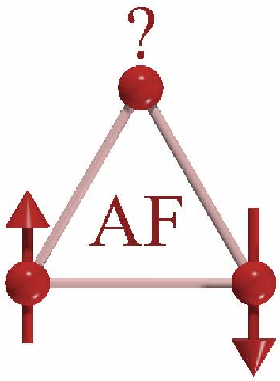

Figure 1.2: The magnetic structure due to antiferromagnetic interactions on a triangular lattice with Ising spins can not be solved singularly. Such a system is degenerate and is called a frustrated magnet.

be applied to the Kagomé and pyrochlore structures. These materials are particularly prone to frustration due to the corner-sharing, rather than edge-sharing basis of their structures.

The frustration in magnetic systems means that many will never achieve long-range magnetic order. Many highly frustrated systems form spin glass structures where the moments are frozen into a disordered state, usually at very low temperatures. Some materials maintain fluctuations down to zero temperature and never reach a transition to a frozen state; these materials are known as spin liquids [11]. Even more exotic is the special case known as the spin ice [12]. This is a spin liquid comprising Ising spins on a pyrochlore structure - analogous to protons around an O atom in hexagonal water ice. An example of a spin ice is $Ho_2Ti_2O_7$ [13]. In this material, local Ising anisotropy leads to a predominantly static, geometrically frustrated ground state.

Disorder and frustration can also be introduced through other means, not just through geometric considerations. One well-studied cause is site randomness, where the materials are known as dilute spin glasses. For example, if Cu is doped with small

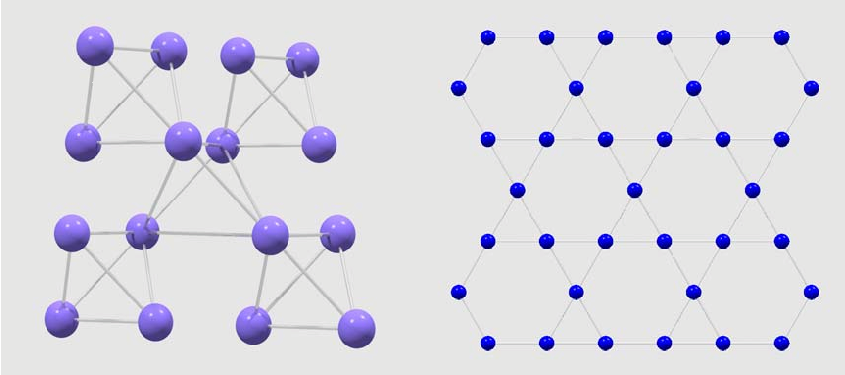

Figure 1.3: The structures of the three dimensional pyrochlore (left) and two dimensional Kagomé (right) lattices.

amounts of Mn which are placed randomly with no short range order then the material is frustrated and undergoes a spin glass transition [14, 15]. Spin glasses can also be caused by bond randomness where the interactions between moments vary. This can be due to the material possessing more than one type of magnetic atom, such as $Rb_2Cu_{1-x}Co_xF_4$ [16] which contains both Co and Cu. This material is a physical realisation of the theoretical Edwards-Anderson model of frustration that involves mixed antiferromagnetic and ferromagnetic interactions on a cubic lattice [17].

Many materials that have properties capable of causing frustration do actually achieve long-range magnetic order. One family of Kagomé materials that contains some ordered systems are the jarosites with $AB_3(SO_4)_2(OH)_6$ where A=Na^+, K^+, Rb^+, Ag^+, H_3O^+ or $\frac{1}{2}Pb^{2+}$ and B=Fe^{3+}, Cr^{3+} or V^{3+} [18]. The samples in this series that achieve long-range magnetic order are B=Fe^{3+} [19] with A=Na^+, K^+ [20], Rb^+, Ag^+ and ND_4^+ [21]. The order is believed to derive from complications in the magnetic structure arising from further neighbour interactions; the most predominant of which are actually the interplane exchange interactions.

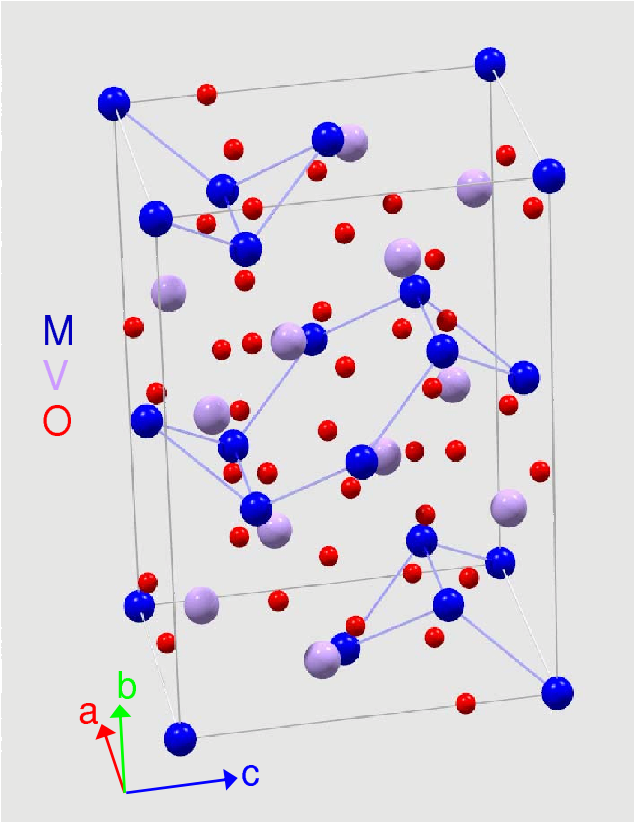

Figure 1.4: The atomic structure of the Kagomé staircase compounds is shown. The space group is Cmca, number 64. The magnetic atoms are the largest, shown in dark blue, the O atoms are the smallest in red and the V atoms are purple.

1.3 Kagomé staircase systems

Recently, a new class of frustrated magnets named the Kagomé staircase materials, has become a central point of intensive investigations [22, 23, 24, 25, 26, 27, 28, 29, 30, 31][1]. These compounds, of formula $M_3V_2O_8$ (M=Ni, Co, Cu, Mn or Zn), present an exchange topology closely related to the Kagomé lattice. In these staircase oxides, layers of edge-sharing MO_6 octahedra are separated by non-magnetic VO_4 tetrahedra. The structure

[1]Reference [22] uses the space group Acam to describe the structure of $Co_3V_2O_8$ and $Ni_3V_2O_8$ so the a and c-axes are swapped when compared to the definition used in this thesis and other publications.

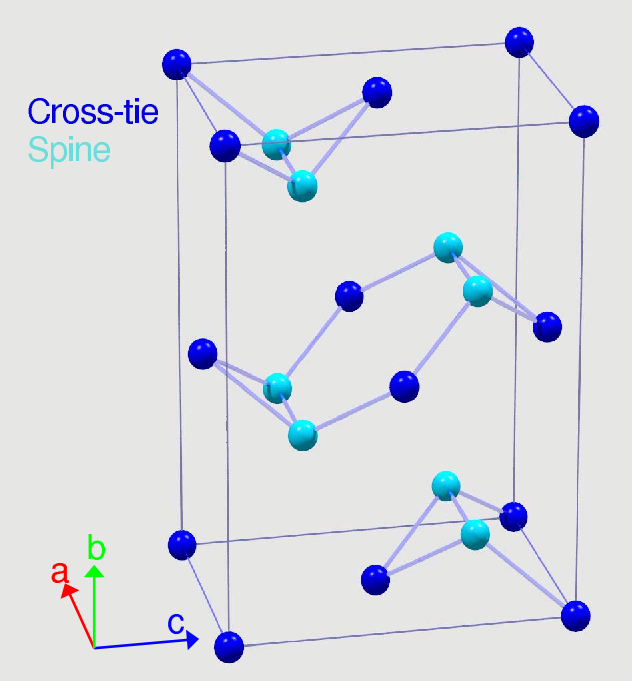

Figure 1.5: The atomic structure of the magnetic atoms in the Kagomé staircase systems. The cross-tie sites are shown in dark blue, and the spine site are in light blue.

of these materials is shown in Figure 1.4. The space group is Cmca (number 64), giving the material a c-centred orthorhombic structure. The specific chemical bonding in these materials creates Kagomé layers of magnetic M^{2+} ions (the V^{5+} ions are non-magnetic) buckled into a staircase formation – hence the so-called Kagomé staircase lattice [26]. The unit cell with just the magnetic M atoms is presented in Figure 1.5. This figure shows the two crystallographically different M sites, called the cross-tie and spine sites. The remainder of the unit cell comprises one V site and three O sites. The magnetic layers found in this structure have lower symmetry than that found in the two dimensional Kagomé lattice which, combined with next-nearest neighbour interactions and possible anisotropic exchange, partially releases the geometrical frustration.

Here will be presented a study of the two materials $Co_3V_2O_8$ and $Ni_3V_2O_8$. The atomic positions in these materials were determined by Sauerbrei *et al.* in 1973 [32].

These positions are given in Table 1.1. The lattice parameters as found by Sauerbrei *et al.* are:

	$Co_3V_2O_8$ (Å)	$Ni_3V_2O_8$ (Å)
a	6.030(4)	5.936(4)
b	11.486(2)	11.420(6)
c	8.312(5)	8.240(5)

The electronic structure of Co^{2+} is [Ar] $3d^7$ $4s^2$, and the structure of Ni^{2+} is [Ar] $3d^8$ $4s^2$. The site symmetry and co-ordinates of the atoms are given in Table 1.2. There are 12 magnetic atoms per unit cell, and 52 atoms in total. The magnetic atoms lie within octahedra of O atoms which are different for the two sites. The octahedra are both distorted in complex manners, as shown for $Co_3V_2O_8$ in Figure 1.6. In this material, the cross-tie site atom lies in the plane with four oxygen atoms of type O3, separated from each by 2.13 Å. The angles O3-Co_{ct}-O3 are 99° and 81°. Above and below the plane are two O2 atoms, the connecting vector lies at 180° to the plane of the O3 atoms. The Co_{ct}-O2 bond length is 2.04 Å. The spine site octahedra distortions are more complicated. Co_s is surrounded by two of each O type, O1, O2 and O3. The magnetic atom lies within the plane of the O1 and O2 atoms which form a rectangle with the Co_s offset below the centre. Above and below Co_s the angles formed with the oxygen are 95° and 91°. To either side the angles are both 87°. The bond lengths are 2.07 Å to the O1 atoms and 2.17 Å to the O2 atoms. The out-of-plane O3 atoms form an angle of 174° with the Co_s site. These bond lengths are 2.12 Å. The nearest neigbour bonds are Co_{ct}-Co_s and Co_s-Co_s which have lengths of 2.98 Å and approximately 3 Å respectively. The numbers for $Ni_3V_2O_8$ are almost identical as the atomic positions in the two samples only differ by up to 2%.

A recent development in this field is the study of compounds formed from a mixture of $Ni_3V_2O_8$ and $Co_3V_2O_8$ [30], and also the study of $Mn_3V_2O_8$ [31]. The material β-$Cu_3V_2O_8$ has been researched by laboratory magnetisation and specific heat measurements [29]. However, this material is exceedingly difficult to manufacture; to produce and maintain this structural form of $Cu_3V_2O_8$ at standard temperature and

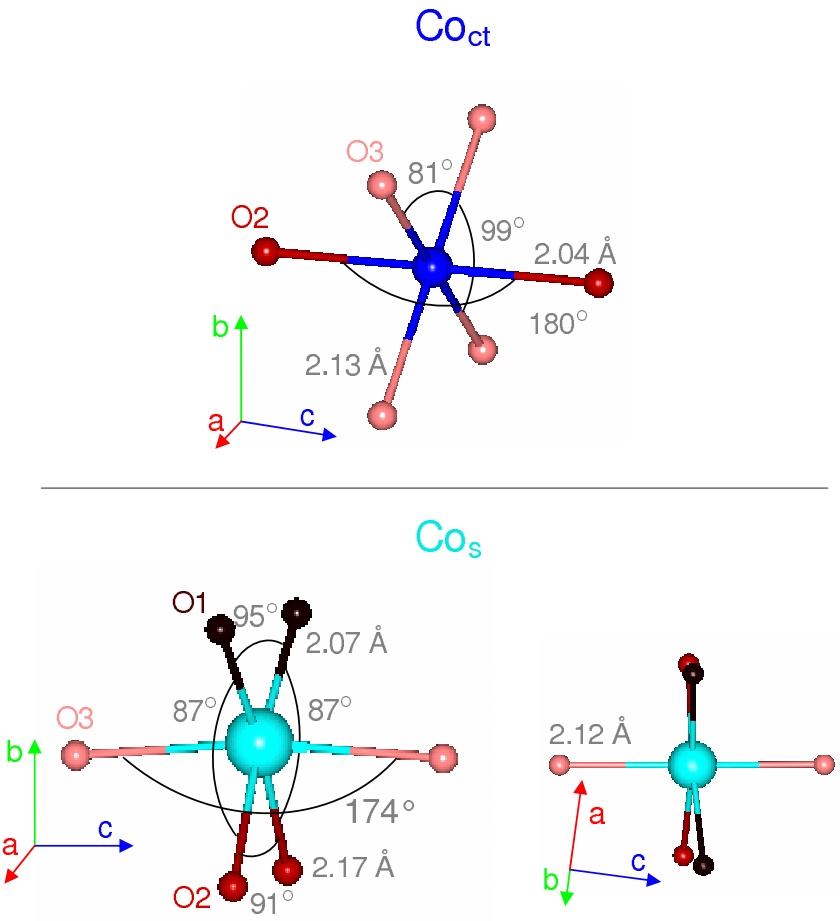

Figure 1.6: The distorted octahedra surrounding the magnetic atoms in $Co_3V_2O_8$. The two sites, Co_{ct} and Co_s, sit in different octahedra. The Co_s site octahedra is most distorted as can be seen in the rotated view of the structure.

$Co_3V_2O_8$

Atom	x	y	z
Co_{ct}	0	0	0
Co_s	1/4	0.1329(1)	1/4
V	0	0.3773(1)	0.1204(1)
O(1)	0	0.2503(4)	0.2290(6)
O(2)	0	0.0010(4)	0.2447(6)
O(3)	0.2703(7)	0.1185(2)	0.9983(4)

$Ni_3V_2O_8$

Atom	x	y	z
Ni_{ct}	0	0	0
Ni_s	1/4	0.13024(3)	1/4
V	0	0.37623(4)	0.11965(7)
O(1)	0	0.2486(2)	0.2309(3)
O(2)	0	0.0013(2)	0.2448(3)
O(3)	0.26663(3)	0.1189(1)	0.0003(3)

Table 1.1: The atomic positions for $Co_3V_2O_8$ and $Ni_3V_2O_8$ with errors in the last digit given in parentheses. For the magnetic Co and Ni atoms, the subscripts ct and s stand for cross-tie and spine respectively. The positions were determined by Sauerbrei *et al.* [32].

pressure requires an environment of 30-40 kbar and 900°C [33]. These difficulties explain the lack of results on this particular compound.

1.3.1 $Co_3V_2O_8$

When this thesis work was started, the scientific community had just begun their study of the magnetic properties of the $Ni_3V_2O_8$ and $Co_3V_2O_8$ systems [22, 26]. Their initial investigations showed the materials to achieve magnetic order through a series of transitions, which, considering the complexity and triangular basis of the structure, must indicate strongly competing interactions. Initial susceptibility measurements showed $Co_3V_2O_8$ to be highly anisotropic; a factor of over 50 was observed between the easy a-axis and hard b-axis. A clear transition is seen in these data at approximately 6 K and two anomalies are observed at 8.2 and 11.2 K.

Atom	Multi-plicity	Wyckoff letter	Site Symm.	Co-ordinates $(0,0,0)+$ $(\frac{1}{2},\frac{1}{2},0)+$			
M_{ct}	4	a	$2/m..$	$0,0,0$	$0,\frac{1}{2},\frac{1}{2}$		
M_s	8	e	$.2.$	$\frac{1}{4},y,\frac{1}{4}$	$\frac{3}{4},\bar{y}+\frac{1}{2},\frac{3}{4}$	$\frac{3}{4},\bar{y},\frac{3}{4}$	$\frac{1}{4},y+\frac{1}{2},\frac{1}{4}$
V	8	f	$m..$	$0,y,z$	$0,\bar{y}+\frac{1}{2},z+\frac{1}{2}$	$0,y+\frac{1}{2},\bar{z}+\frac{1}{2}$	$0,\bar{y},\bar{z}$
O(1)	8	f	$m..$	$0,y,z$	$0,\bar{y}+\frac{1}{2},z+\frac{1}{2}$	$0,y+\frac{1}{2},\bar{z}+\frac{1}{2}$	$0,\bar{y},\bar{z}$
O(2)	8	f	$m..$	$0,y,z$	$0,\bar{y}+\frac{1}{2},z+\frac{1}{2}$	$0,y+\frac{1}{2},\bar{z}+\frac{1}{2}$	$0,\bar{y},\bar{z}$
O(3)	16	g	1	x,y,z $\bar{x},\bar{y},\bar{z}$	$\bar{x},\bar{y}+\frac{1}{2},z+\frac{1}{2}$ $x,y+\frac{1}{2},\bar{z}+\frac{1}{2}$	$\bar{x},y+\frac{1}{2},\bar{z}+\frac{1}{2}$ $x,\bar{y}+\frac{1}{2},z+\frac{1}{2}$	$x,\bar{y},\bar{z}$ $\bar{x},y,z$

Table 1.2: The site symmetry for space group Cmca, 64 [34].

Since these initial publications, the phase diagram of $Co_3V_2O_8$ has been studied extensively [35, 36, 37, 38, 39], and further efforts have been made at crystal growth [40]. Crystals have been studied using laboratory magnetisation and specific heat measurements to determine the phase diagram, neutron diffraction to determine the magnetic structure [23, 27, 41] and inelastic neutron methods to study magnetic excitations [42]. The magneto-capacitance of $Co_3V_2O_8$ has also been studied [43] and results suggest that a structural distortion is induced in the material on application of a magnetic field at temperatures below 30 K.

This thesis presents a detailed study of the phase diagram, diffraction experiments and inelastic neutron scattering measurements. The phase diagram comprises four magnetic structures in zero applied field, and more phases are observed in applied fields. In zero field, the transition temperatures are 11, 8.7, 6.7, 6.1, and 5.8 K, as will be shown in Chapter 4. Upon cooling, the sample enters an incommensurate phase, then passes through a series of locking and unlocking transitions where the structure becomes antiferromagnetic. The material also very briefly enters a phase with magnetic Bragg

peaks at hkl values that are crystallographically forbidden for the c-centred structure ($h + k$=odd). The low temperature phase is ferromagnetic, although on application of a magnetic field this order gives way to a series of complex structures. These structures and the phase diagram will be discussed in much more detail in Chapter 4.

1.3.2 $Ni_3V_2O_8$

The first investigations of $Ni_3V_2O_8$ [22, 26] showed the powder form of the material to have four phase transitions between 2 and 10 K. Since these first investigations, the single crystal phase diagram of the material has been presented [27, 35] and the observed magnetic structures have been explained using theoretical models [25]. These models include nearest-neighbour exchange, next-nearest-neighbour exchange, spin anisotropy, Dzyaloshinsky-Moriya and pseudo-dipolar interactions. The complexity of the material is demonstrated by the need to include so many interaction types in the model. One of the phases observed between 4 and 6 K holds an extra development; it was found to be ferroelectric, and so multiferroic. This was first observed by Lawes *et al.* [28] in 2005, and has since been studied using more and more techniques [43, 44, 45, 46, 47, 48].

The structure of $Ni_3V_2O_8$ was first reported by Sauerbrei *et al.* [32], and single crystals have since been produced by a number of teams [22, 49, 50]. Crystals have been studied using laboratory magnetisation and specific heat measurements [26, 35], neutron diffraction [25, 27], inelastic neutron methods [42] and muon techniques [49]. $Ni_3V_2O_8$ has also been found to have interesting photophysical properties [51].

This thesis presents a detailed study of the phase diagram, diffraction experiments and inelastic neutron scattering measurements. The series of magnetic transitions observed will be discussed in more detail in Chapter 5. In brief, $Ni_3V_2O_8$ has four magnetic phases below 10 K. The transition temperatures for these phases are 9.1, 6, 4 and 2 K. The first two phases found on reducing temperature are incommensurate. The second of these phases has interesting symmetry properties which allow for the development of ferroelectric order. The two lower temperature phases are both commensurate,

the interactions are predominantly antiferromagnetic.

Although the ferroelectric properties of neither $Co_3V_2O_8$ or $Ni_3V_2O_8$ are studied here, it is worth noting this attribute. Recently, a number of materials have been found that develop similar dielectric properties that are associated with a change in magnetic structure [48, 52, 53]. Presented here are purely the magnetic properties of $Ni_3V_2O_8$ and $Co_3V_2O_8$, including results of single crystal growths, laboratory measurements and large scale facility neutron scattering investigations.

Chapter 2

Neutron scattering theory

2.1 Neutron properties

Neutron scattering has become an invaluable tool in the study of condensed matter. The properties of the neutron make it an ideal probe for such systems. The most significant property is undoubtedly the mass of the neutron. When combined with easily achievable velocities, the mass can yield a de Broglie wavelength of the order of interatomic distances. The mass is 1.675×10^{-27} kg and the velocity range used in experiments is very wide, from around 200 to 80000 ms^{-1}.

The neutron comprises three quarks (of flavour up, down and down), so the total charge is zero, and the total spin is $\mathbf{S}_N = \hbar/2$. The neutron penetrates deeply into atoms due to it having no charge. It interacts with the nucleus and is scattered by nuclear forces. The neutron scattering cross-section of an atom is therefore not strongly related to its atomic number. This is the most significant difference between neutron and X-ray scattering experiments. X-rays interact with charged particles, mainly the electrons of an atom. The electron scattering cross-section increases in proportion with the number of electrons in an atom. The interaction strengths for the two techniques can vary hugely in different elements.

As the neutron has spin, it interacts with other spin possessing particles; such

as unpaired electrons. This makes the neutron an ideal probe for magnetic systems.

2.2 Neutron scattering theory

2.2.1 Basic principles

When quantitative analysis of a scattering event is required, the scattering cross-sections (σ) of the materials involved must be considered. The total scattering cross-section, σ_{tot}, is the total number of neutrons scattered per second divided by the incident neutron flux, Φ [54]. σ_{tot} is expressed mathematically in Equation 2.1 using spherical polar co-ordinates θ and ϕ, where dΩ is a solid angle.

$$\sigma_{tot} = \int_{\theta,\phi} \left(\frac{\mathrm{d}\sigma}{\mathrm{d}\Omega}\right) \mathrm{d}\Omega \tag{2.1}$$

$\frac{\mathrm{d}\sigma}{\mathrm{d}\Omega}$ is known as the differential scattering cross-section and is equal to the number of neutrons scattered per second into the solid angle dΩ in the direction (θ, ϕ), divided by the flux, Φ, and solid angle, Ω. In a scattering experiment only a partial solid angle is covered by detectors and only a certain energy range, E' to E'+dE', is detected. Therefore the partial scattering cross-section, $\frac{\mathrm{d}^2\sigma}{\mathrm{d}\Omega \mathrm{d}E_f}$, is the quantity measured during a scattering experiment. The geometry related to this scattering is shown in Figure 2.1.

For now, only the interaction of the neutron with the nuclei of atoms and not the magnetic interaction of the neutron will be considered. The incident neutron can then be described purely by its momentum or wavevector, $\mathbf{k}$. The momentum transfer ($\hbar\mathbf{Q}$) and energy transfer ($\hbar\omega$) of the neutron during a scattering event are described by Equations 2.2 and 2.3 in terms of incident (i) and final (f) momenta/energies. $\mathbf{Q}$ is known as the scattering vector and m is the mass of the neutron.

$$\mathbf{Q} = \mathbf{k}_i - \mathbf{k}_f \tag{2.2}$$

$$\hbar\omega = E_i - E_f = \frac{\hbar^2\mathbf{k}_i^2}{2m} - \frac{\hbar^2\mathbf{k}_f^2}{2m} \tag{2.3}$$

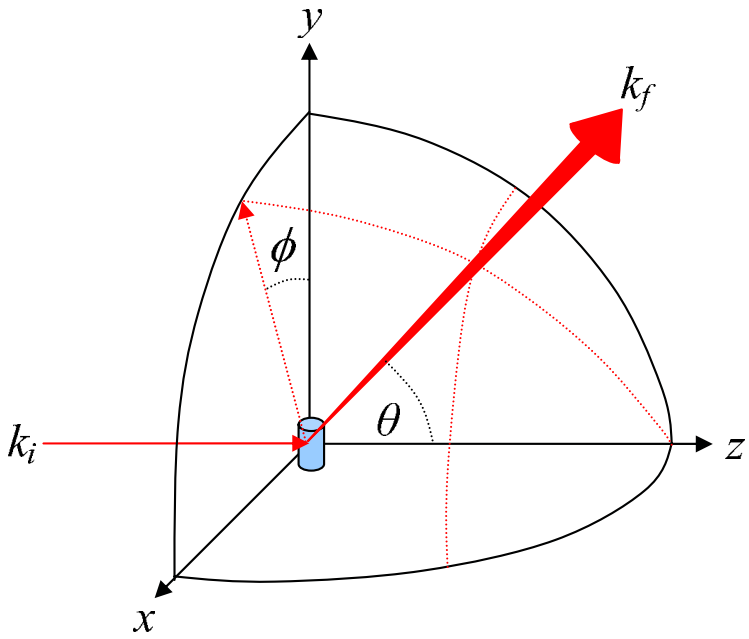

Figure 2.1: The geometry of a scattering experiment where the incident neutrons with wavevector $\mathbf{k}_i$ are scattered in the direction θ, ϕ with final wavevector $\mathbf{k}_f$.

When $E_i = E_f$, the scattering event is elastic and probes the structure or correlation of a system. When $E_i \neq E_f$, the scattering event is inelastic and probes the excitations in the sample.

The angular momentum, $\mathbf{L}$, of a neutron scattered from a single nucleus is quantised, $\mathbf{L} = \hbar\sqrt{l(l+1)}$ [55]. The angular momentum is equal to the neutron momentum multiplied by the distance between the neutron and the nucleus. That distance must therefore also be quantised, and at its closest is of the order of 10^{-14} m. This short-range interaction between the neutron and a nucleus compared to the wavelength of the neutron (approximately 10^{-10} m) means that only the partial $\mathbf{S}$ waves (with $l = 0$) will be scattered and that scattering will be spherically symmetric.

A plane wave of incident neutrons will have a wavefunction of the form:

$$\psi_{inc} = e^{i\mathbf{k}r}. \tag{2.4}$$

where r is the distance to the measurement position from the stationary nucleus. The

scattered wave will have a wavefunction of the form:

$$\psi_{sc} = -\frac{b}{r}e^{i\mathbf{k}r}, \tag{2.5}$$

where b is the scattering length; a constant specific to each element and the combined neutron/nucleus spin configuration. The resultant neutron will be described by

$$\psi = e^{i\mathbf{k}r} - \frac{b}{r}e^{i\mathbf{k}r}. \tag{2.6}$$

The total scattering cross-section of the nucleus involved (σ_{tot}) is defined by

$$\begin{aligned}
\sigma_{tot} &= \frac{\text{scattered neutron flux}}{\text{incident neutron flux}} \\
&= \frac{4\pi \mathrm{r}^2 \mathbf{v}| \left(b/r\right) e^{i\mathbf{k}r}|^2}{\mathbf{v}|e^{i\mathbf{k}r}|^2} \\
&= 4\pi\overline{b^2}
\end{aligned} \tag{2.7}$$

where $\mathbf{v}$ is the neutron velocity.

As the value b varies within the same atom type for different isotopes and even the direction of spin compared to that of the neutron, the scattering from a collection of such atoms is not perfectly coherent. An incoherent background is produced and the different scattering types must be defined. The total scattering is a sum of the incoherent scattering (σ_{inc}) and the coherent scattering (σ_{coh}) which are defined in Equations 2.8 and 2.9 [56].

$$\sigma_{inc} = 4\pi\overline{(b-\bar{b})^2} \tag{2.8}$$

$$\sigma_{coh} = 4\pi\bar{b}^2 \tag{2.9}$$

The incoherent signal can be used to study time dependent self-correlation functions; the probability of finding a particle at position r at time t when it was at $r = 0$ at $t = 0$. This describes the motion of a particle, an incredibly useful technique for the study of liquids and molecules.

To calculate the scattering from a unit cell and not just a single nucleus, the scattering from each atom must be considered. A scattered wave can be represented by an equation in the following form:

$$\psi_{sc} = b \exp^{2\pi i(hu+kv+lw)} \tag{2.10}$$

hkl are the Miller indices of the reflection and uvw are the fractional co-ordinates of the scattering source from the origin [57].

The summation of the scattering from each atom (n) in the unit cell is called the nuclear structure factor, F_N.

$$F_N = \sum_{1}^{n} b_n \exp^{2\pi i(hu_n+kv_n+lw_n)} \tag{2.11}$$

The structure factor is complex and contains the amplitude and phase information of the total scattered wave.

2.2.2 Magnetic scattering

The neutron has a magnetic dipole moment that will interact with magnetic fields. During the scattering process, the neutron will be affected by any magnetic field from the dipole moment of electrons; from their spin and from their orbital motion. The strength of this interaction is of the same order of magnitude as the coherent scattering from the nucleus. This is a significant point; in non-resonant X-ray techniques the scattering magnitude is approximately six orders of magnitude smaller.

An important consideration is that magnetic scattering does not originate from a relatively small component as the nuclear scattering does. The interaction happens over a much larger volume due to the spatial distribution of the magnetic interaction. The scattering is then highly θ dependent, a large decrease in intensity is observed with an increase in θ or $\mathbf{Q}$. This demonstrates that magnetic Bragg peaks need to be studied at low $\mathbf{Q}$ values. The dependency is defined in the magnetic form factor, f_M, where $\rho(r)$ is the density of magnetisation in the atom [54, 55].

$$f_M = \int \rho\left(r\right) \exp^{(i\mathbf{k}r)} \mathrm{d}r \tag{2.12}$$

The magnitude of magnetic scattering is defined by the magnetic scattering length, p [58].

$$p = \left(\frac{e^2\mu_n}{m_e c^2}\right)\mathbf{S}f_M \tag{2.13}$$

Where e and m_e are the charge and mass of an electron, c is the speed of light, $\mathbf{S}$ is the spin quantum number and μ_n is the magnetic moment of the neutron. This definition of the magnetic scattering length allows the magnetic structure factor ($\mathbf{F_M}$) to be defined, analogous to the nuclear structure factor.

$$\mathbf{F_M} = \sum_{1}^{n} p_n \mathbf{q}_n \exp^{2\pi i(hu_n + kv_n + lw_n)} \tag{2.14}$$

Where $\mathbf{q}_n$ is the magnetic scattering vector and is defined in Equation 2.15:

$$\mathbf{q} = \varepsilon\left(\varepsilon \cdot \mathbf{K}\right) - \mathbf{K} \tag{2.15}$$

ε is the unit vector in the direction of the scattering vector and $\mathbf{K}$ is the unit vector in the direction of the atomic magnetic moment. The interaction between the dipole moments is therefore dependent upon their orientations. Only the component of the magnetic moment perpendicular to the scattering vector gives rise to magnetic scattering [59].

The total scattered intensity from a reflection hkl from a non-polarised neutron beam is then the sum of the scattered intensities from the nuclear and magnetic contributions:

$$|F_{hkl}|^2 = |F_N|^2 + |\mathbf{F_M}|^2 \tag{2.16}$$

Ferromagnetic Bragg peaks occur at the same hkl positions at nuclear Bragg peaks. Antiferromagnetic peaks, and those from incommensurate magnetic structures appear at new hkl positions related to the magnetic ordering.

2.3 Neutron sources

There are two ways of producing the flux of neutrons required for experiments; nuclear reactors designed for research, or spallation sources. Both of these source types have been used in this study and are described here.

The Institut Laue Langevin (ILL) in Grenoble, France [60], is a high flux reactor that has been producing neutrons for experiments since 1971. It does this by using fissile enriched uranium 235 in a controlled reaction. The neutrons are slowed to useful energies using heavy water as the moderator and to cool the reactor system. The rate of the reaction is controlled by neutron absorbing control rods. The surroundings are shielded from radiation by a water pool housed in thick concrete.

The majority of neutrons used at the ILL are classed as thermal and are in equilibrium with the heavy water moderator at 300 K. Neutrons with other energies are also used and are produced using extra moderating material. A graphite source is kept at 2400 K to enable the use of hot neutrons. A liquid deuterium source is held at 25 K to produce cold neutrons. Neutrons are guided from these moderator sources using beam tubes or wave guides. An overall flux of 1.5×10^{15} neutrons cm^{-2} s^{-1} is achieved.

Heat dissipation is the limiting factor for reactor source types. Due to this, spallation has been confirmed as the production technique of choice for future neutron sources. The heat production per neutron is around $1/10$ of that produced in a reactor [61].

The ISIS spallation source is located in Oxfordshire, UK [62]. A spallation source very basically comprises a linear accelerator (a linac), a synchrotron and a target. The linear component accelerates pulses of H^- ions to an energy of 35 keV. The ions are bunched using a radio frequency quadrupole accelerator. The pulses are then passed into the linac. The ions are accelerated to 70 MeV in this part of the spallation source using radio frequency electric fields. The beam is passed through drift tubes to shield it when the field direction would cause deceleration.

The ion beam then enters the synchrotron and is passed through an aluminium oxide layer to remove the electrons and leave a beam of protons. The beam is accelerated to 700 MeV which causes it to be separated into two pulses. Dipole bending magnets keep the two beams on track. The proton beams circulate the 26 m radius synchrotron in the region of 10,000 times. The two beams are then passed to the extracted proton

beam line to make their way to the target. This happens with a frequency of 50 Hz, and a mean current of 200 μA.

The target is made of tantalum coated tungsten, a metallic material capable of donating many neutrons whilst still being suitable for engineering into the target component. The neutrons are then moderated to more useful energies by either ambient temperature water (316 K), liquid methane at 100 K, or liquid hydrogen at 20 K moderator sources. The average flux produced by any pulsed source is orders of magnitude lower than that achieved by a steady reactor source. However, the time-of-flight capabilities that a pulsed source offers remove the need for monochromatisation and the resulting reduction in flux.

2.4 Neutron detection

A good neutron detector will have a high detection efficiency, a low background, low sensitivity to non-neutron events, good stability and a short dead-time [63]. There are two main types of detectors: gas detectors and scintillator detectors [55]. Both techniques rely on using the neutrons to produce charged particles that then cause a change in the potential of the detector electrodes.

A gas detector comprises a sealed metal tube containing pressurised ^{3}He or BF_3 gas and a central thin wire anode. BF_3 is cheaper than ^{3}He but is toxic and less efficient. The efficiency of a gas detector can approach 100%. The ^{3}He detectors rely on the reaction described in Equation 2.17 to produce detectable charged particles:

$$^3_2\mathrm{He} + ^1_0\mathrm{n} \rightarrow ^3_1\mathrm{H} + ^1_1\mathrm{p} + 0.77\ \mathrm{Mev} \tag{2.17}$$

Scintillator detectors are much more suitable for diffraction instruments as the size and shape are variable. The scintillator material absorbs the neutron, and emits an alpha particle. These energetic charged particles ionize the surrounding atmosphere and cause it to fluoresce. This radiation enters photomultiplier tubes and electrons are ejected and detected.

Both kinds of detector can also incorporate position sensitivity. This is done by measuring the output of the anode at each end of the tube in a gas detector or measuring currents in the anodes situated beneath the photomultipliers in scintillator detectors [64]. Time or amplitude analysis of the output is used to derive the position of the event. Detectors have also been built that can determine the position in two dimensions by using a grid of perpendicular anodes.

2.5 Diffraction

The diffraction technique makes use of elastically scattered waves. As discussed in Section 2.1, neutrons can be obtained with de Broglie wavelengths similar to atomic spacings. When atoms are arranged into periodic, crystalline structures, the Bragg diffraction condition can be satisfied.

When a series of plane waves are incident upon a crystalline material at incident angle θ, only certain diffracted waves will interact coherently. For the waves to be in phase the path difference must equal an integer number, n, of wavelengths, λ. This is demonstrated in Figure 2.2, where the path difference is BC+CD, and Bragg's law is shown in Equation 2.18, where d is the separation of the crystal planes.

$$n\lambda = 2d\sin\theta \tag{2.18}$$

A diffraction pattern is produced when the angle of incident radiation (neutrons, X-rays or light) is scanned from one angle to another. Whenever an angle is reached that allows the Bragg condition to be satisfied, a Bragg peak is observed in the diffraction pattern. The intensity of a Bragg peak is a complex summation of the amplitude and phase of all diffracted waves at that point in θ. It is determined by calculating $|F_{hkl}|^2$, as shown previously in Equation 2.16.

The dipole interaction between the neutron spin and any magnetic field of the atom (such as core, unpaired electrons) can also lead to Bragg peaks to be diffracted in just the same way. Diffraction experiments can be performed on single crystal or

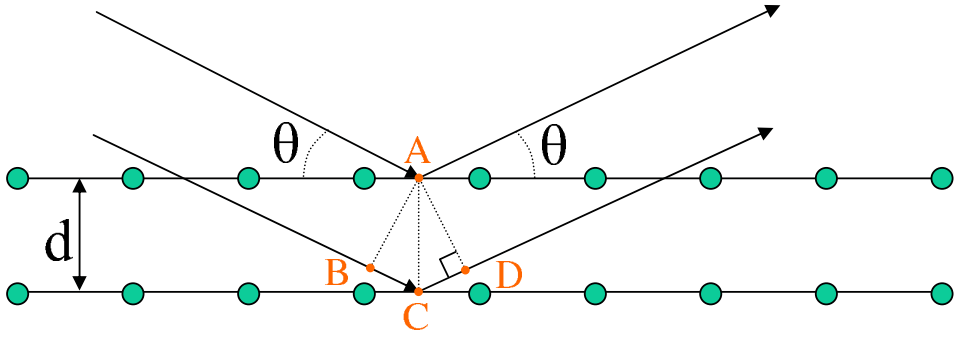

Figure 2.2: Scattering of two plane waves from two parallel lattice planes. The Bragg condition is satisfied when the path difference between two scattered plane waves equals an integer number of wavelengths.

polycrystaline powder forms of a material. When investigating a powder, a number of processes that are evident in single crystal diffraction are eliminated. Such processes as multiple scattering and extinction can cause errors in analysis.

2.5.1 GEM

During this study, the GEneral Materials diffractometer (GEM) instrument at the ISIS facility was used. GEM is a medium resolution instrument with a good flux of neutrons from the pulsed source. It has eight detector banks that cover an area of 7.270 m^2 in the angular range 1.2° to 171.4° [65]. The detector coverage is more than 30% of the scattering directions from the sample. The detectors are all ZnS/^{6}Li scintillators, the banks are shown in Figure 2.3.

GEM takes neutrons from the cold methane moderator source at a distance of 17 m. The instrument employs two disc choppers to set the wavelength range and prevent frame overlap from the pulsed source. It has a best resolution in reciprocal space of $\Delta\mathbf{Q}/\mathbf{Q} = 0.34\%$ at the backward scattering angle. This configuration is ideal for experiments to determine crystal structure. The available sample environments include a cryostat, a closed cycle refrigerator (CCR), a cryomagnet and a furnace to name a

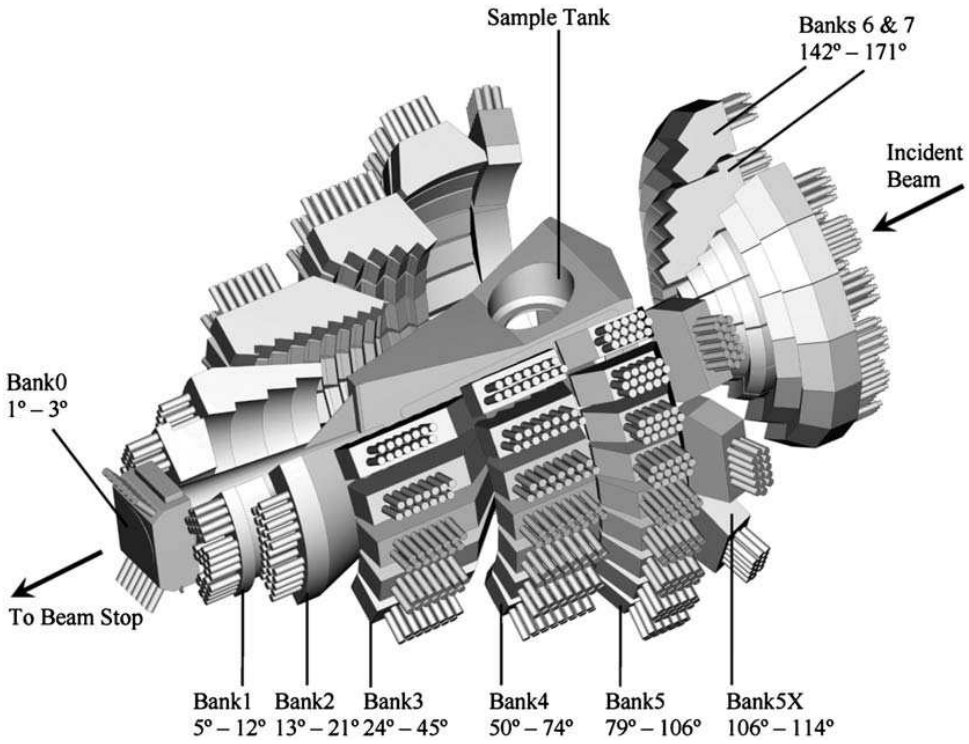

Figure 2.3: A diagram of the GEM diffractometer at ISIS. Image from reference [65].

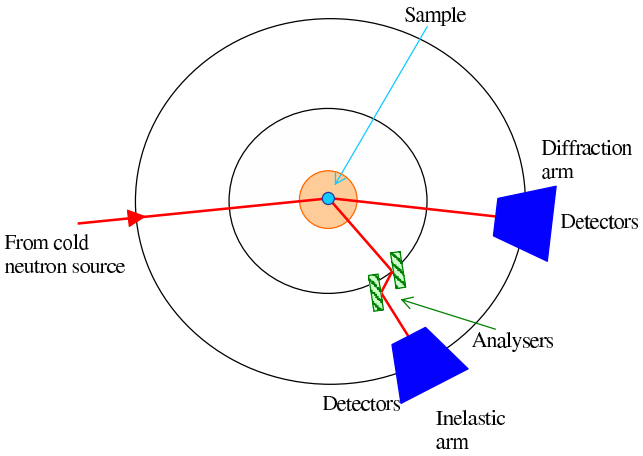

Figure 2.4: A diagram to represent the PRISMA spectrometer and diffractometer at the ISIS facility.

few.

2.5.2 PRISMA

The PRISMA instrument at the ISIS facility has two configurations allowing diffraction and spectrometry to be performed [66]. PRISMA takes neutrons from a methane moderator source at 100 K. The instrument can cover a large range in $\mathbf{Q}$ and has a large flux of long wavelength neutrons. The detectors used are ^{3}He tubes for both diffraction and spectrometry. The diffraction configuration is used to produce maps in reciprocal space. The sample environment options include the typical cryostat, CCR and cryomagnet. A schematic is shown in Figure 2.4.

2.5.3 D10

D10 is a four-circle and triple-axis diffractometer capable of energy analysis [60]. The four circle capability of the sample cradle maximises the availability of orientations for investigation. D10 takes thermal neutrons from the ILL reactor source. It has good reciprocal space resolution, good flux and low intrinsic background. It can be used in

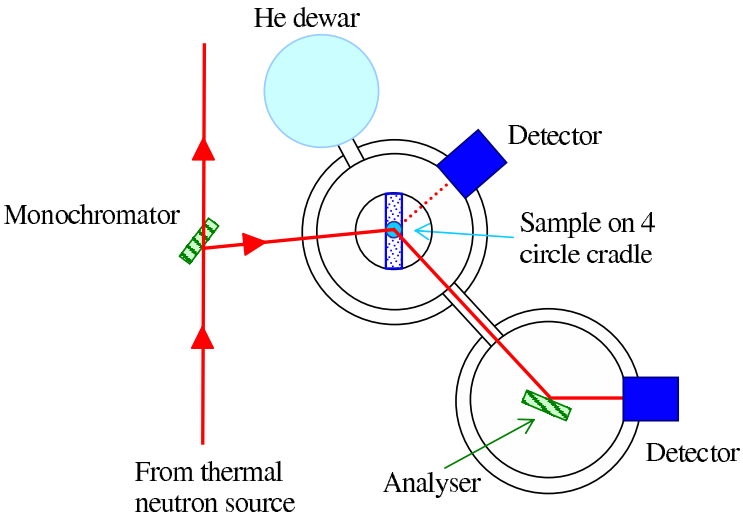

Figure 2.5: A schematic of the D10 spectrometer at the ILL. Image adapted from reference [60].

four different configurations: standard four-circle, standard two-axis, four-circle with energy analysis and two-axis with energy analysis.

The sample environment options include a four circle He flow cryostat for temperatures in the range 1.6 to 450 K. The cryostat is supported by a C-shaped Eulerian cradle. The instrument can also accommodate a cryomagnet, standard cryostat, furnace or pressure cell on the two axis tilt table.

Two detectors are available: an 80 mm$\times$80 mm microstrip detector for three-dimensional resolution in reciprocal space, or a single ^{3}He detector with better efficiency and lower background. The detector may be inclined up to 30° from the horizontal to increase coverage. A schematic is shown in Figure 2.5.

2.5.4 Refinement

To determine structural information from diffraction data, the data must be analysed by refinement. For powder samples, Rietveld refinement [67] is the least squares process of fitting all the Bragg peaks of a diffraction pattern by adjusting parameters in a proposed

structure. For single crystal data, the refinement process involves fitting the proposed structure to integrated intensities of Bragg peaks. In this study, refinement was carried out using the program FullProf [68], created by J. Rodriguez-Carvajal.

The function to be minimised for a powder profile as proposed by H. M. Rietveld [67] is shown in Equation 2.19. The sum is performed over all observations, i. W_i is a statistical weight and can be defined as $1/Y_i$ where Y_i is the measured number of counts. y_i is the measured contribution of the Bragg peak to the profile at position $2\theta_i$, and is defined in Equation 2.20. The parameters obs and $calc$ stand for observed and calculated respectively and c is a scale factor between the observed and calculated patterns. To produce a calculated value of y_i a sum must be taken over all contributing Bragg peaks.

$$M = \sum_i W_i \left\{ y_i\,(obs) - \frac{1}{c} y_i\,(calc) \right\}^2 \tag{2.19}$$

$$y_i = t\,|F_{hkl}|^2\, j_k L_k \frac{2\sqrt{\ln 2}}{H_k\sqrt{\pi}} \exp\left[-4\ln 2 \left\{ \frac{2\theta_i - 2\theta_k}{H_k} \right\}^2 \right] \tag{2.20}$$

t is the step size in the data, $|F_{hkl}|^2$ is the sum of the nuclear and magnetic contributions to the scattering. j_k is the multiplicity of the reflection and L_k is the Lorentz factor which defines the dependence of the integrated intensity of a peak on the diffraction angle. The effect is to reduce the intensity at intermediate diffraction angles, and to increase it at small and large values. $2\theta_k$ is the calculated Bragg peak position and H_k is the full width half maximum of the Bragg peak. The subscript k defines the reflection.

For single crystal data, where the information is recorded as integrated intensities, the function to be minimised is shown in Equation 2.21.

$$M = \sum_i W_i \left\{ |F_{hkl}|^2\,(obs) - \frac{1}{c} |F_{hkl}|^2\,(calc) \right\}^2 \tag{2.21}$$

Many refinement parameters are used to define the atomic and magnetic structure. The most significant to the analysis performed in this study are the lattice parameters, atomic positions, isotropic temperature parameters, half-width parameters, scale, and magnetic moment vector contributions. The symmetry of the unit cell must also

be described to complete the unit cell. The quality of the fit to the data is described by an R-factor, defined in Equation 2.22 for the total of the magnetic and nuclear contributions.

$$\mathrm{R}_{\mathrm{total}} = 100 \times \frac{\sum_i \left| |F_{hkl}|^2 (obs) - \frac{1}{c} |F_{hkl}|^2 (calc) \right|}{\sum_i |F_{hkl}|^2 (obs)} \tag{2.22}$$

Representation analysis is used to determine the symmetry of a magnetic unit cell. This technique calculates the allowed and disallowed symmetry operators for a unit cell when taking into account the known properties such as the propagation vector. Throughout this study the programme BasIreps from the FullProf Suite was used to calculate the symmetry operators which left the physical properties of the system invariant and were therefore allowed. All possible combinations of symmetry operators were tested during the Rietveld refinement.

2.6 Spectrometry

Neutron spectrometry is the measurement of the inelastic interaction between matter and neutrons. The energy range of neutrons matches well with the electronic excitation energies in condensed matter. This makes the change in energy of a neutron during an inelastic interaction with an excitation a significant, detectable value.

Spectrometers make use of a monochromator or chopper to select the wavelength or energy range of the neutrons. Energy analysis is then performed on the scattered neutrons. This is done either by calculating the neutron's time of flight or by directing the scattered beam through an analyser to determine the Bragg reflection angle and converting the wavelength to an energy.

2.6.1 PRISMA

As well as the diffractometry option, the spectrometry capabilities of PRISMA were also utilised in this study [66]. When using the inelastic measurement configuration, data

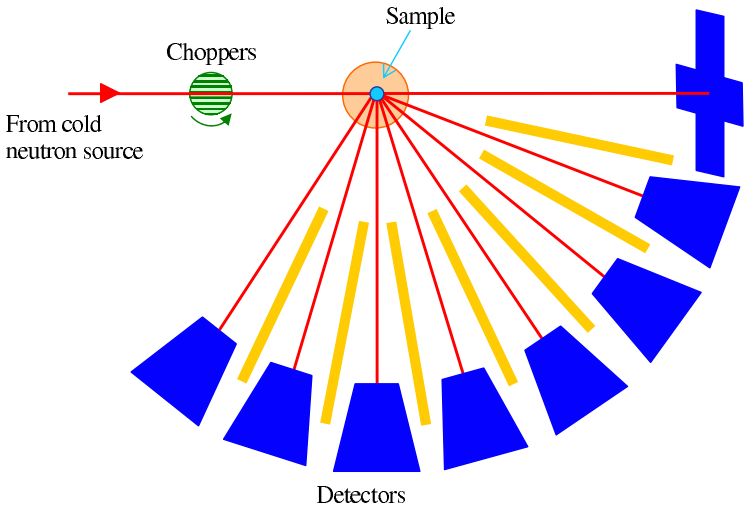

Figure 2.6: A schematic to represent the Mari chopper spectrometer at the ISIS facility.

can be collected in two modes. A single $\mathbf{Q}$-ω line in reciprocal space parallel to $\mathbf{k}_i$ can be measured, or individual analysers can be set up to measure several different $\mathbf{Q}$-ω lines parallel to $\mathbf{k}_i$. A basic diagram of the main components of the instrument is shown in Figure 2.4. A compact two analyser configuration is used on the inelastic detector arm.

2.6.2 Mari

The Mari instrument at the ISIS facility is a direct geometry chopper spectrometer. It has continuous ^{3}He detector coverage from 3 to 134° and an incident energy range of 9 to 1000 meV. This makes it capable of mapping a large area in $\mathbf{Q}$ and energy in one measurement. The range of energy and the resolution used is selected by using one of five chopper packages. Mari takes neutrons from a methane moderator source at 100 K. The majority of Mari's detectors are positioned beneath the sample position with a cross shaped array covering the higher positions, a schematic is shown in Figure 2.6.

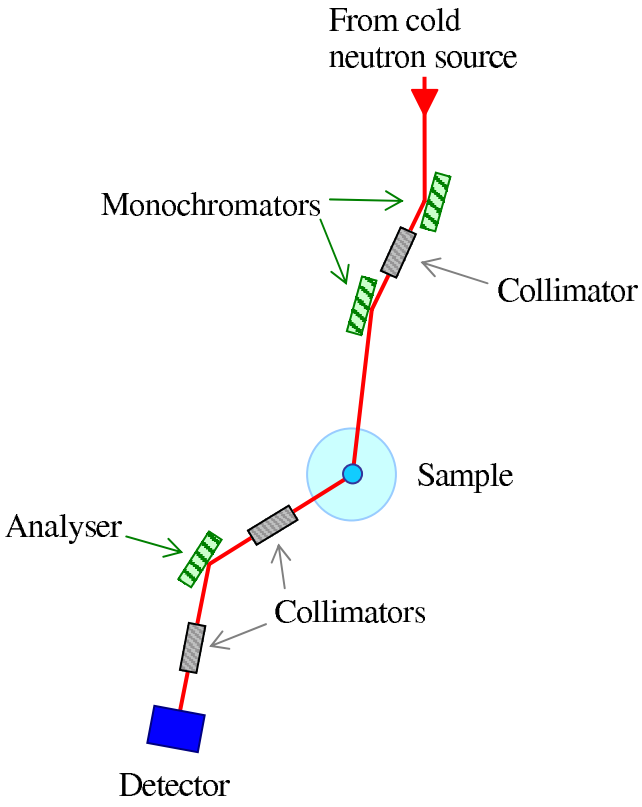

Figure 2.7: A diagram to represent the 4F1 and 4F2 triple-axis spectrometers at the LLB. The geometry shown is that of instrument 4F1. Image adapted from reference [69].

2.6.3 4F1/2

The 4F1 and 4F2 instruments are two cold neutron triple-axis spectrometers at the reactor source Laboratoire Leon Brillouin in Saclay, France [69]. The two instruments only differ in their geometry, one is a mirror image of the other. The basic components are shown in Figure 2.7 for the geometry of 4F1.

The spectrometers use ^{3}He detectors and can cover an angular range of -5 to 140°. The wavelength range is 1.8 to 6 Å, the shortest wavelengths achieved by the use of a Be filter at 77 K. The monochromators are pyrolytic graphite and the neutrons arrive from a liquid hydrogen cold source moderator.

Chapter 3

Sample preparation and experimental techniques

3.1 Crystal growth

3.1.1 Powder preparation

The starting materials for all samples studied were high purity oxide powders. The powders used were NiO or CoO with V_2O_5 [22]. Stoichiometric ratios of the powders were ground by hand using a mortar and pestle until the particle size could be reduced no further and the finest grain powder was achieved. The powders were then heated in air, the duration and temperatures used are detailed in Table 3.1. The samples were ground thoroughly in-between each heating.

Material	First run		Second run	
	Duration (hours)	Temperature (°C)	Duration (hours)	Temperature (°C)
$Ni_3V_2O_8$	24	800	24	900
$Co_3V_2O_8$	24	800	48	1050

Table 3.1: Duration and temperatures for the heating of each sample. The materials were ground in between these heatings.

The powders were checked for purity and phase formation using X-ray diffraction (see Section 3.2.1). If the phase was not ideal to the extent that: no Bragg peaks were absent, no extra peaks were observed, and the relative intensities were of the correct order, then the last heating phase was repeated until the desired phase was reached.

3.1.2 Floating zone technique

The floating zone crystal growth technique uses the principle of epitaxial growth to produce large, high quality crystals. The starting materials required are a compressed powder rod and ideally, a piece of crystal of the same material to act as a seed. When making the first crystal of a material, the crystal piece may be substituted by a short piece of compressed powder rod, although this may reduce the quality of the crystal grown.

The powder rod is suspended above the crystal piece and the two axes are counter rotated, as demonstrated in Figure 3.1. Elliptical mirrors concentrate the heat from high power infrared lamps into a central spot. The ends of the rod and seed piece are brought towards this hot central part of the furnace. The ends melt and are touched together to form the floating zone, which is thoroughly mixed by the rotation of the rod and seed. The floating zone region is then moved up the compressed powder rod, either by moving the mirror stage, or the powder and seed rods. Material in the lower part of the zone solidifies as it moves from the central hot area and cools, taking on the atomic structure of the seed piece.

Two furnaces were used in the preparation of the $Co_3V_2O_8$ and $Ni_3V_2O_8$ crystals. The first furnace used was an NEC two mirror infrared image furnace, model number SC-N35HD. The powder rods were first scanned through this furnace at speeds of 15 to 20 mm/hour to produce a constant density, and therefore more stable rod for a slower growth. This fast scanned rod was then run through a four mirror furnace at a much slower speed of 0.5 mm/hour. The furnace used was a Crystal Systems Inc. Optical Floating Zone Furnace, model number FZ-T-10000-H-IV-VPS. The four mirror

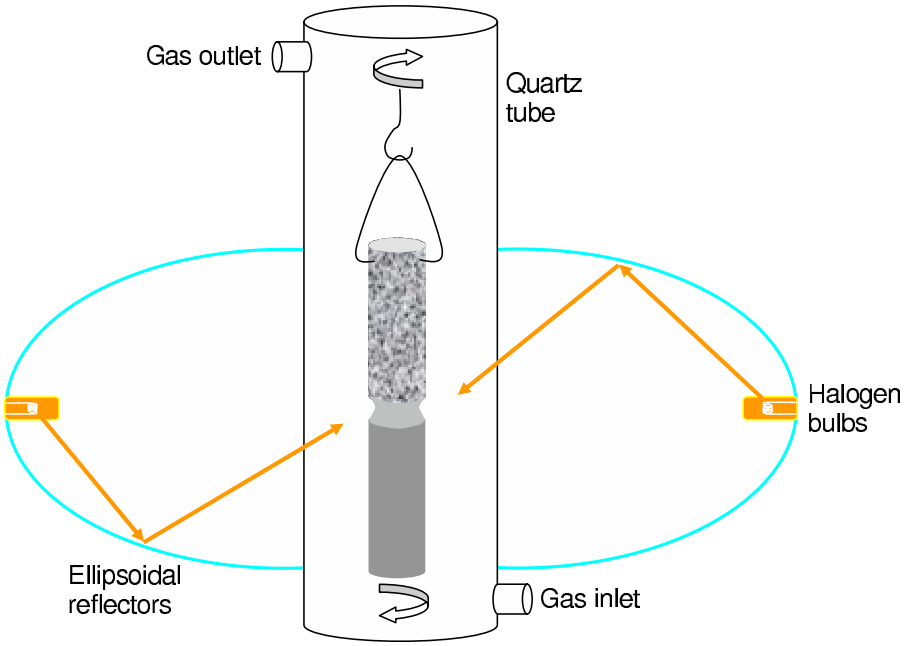

Figure 3.1: A diagram to represent the floating zone technique, not drawn to scale. The polycrystalline powder rod is suspended and counter rotated over the seed crystal. The ellipsoidal reflectors concentrate the heat from the halogen lamps onto the central molten "floating zone". The sample is contained within a quartz tube to enable environment options.

configuration gives a more even central hot spot.

Unlike some materials, these samples lose little mass during zoning so this slow speed does not pose a problem with decomposition. These processes were all performed in air at ambient pressure.

3.2 Compositional analysis and crystal alignment

3.2.1 X-ray diffraction

To check the phase formation and impurity level of the materials, powder samples were investigated using X-ray diffraction. This process was performed at various stages throughout the sample preparation. Firstly, to check the powder to be used for crystal growth, or powder experiments. Secondly, a small section of the crystal was ground and investigated to check that no impurities had been introduced during the growth, or that the phase had changed.

There were two X-ray kits used to investigate the powder purity. They were a Bruker X-ray Diffractometer D5005, and a Hilton Brooks XRD unit. All kits use a Cu K_α source with wavelength λ=1.5418 Å and detect in the reflection mode. The signal is produced when the Bragg condition is satisfied: coherent scattering from the crystallite planes causes Bragg peaks to appear, as described in Section 2.5. The series of peaks detected were compared in position and intensity to published results. A typical scan would be from 10 to 90° in 0.05° steps, with 3 seconds counting time per point. These settings gave a background level of the order of 50 counts and an approximate strongest peak value of 1000 counts.

3.2.2 X-ray Laue technique

Each crystal produced needed to be aligned to ensure the maximum amount of information was gained from it. This was done using an X-ray Laue camera, and occasionally, a neutron Laue camera.

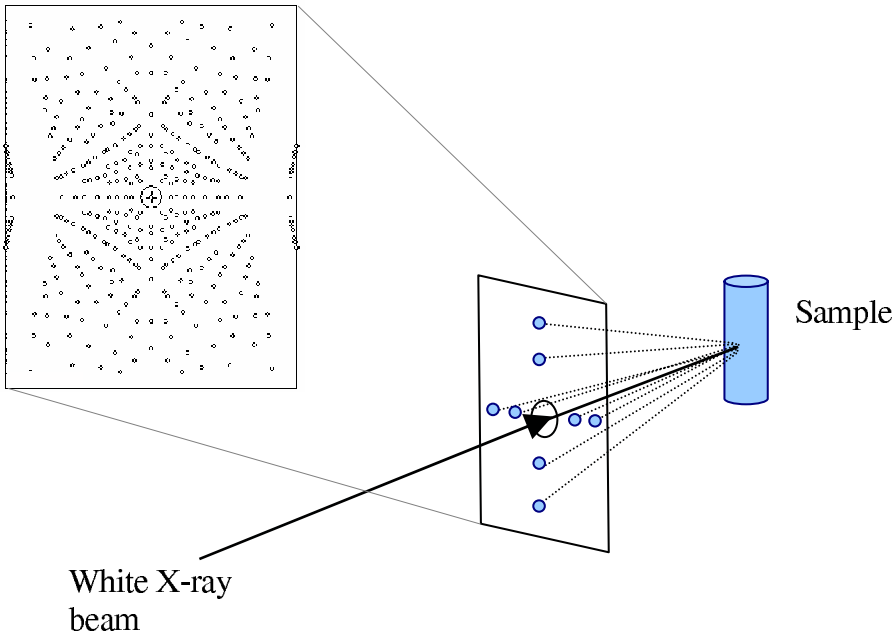

Figure 3.2: A diagram to represent the back reflection Laue technique. The example of an observed pattern was produced using Orient Express [70] centred on the [1 0 0] direction in $Ni_3V_2O_8$.

The Laue instruments that were used detect the back scattered signal from the sample [57]. The white X-ray beam passes through a central hole in the CCD plates, and is diffracted from the sample back to the CCD as shown in Figure 3.2. The sample is mounted on a computer controlled triple-axis goniometer and is stationary during data acquisition. A wide range of wavelengths is present in the incident beam so the Bragg condition for each lattice plane is satisfied by a different wavelength.

The program Orient Express [70] was used to identify the crystal orientations. This program calculates the expected diffraction pattern from the crystal using the space group and atomic positions. The calculated pattern can then be compared to the pattern produced with the Laue camera, and the orientation determined. Crystal pieces with faces perpendicular to the main crystallographic directions were cut using a low speed diamond wheel saw.

3.2.3 Scanning electron microscopy

Scanning electron microscopy [71] was used to check the composition of the crystal samples. In a vacuum, electrons are accelerated and focused onto a spot of 1 to 5 nm in diameter. The electron beam position is controlled by deflection coils, which scan the beam position in a raster pattern. The electrons interact with a tear drop shaped volume of the sample called the interaction volume (see Chapter 5 [72]). Secondary electrons are emitted from the uppermost layer of this volume, near the surface. Below this layer, backscattered electrons are produced, then deeper still, X-rays are emitted.

There are multiple detection modes used in SEM. Initially, the secondary electrons are used to investigate the topography of the material. When the composition is of more importance than the topography, the secondary electron mode is only used to refine the focusing of the beam. The X-ray emission spectra are then detected to determine the composition of the material using energy dispersive X-ray analysis (EDX).

A third mode can be employed to determine the structure of a crystalline material. The electron backscatter diffraction mode detects Bragg diffraction using a defocused, near parallel beam set-up. If the beam is swept over a sufficiently wide angle, the Bragg condition will be satisfied for multiple lattice planes. The image produced will show many overlapping lines. The crossing point of the lines represents lattice planes, and so the structure can be solved.

The surface of the sample must be polished to a very high standard using progressively finer grain abrasives. The final polishing material is colloidal silica, with a particle size of $1/4$ μm. If the sample is insulating, a few atomic layers of a conducting material such as gold, must be deposited for the technique to work.

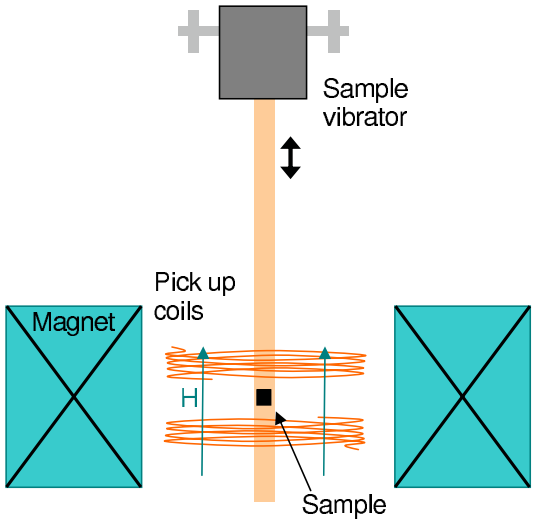

Figure 3.3: A diagram of the main components in the Vibrating Sample Magnetometer (VSM). The sample is vibrated at a frequency of 55 Hz over a distance of 1.5 mm in an applied magnetic field.

3.3 Laboratory measurements

3.3.1 Vibrating sample magnetometry

An Oxford Instruments Vibrating Sample Magnetometer (VSM) was used to probe the magnetic properties of the samples. This technique is inductive; moving a magnetised sample through a pair of pick-up coils causes a change of magnetic flux in the coils and the induced e.m.f. is proportional to the magnetic moment. The VSM vibrates the sample at a frequency of 55 Hz over a range of 1.5 mm. This movement induces a current in the two pick up coils situated above and below the sample. The VSM has a sensitivity of approximately 10^{-5} emu of magnet moment and has a magnetic field range of $\pm$120 kOe. A schematic diagram of the main components is shown in Figure 3.3.

Due to the relatively small separation of the coils, the sample size is an important factor. If the sample is too large along the direction of separation of the coils, the magnetisation is systematically reduced.

The VSM has a temperature range of 1.4 to 310 K with its usual configuration, or from 100 to 1000 K when using a furnace insert. The low temperatures are achieved by using liquid nitrogen and liquid helium. The sample space is further surrounded by a vacuum layer to insulate it. Temperatures below the boiling point of liquid helium (4.2 K) are reached by pumping helium through the sample chamber at a reduced pressure.

3.3.2 SQUID magnetometry

A Quantum Design Super conducting QUantum Interference Device (SQUID) magnetometer (model MPMS-5S) was also used to investigate the magnetisation of the single crystal samples. SQUID magnetometry is another inductive technique, moving the sample slowly through the pick up coil set [73]. The pick up coils are wound as a second order gradiometer and are connected to the SQUID via superconducting wires. The top coil is one turn wound clockwise, the centre coil comprises two turns wound anticlockwise and the lower coil is one turn wound clockwise. The coils are positioned at the centre of the superconducting magnet outside the sample chamber.

The gradiometer configuration (see Figure 3.4) reduces noise in the detection circuit caused by fluctuations in the large magnetic field of the superconducting magnet. The SQUID device converts the induced current to a usable voltage proportional to the magnetic moment of the sample. The SQUID is situated below the system magnet protected by superconducting shielding.

This magnetometer is sensitive to approximately 10^{-9} emu of magnetic moment and has a magnetic field range of $\pm$50 kOe. The residual field is much lower than in the VSM, making the accuracy of the SQUID measurements much higher. The 4 cm over which the sample moves in a measurement must be considered. The magnetic field must be homogeneous over this range so as not to cause problems with hysteretic samples. The SQUID maintains an accurately homogeneous field to allow high sensitivity measurements to be made.

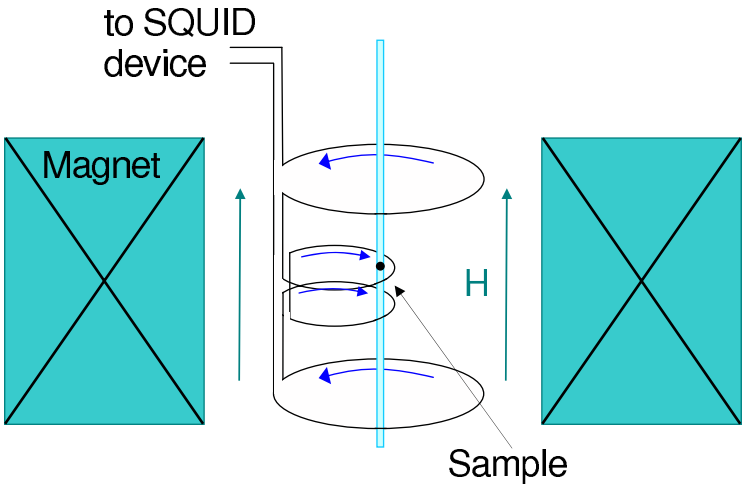

Figure 3.4: A diagram of the main components of a SQUID magnetometer. The sample is moved through the pick-up coils in an applied field. The SQUID device is shielded from magnetic fields and converts the induced current to a meaningful voltage with high sensitivity.

3.3.3 Specific heat measurements

The Quantum Design Physical Properties Measurement System (PPMS) is designed to accept various inserts for specific heat, resistivity and magnetisation measurements. In this study the specific heat insert and a closed cycle He^3 specific heat insert were used.

An insulating sample has two main contributions to the specific heat (C); from the lattice and from the magnetic properties of the sample [74]. The lattice contribution decays with temperature as T^3 at low temperatures and so this technique is very powerful for investigating low temperature magnetic transitions. Heat capacity measurements can also determine the spin state of a system. This is done by calculating the magnetic entropy of the material, S_m, as a function of temperature (T) using Equation 3.1.

$$S_m = \int_0^{T_{\max}} {}^{C}\!/_{T} dT \tag{3.1}$$

The total entropy recovered will then reveal the spin state of the system by

$$S_m(T \to \infty) = R\ln(2S+1), \tag{3.2}$$

where R=8.314 J/mol K.

To perform such a measurement, the sample is secured to a platform using a highly thermal conducting grease. Measurements must be run before this to produce addenda files to subtract from the data collected with the sample. Even a small difference in the amount of grease used in the addenda and sample measurements can produce a significant discrepancy in the data collected.

The platform is suspended inside a puck from eight wires in the standard ^{4}He configuration, and four wires in the ^{3}He configuration. Half of the wires are the contacts to the platform heater, the remaining wires are the contacts to the platform thermometer. Half of these wires are current carrying, whilst the others measure voltage. Another thermometer external to the puck is used as the reference temperature of the system.

For each set point in a temperature scan, the sample space is set to a reference temperature. When stability is maintained, an amount of heat equal to a small percentage of the reference temperature is applied to the sample plate. The rise and decay of temperature of the sample platform is recorded and fitted using a two τ method. Two relaxation time constants (τ) are needed to represent the decay of temperature from the sample, and from the platform, sample and heater system. If the sample is sufficiently conducting, a one τ method can be used. The PPMS software automatically determines whether to use the one or two τ method for each data point collected. The temperature range of the PPMS is 1.5 to 400 K, and with the ^{3}He insert, this is extended to 340 mK.

As the samples studied here are insulating, for this technique they must be thin, in the region of 0.2 mm. If the samples were too thick, the rate of heat transfer measured would be inaccurate. A proportion of the heat would be transferred to the rest of the sample, rather than back to the supporting platform.

Chapter 4

Magnetic properties of $Co_3V_2O_8$

4.1 Single crystals

The powder samples of $Co_3V_2O_8$ were manufactured using the procedure described in Section 3.1.1. The purity of the powder was found to be excellent; no extra or missing Bragg peaks were observed in laboratory X-ray diffraction patterns. An example pattern and the comparison to the current best data available [75] are shown in Figure 4.1.

Single crystals were then prepared using the technique described previously (Section 3.1.2). Multiple growth speeds were tested and the speed at which the growth was most stable and with the best crystals produced was found to be 0.5mm/hour. The rods used for these growths had initially been scanned through the floating zone furnace at a much higher speed of 15mm/hour to remove any air bubbles. Many crystals were produced; the best crystal was manufactured when a sequence of four crystal rods were grown, each using the previous crystal as a seed. This approach produced a final crystal of very high quality. It was found to have a mosaic spread of less than 0.5° over its entire 2 cm^3 volume. The polished crystal was checked with the EDX technique and no impurities were detected within an accuracy of approximately 1 atomic %. Within this accuracy, the relative ratios of the heavier atoms, Co and V were correct at 3:2. A picture of this crystal is shown in Figure 4.2. The crystals were aligned using an X-ray

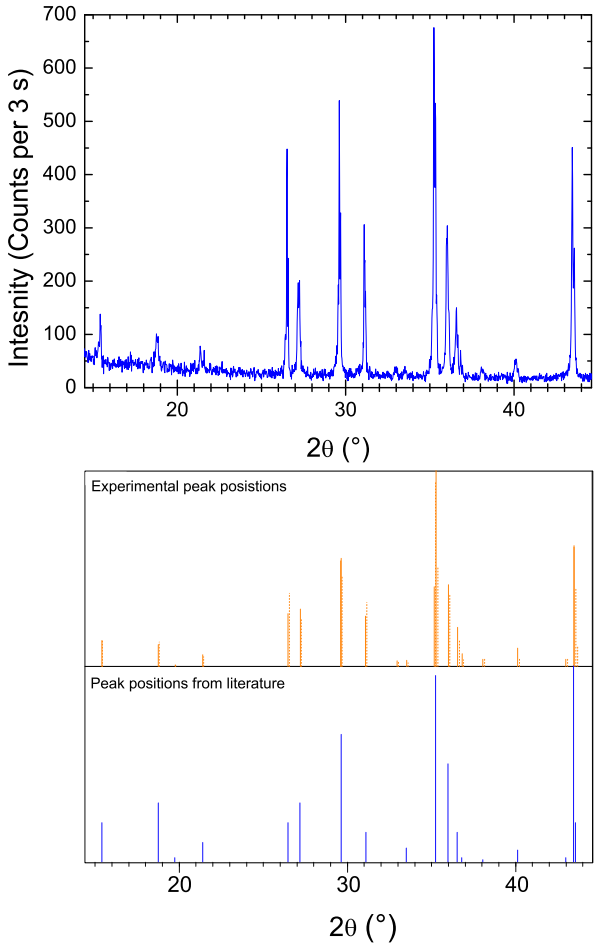

Figure 4.1: X-ray diffraction pattern of $Co_3V_2O_8$ (upper panel) and the fitted peak positions compared to published peak positions from reference [75] (lower panel). A Cu Kα source was used to produce an X-ray wavelength of 1.5418 Å. The dotted lines mark the Kα_2 experimental peak positions.

Figure 4.2: A $Co_3V_2O_8$ single crystal grown using the floating zone technique.

Laue camera. An example of the images produced is shown in Figure 4.3. It shows the symmetry observed when the crystal is aligned along the [1 0 0] direction. Once aligned along the three crystallographic axes; the crystal was cut using a low speed diamond wheel saw and laboratory measurements were taken.

4.2 Magnetic phase diagram

Through magnetometry (VSM and SQUID) and specific heat measurements, the magnetic field vs. temperature phase diagram for $Co_3V_2O_8$ was produced, and is shown in Figure 4.4. The precise positions of the phase transitions were chosen using consistent means throughout. For example, if the transition was observed as a hysteresis in a magnetisation measurement taken as a function of applied field, then the transition point was taken as the average of the two peaks in the derivative. If the transition was observed as a peak in the susceptibility, the transition point was chosen as the temperature at which the derivative crossed zero. If the transition was observed as a change in the gradient of the susceptibility then linear fits were made to the data on either side of this change and the transition point was taken to be the point where these two lines cross.

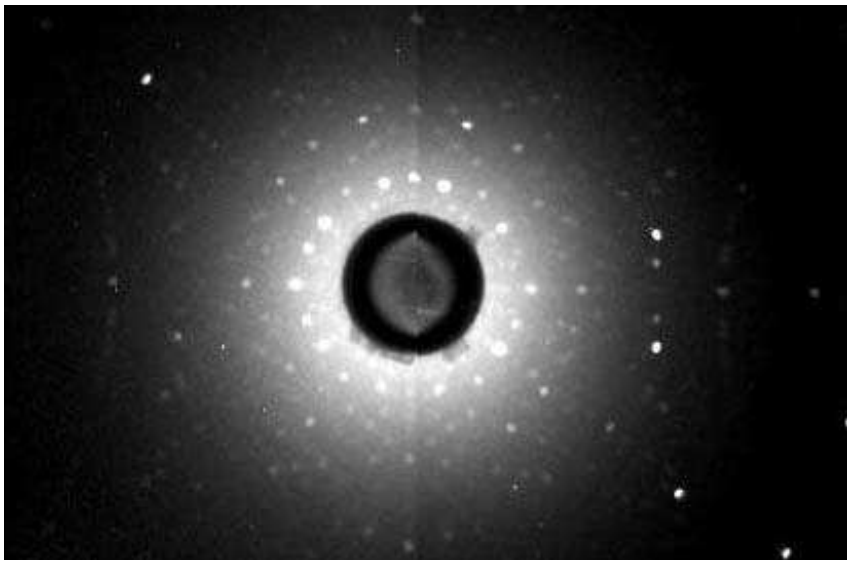

Figure 4.3: An X-ray Laue image from a $Co_3V_2O_8$ single crystal centred on the [1 0 0] direction. The space group of the structure is orthorhombic Cmca.

The samples were investigated with fields applied along each of the three main crystallographic directions, aligned with an accuracy of at least 3°. The phase transitions were tracked in the temperature interval between 1.4 and 12 K in a magnetic field range of $\pm$120 kOe. When extrapolated to zero applied field, the transition temperatures were found at 11, 8.7, 6.7 and 6 K.

A range of characteristic magnetisation and susceptibility curves for $Co_3V_2O_8$ is shown in Figure 4.5. The $\mathbf{M}(\mathbf{H})$ curve for a field applied along the easy a-axis at 2 K shows a very rapid increase caused by a small field – the magnetic moment is practically saturated at 2 kOe. From the value of magnetisation at $\mathbf{H} = 80$ kOe (shown in the left panel of Figure 4.5), the lower limit for the average Co moment was found to be 3.6 μ_B. From the inset of this figure, it is evident that there is no significant remanent magnetisation in zero field (less than 4% of the saturation magnetisation) and no significant hysteresis, within the measurement field resolution of 50 Oe.

In the antiferromagnetic phase at 8 K, it is again very easy to saturate the

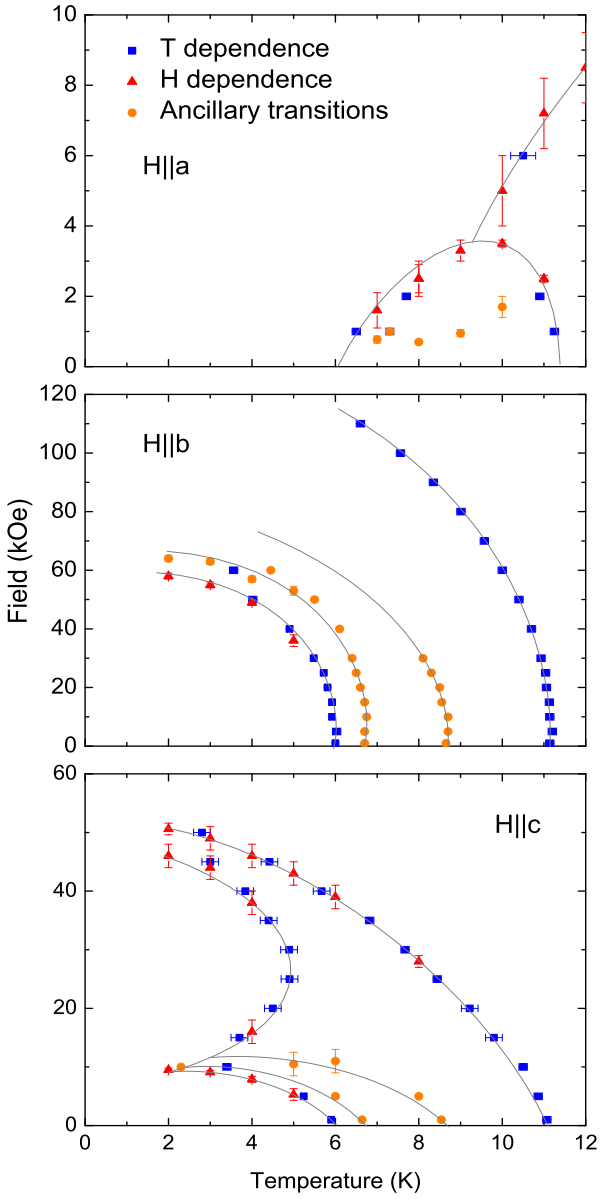

Figure 4.4: Magnetic phase diagram of $Co_3V_2O_8$ for magnetic fields applied along the three main crystallographic directions. Magnetisation temperature and field curves were used to follow the transitions. The orange symbols represent anomalies in the magnetisation curves that correspond to the locking and unlocking of the propagation vector within the incommensurate antiferromagnetic phase. Note the different scales of field for each direction. Curves are drawn as guides to the eye only.

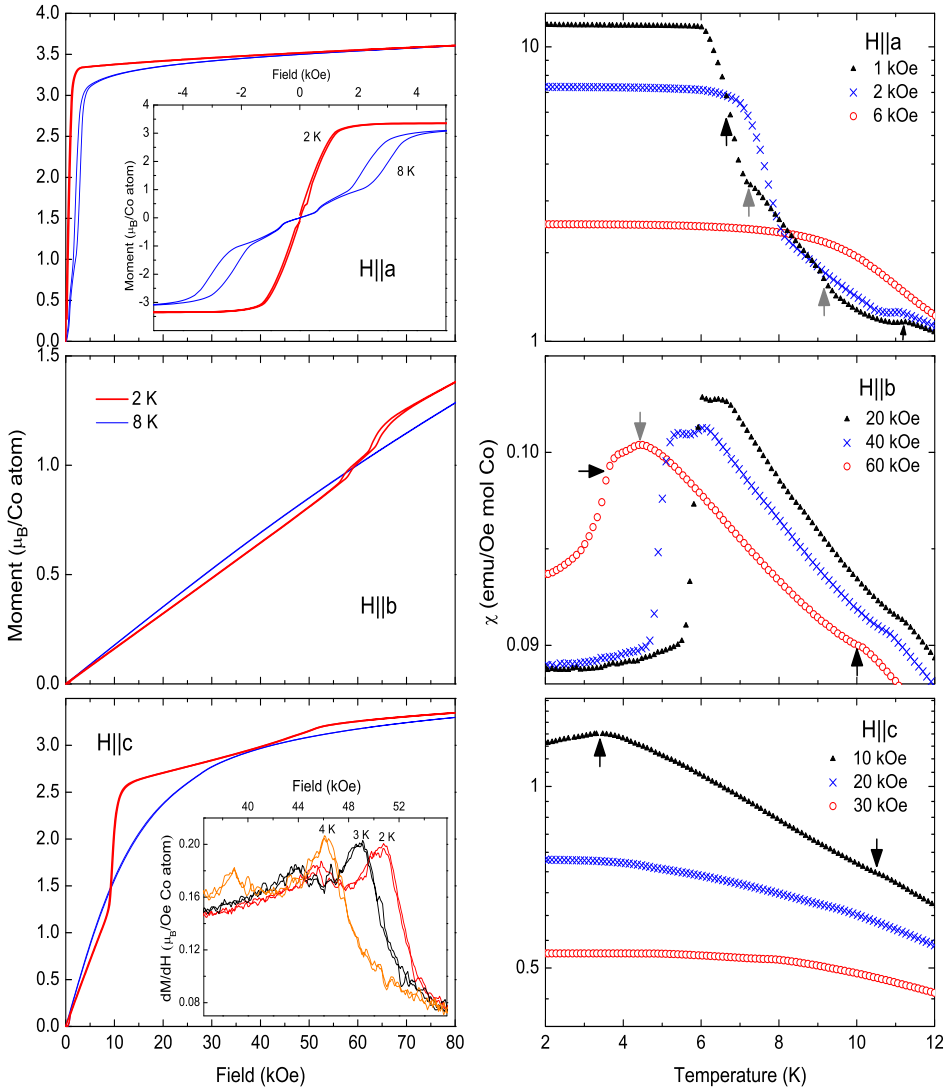

Figure 4.5: Left: Magnetisation curves for the three main crystallographic directions of $Co_3V_2O_8$. The 2 K data are in the ferromagnetic phase, and the 8 K data in the antiferromagnetic phase. For $\mathbf{H} \parallel a$, the inset shows no hysteresis in the ferromagnetic phase (within a 50 Oe field resolution) but a considerable hysteresis exists around 2.7 kOe in the antiferromagnetic phase. For $\mathbf{H} \parallel b$, two step like features are seen at 2 K but not at 8 K. For $\mathbf{H} \parallel c$, $d\mathbf{M}/d\mathbf{H}$ indicates more definitely the location of phase transitions, shown by the inset. Right: Susceptibility curves in various fields. The black arrows indicate the locations of phase transitions. The grey arrows (such as at 60 KOe and 4.5 K for $\mathbf{H} \parallel b$) point to the unlocking and unlocking of the commensurate antiferromagnetic structure. These phase transitions were used to build the $Co_3V_2O_8$ phase diagram (Figure 4.4).

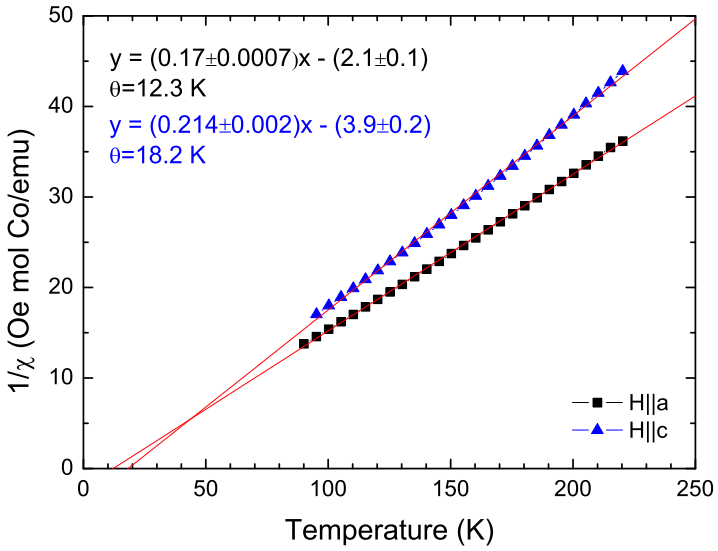

Figure 4.6: The Weiss temperature θ was determined for $Co_3V_2O_8$ using SQUID magnetometry measurements. A linear fit is applied at temperatures above the magnetic transitions and the x-intercept is found. For fields applied parallel to the a and c-axes the average value was found to be $+15\pm3$ K.

magnetisation. In the small field range before saturation, the system clearly passes through a region of hysteresis centred around 2.7 kOe indicating the presence of an additional phase transition. The phase transitions are also clearly seen as anomalies in the susceptibility ($\chi(T)$) curves at low fields. However, by 6 kOe the susceptibility curve is very smooth, making it impossible to pin-point the transition temperature.

From the magnetisation curves shown for $\mathbf{H} \parallel b$ (central panels, Figure 4.5), it is obvious that this direction is the hard axis of the system. In a field of 80 kOe parallel to b, the average magnetic moment is less than 40% of that found for a low field applied along the a-axis. The $\chi(T)$ curves measured for these two directions differ by a factor of almost 100 [35]. In the low temperature phase at 2 K, the $\mathbf{M}(\mathbf{H})$ curve shows two step-like hysteretic anomalies at 58 and 64 kOe. These features, and others, are easily followed across $\chi(T)$ curves measured in different applied fields.

The two features that are step-like at low temperatures, are shown by black arrows on the $\chi(T)$ curve measured at 60 kOe. The black arrows indicate the locations of the paramagnetic to antiferromagnetic and antiferromagnetic to ferromagnetic phase transitions. The grey arrow corresponds to an anomaly in the curve that cannot be attributed to a clear phase transition. This will later be shown to be associated with the unlocking of the propagation vector from $(0, 1/2, 0)$ within the intermediate magnetic phase.

For $\mathbf{H} \parallel c$, in the low temperature phase at 2 K, the saturation magnetic moment approaches that for $\mathbf{H} \parallel a$. The $\mathbf{M}(\mathbf{H})$ curve for $\mathbf{H} \parallel c$ shows multiple features at 9.5, 46 and 51 kOe. To best observe all of these, the derivative of the magnetisation must be considered. These irregularities can also be followed in the $\chi(T)$ curves. The ordering temperature decreases significantly with applied magnetic field, for $\mathbf{H} \parallel c$ for example, T_N(40 kOe) $\approx 1/2\ T_N$(1 kOe). Such a dramatic decrease in the ordering temperature is unusual even for highly frustrated systems. The average Weiss temperature for this system was found to be $+15 \pm 3$ K, as shown in Figure 4.6. This number compares well with the value of $+14$ K found by Rogado *et al.* [26] for a polycrystalline sample.

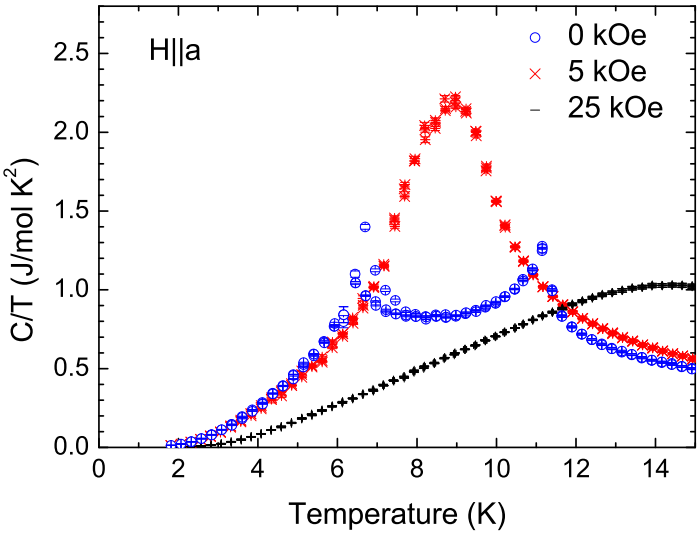

Figure 4.7: The specific heat of $Co_3V_2O_8$ normalised by temperature. Measurements were taken at applied fields of 0, 5 and 25 kOe parallel to the easy a-axis.

Demagnetisation factor corrections have been tested and found to make minimal impact on the estimated position of phase transitions. By far the greatest inaccuracy comes from allocating a transition field or temperature, especially when derivatives are required to do this.

The specific heat of the sample was also investigated for fields applied parallel to the easy a-axis. Figure 4.7 shows the specific heat normalised to temperature for applied fields of 0, 5 and 25 kOe. The sharpness of the observed peaks quickly fades with the application of higher fields. As this crystallographic direction is so sensitive to applied fields, the transition temperatures gained through these measurements have not been added to the already slightly cluttered phase diagram.

Shown in Figure 4.8 is the specific heat of $Co_3V_2O_8$ extended to high temperatures. As the low temperature specific heat is dominated by the magnetic contribution, the high temperature data must be used to approximate the lattice contribution. The data between 50 and 300 K have been fitted with a combination of Debye and Einstein

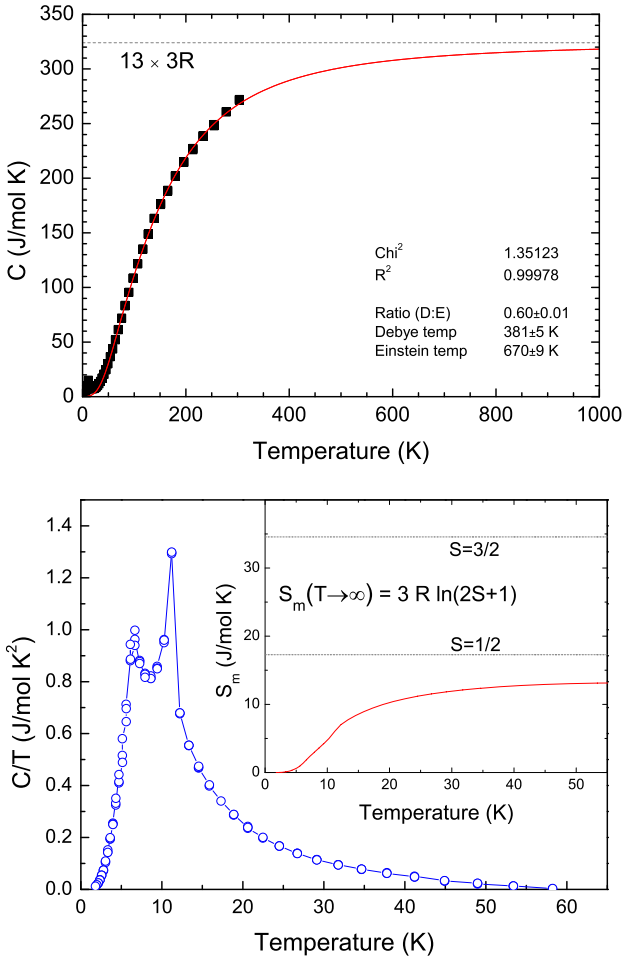

Figure 4.8: Top: The specific heat of $Co_3V_2O_8$ extended to high temperatures. The data between 50 and 300 K have been fitted with a combination of Debye and Einstein temperatures. Bottom: The low temperature data has had the fit from the top figure subtracted, and an integration has been performed over T to extract the recovered entropy of the system. These data were all collected in zero applied field.

models [76]. The Debye temperature that corresponds to the heavy atoms with acoustic modes of oscillation was estimated to be 380±5 K, and the Einstein temperature that corresponds to the light atoms with optical modes was estimated to be 670±9 K. The ratio of Debye and Einstein modes was estimated to be 3:2, which does not compare well with the ratio of heavier to lighter atoms (5:8). This demonstrates the flexibility of this fit, but the temperatures extracted do seem reasonable. The data can be seen to tend to the total specific heat value for this system of $3R$ per atom in the formula unit (13 atoms for $Co_3V_2O_8$). This fit was subtracted from the data below 50 K and the magnetic entropy recovered in the system was calculated. The entropy should reach the asymptotic value of $S_m(T \rightarrow \infty) = R\ln(2\mathbf{S}+1)$, where $\mathbf{S} = 3/2$ for Co^{2+}. However, the entropy is clearly a long way short of reaching this value. Very similar results were found by Yasui *et al.* [39] who suggested that the results can be understood by $Co_3V_2O_8$ possessing a Kramers doublet ground state. Kramers theorum states that a system which contains an odd number of electrons must possess at least a two-fold degeneracy in zero applied field. Co^{2+} has an odd number of 3d electrons and can be assigned a fictitious spin $\mathbf{S} = 1/2$ state. In this scenario, the entropy should reach a much lower value. The value found here is still only 75% of the total entropy expected for a $\mathbf{S} = 1/2$ state. This shortfall could be explained by the difficulties in obtaining reliable results when measuring around a first order phase transition using the relaxation method. From the zero applied field data shown in Figure 4.7, it can be seen that the transition at approximately 6 K causes problems for the instrumentation: the scans measuring up and down in temperature see quite a different intensity in the peak. The results of Rogado *et al.* [26] show a much more significant peak in specific heat at 6 K. It is quite probable that the measurements shown here did not capture the entire intensity of that transition, and that this missing intensity could easily account for the missing entropy.

All features observed in the $\chi(T)$ and $\mathbf{M}(\mathbf{H})$ curves for $\mathbf{H} \parallel b$ and $\mathbf{H} \parallel c$ are summarised in the magnetic phase diagram in Figure 4.4. The reduced symmetry and

large number of competing interactions in the system contribute to the complex nature of this diagram. It comprises multiple phases, which have been probed by neutron diffraction to enable magnetic structure determination.

4.3 Magnetic structure from powder measurements

4.3.1 In zero field

Recently, Chen *et al.* [23] have reported a detailed investigation of the magnetic ground state of $Co_3V_2O_8$ by powder and single crystal neutron diffraction. The investigation reveals that on cooling, a progressive transition from an incommensurate magnetic order to a ferromagnetic state exists along with a number of lock-in transitions related to commensurate antiferromagnetic order at intermediate temperatures. Contrary to what has been reported based on bulk properties measurements [24], the magnetic behaviour is totally different from what has been observed for the Ni counterpart [35]. This suggests different strengths of the interactions and the magnetic anisotropy [23].

The author has performed a powder neutron diffraction study of the antiferromagnetic incommensurate and ferromagnetic structures of $Co_3V_2O_8$ as a function of temperature and magnetic field, in collaboration with L. C. Chapon (ISIS Facility). The analysis of the data brings to light new aspects of the magnetic properties of this material. In particular, the large magnetic anisotropy and unsaturated Co moments in the ferromagnetic ground state. The results for the commensurate magnetic phases in zero-field are in perfect agreement with those reported by Chen *et al.* [23]. We further report the parameters extracted from Rietveld refinement of data in the high-temperature incommensurate region, showing a smooth variation of phase factors in the vicinity of the lock-in transition. In addition, neutron diffraction reveals that both incommensurate and ferromagnetic states are extremely sensitive to the application of a magnetic field. At 9 K, moderate magnetic fields destabilise the incommensurate magnetic state inducing a direct transition to a ferromagnetic state analogous to that found in zero-field at low

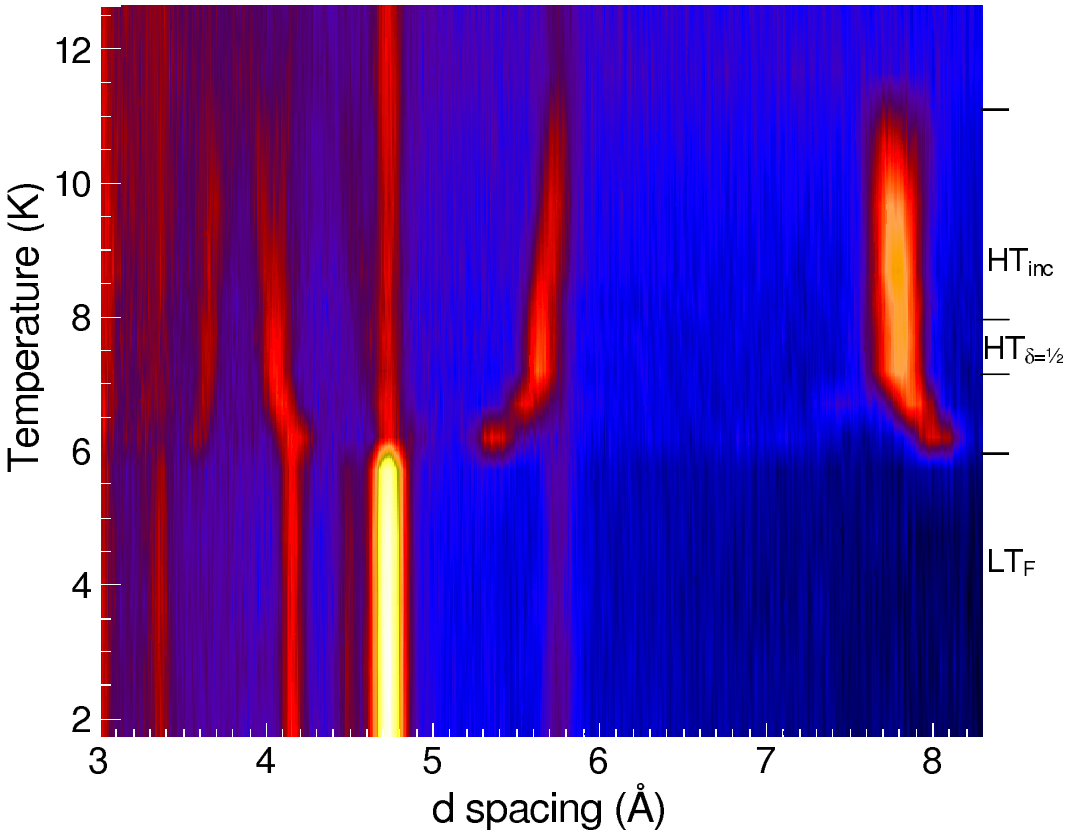

Figure 4.9: Neutron powder diffraction data of $Co_3V_2O_8$ taken on the GEM instrument at ISIS, UK. Line scans were taken at temperature intervals of 0.5 or 1 K and interpolated between. The colour scale ranges from dark blue representing the lowest scattered intensity, through red and yellow to white for the highest observed intensity. For example, the highest intensity observed at 4.7 Å has 100 counts in 1 hour, the background corresponds to approximately 20 counts and the peak at 4.15 Å at the lowest temperature has 35 counts. The different magnetic phases are indicated by the text on the right of the figure, see the main text for descriptions.

temperatures. A magnetic field applied in the low-temperature ferromagnetic state does not change the periodicity of the magnetic structure. However, the magnetic moment of the Co ion on the cross-tie site, that is considerably reduced in the zero-field structure, shows a net increase and eventually saturates at the same value as the Co spine moment. High-field data at low temperatures can be explained by a spin-reorientation process predominantly in the ac-plane, with different behaviours for the two Co sites.

Around 6 g of powder were used for the neutron experiment. Medium resolution neutron powder diffraction experiments were conducted on the GEM diffractometer at the ISIS facility of the Rutherford Appleton Laboratory, UK. Diffraction patterns were collected in zero-field at half degree intervals over the phase transition temperatures, and then at degree intervals over the remaining temperatures between 2 and 12 K. The counting time for each cryostat run was approximately 1 hour, using 160 μAh. The diffraction patterns in magnetic fields were collected using a 100 kOe Oxford Instruments superconducting magnet, these measurements ran for 300 μAh. Data were recorded at temperatures of 2 K and 9 K with increasing magnetic fields of 5, 15, 25, 40 and 80 kOe. For these in-field experiments, the sample was tightly packed into a vanadium can to avoid reorientation of the crystallites. Rietveld refinements were performed with the FullProf program [68]. Possible symmetry arrangements of the low-temperature magnetic structure were determined using representation analysis. The symmetry results are presented using Kovalev's notation [77].

$Co_3V_2O_8$ was found to order around 11 K, in agreement with previous reports [22, 23, 24, 26]. On cooling, it shows a complex sequence of phase transitions as indicated by the temperature dependence of the neutron diffraction pattern, shown in Figure 4.9. These data clearly demonstrate abrupt shifts in the positions and relative intensities of magnetic Bragg peaks. First, incommensurate magnetic ordering sets in with a propagation vector $\mathbf{k} = (0,\ \delta,\ 0)$, where $\delta = 0.54(1)$ at 9.7 K and decreases rapidly to lock at $\delta = \frac{1}{2}$ around 8.0 K. With further cooling, the structure becomes incommensurate again with a rapid decrease of δ. At 5.7 K, a sudden transition to $\mathbf{k} = (0,\ 0,\ 0)$ is

	Atoms					
Irreps.	Co(c-1)	Co(c-2)	Co(1-1)	Co(1-2)	Co(2-1)	Co(2-2)
Γ_1	(u_1,0,0)	(-u_1,0,0)ϕ	(0,v_2,0)	(0,-v_2,0)ϕ	(0,v_3,0)	(0,-v_3,0)ϕ
Γ_2	(0,v_1,w_1)	(0,v_1,-w_1)ϕ	(0,v_2,0)	(0,v_2,0)ϕ	(0,v_3,0)	(0,v_3,0)ϕ
Γ_3	(u_1,0,0)	(u_1,0,0)ϕ	(u_2,0,w_2)	(u_2,0,-w_2)ϕ	(u_3,0,w_3)	(u_3,0,-w_3)ϕ
Γ_4	(0,v_1,w_1)	(0,-v_1,w_1)ϕ	(u_2,0,w_2)	(-u_2,0,w_2)ϕ	(u_3,0,w_3)	(-u_3,0,w_3)ϕ

Table 4.1: Basis vectors for symmetry related Co ions of the cross-tie and spine sites belonging to irreducible representations of the little group G_k, Cmca with $\mathbf{k} = (0, \delta, 0)$, $\phi = exp(i\pi\mathbf{k})$. Labelling of the irreducible representations follow Kovalev's notation [77].

evidenced, again in excellent agreement with recent results [23].

The temperatures measured in each phase are as follows: the high temperature incommensurate phase (HT_{inc}) includes 10.7, 9.7 and 8.7 K; the high temperature $\delta = \frac{1}{2}$ phase ($HT_{\delta=\frac{1}{2}}$) includes 8.2, 7.7 and 7.2 K; the intermediate phase where δ rapidly decreases includes 6.7 and 6.2 K; and the low temperature ferromagnetic phase (LT_F) includes 5.7 K and below. Due to relatively large temperature steps (1 K) in our experiments, the exact temperature dependence including further lock-in transitions in the intermediate phase as reported by Chen *et al.* [23] could not be precisely mapped out. These were more clearly seen in the single crystal diffraction experiment discussed in Section 4.4.

Rietveld analysis of the magnetic structure has been performed in the HT_{inc} phase, the $HT_{\delta=\frac{1}{2}}$ phase and in the LT_F phase. The data and fits of representative temperatures from each of these phases are shown in Figure 4.10. In the temperature range 6.2 to 6.7 K, however, the presence of magnetic Bragg peaks indexed with third order harmonics of the propagation vector complicates the analysis. In particular, the fundamental reflection is only partially observed in the d-spacing range accessible from the lowest scattering angle detectors; the large peak occurs at 22.8 Å at 7.2 K, then moves up to 25 Å at 6.2 K.

Symmetry analysis of the magnetic structures for the HT_{inc}, $HT_{\delta=\frac{1}{2}}$ and the

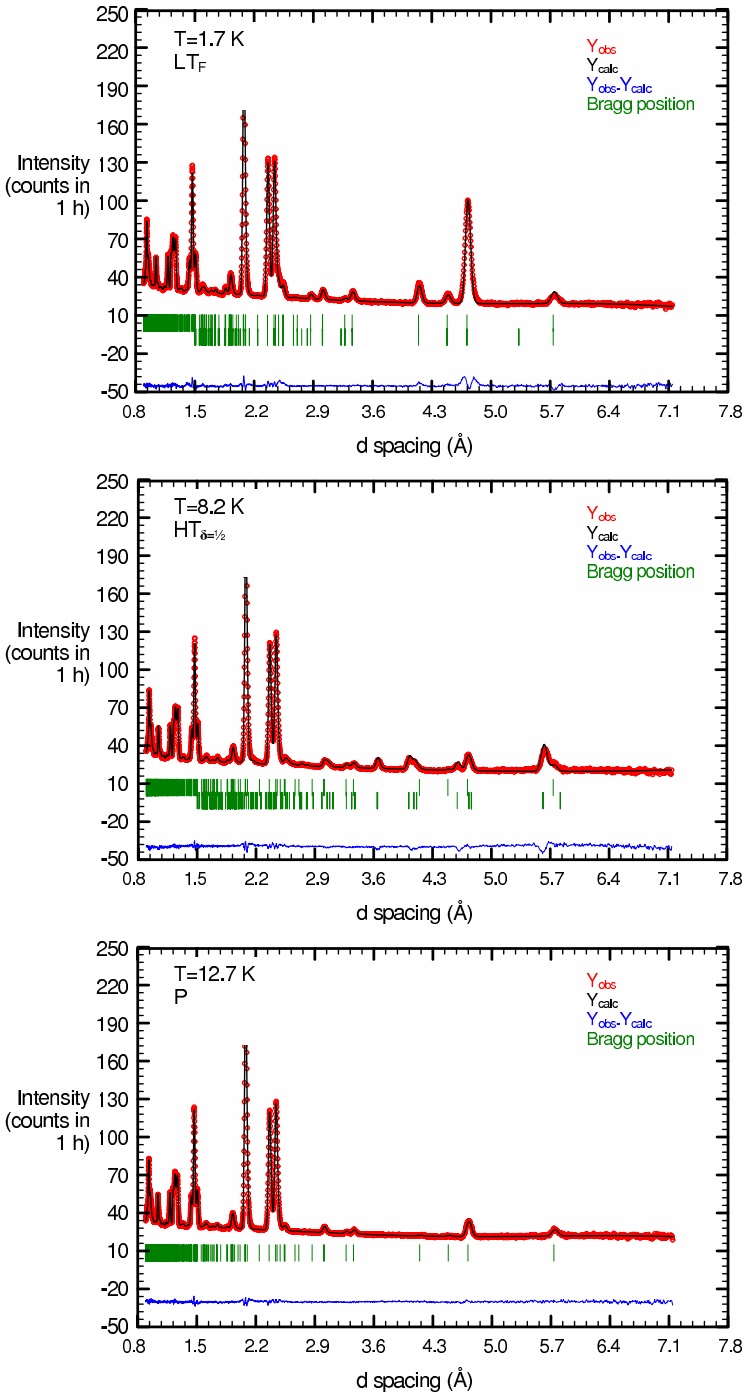

Figure 4.10: Examples of the refinement of neutron powder diffraction data of $Co_3V_2O_8$ performed using FullProf at 1.7, 8.2 and 12.7 K in the LT_F, $HT_{\delta=\frac{1}{2}}$ and paramagnetic phases respectively.

	Atoms					
Irreps.	Co(c-1)	Co(c-2)	Co(1-1)	Co(1-2)	Co(2-1)	Co(2-2)
Γ_1	(u_1,0,0)	(-u_1,0,0)	(0,v_2,0)	(0,-v_2,0)	(0,v_2,0)	(0,-v_2,0)
Γ_2	-	-	(0,v_2,0)	(0,v_2,0)	(0,-v_2,0)	(0,-v_2,0)
Γ_3	(u_1,0,0)	(u_1,0,0)	(u_2,0,w_2)	(u_2,0,-w_2)	(u_2,0,w_2)	(u_2,0,-w_2)
Γ_4	-	-	(u_2,0,w_2)	(-u_2,0,w_2)	(-u_2,0,-w_2)	(u_2,0,-w_2)
Γ_5	(0,v_1,w_1)	(0,v_1,-w_1)	(0,v_2,0)	(0,v_2,0)	(0,v_2,0)	(0,v_2,0)
Γ_6	-	-	(0,v_2,0)	(0,-v_2,0)	(0,-v_2,0)	(0,v_2,0)
Γ_7	(0,v_1,w_1)	(0,-v_1,w_1)	(u_2,0,w_2)	(-u_2,0,w_2)	(u_2,0,w_2)	(-u_2,0,w_2)
Γ_8	-	-	(u_2,0,w_2)	(u_2,0,-w_2)	(-u_2,0,-w_2)	(-u_2,0,w_2)

Table 4.2: Basis vectors for symmetry-related Co ions of the cross-tie and spine sites belonging to irreducible representations of the space group Cmca. Labelling of the irreducible representations follows Kovalev's notation. The absence of modes for irreducible representations not appearing in the decomposition of the magnetic representation is indicated by the "-" sign.

LT_F phases have been performed using representation analysis. The labelling of atomic positions for cross-tie and spine sites is shown in Figure 1.5 and Table 1.1. Analysis of the magnetic configurations for atomic sites generated from c-centering translation of the labelled positions is not explicitly reported but can be easily calculated by including the phase factor $2\pi\mathbf{k}\cdot\mathbf{T}$ where $\mathbf{T} = (\frac{1}{2}, \frac{1}{2}, 0)$. For the HT structures ($\mathbf{k}$=$\mathbf{k}_8$ in Kovalev's notation) only the screw-axis along y, mirror plane perpendicular to x and b glide plane perpendicular to the z-axis are valid operators in the little group [77]. The loss of symmetry operators indicate that the four equivalent positions for the Co spine sites split into two orbits, Co(1-1) with Co(1-2) and Co(2-1) with Co(2-2). The two Co cross-tie sites, Co(c-1) and Co(c-2) belong to the same orbit. Basis vectors of the HT magnetic structures are reported in Table 4.1 for the four irreducible representations labelled $\Gamma_i (i$ =1,4), they are all mono-dimensional. In agreement with the results of Chen *et al.* [23], we found that only Γ_3 fits the experimental data with moments along the a-axis. There is no canting along the c-axis within the resolution of our experiment.

Although the Co spine sites split into two orbits, co-representation analysis including the complex conjugation operator constrain the moment on both orbits to be

the same. However, there are no symmetry constraints as such for the phase differences. Therefore, in addition to a global phase factor, set to be 0 on the first Co(c-1) site, there are two phases to be refined describing the relative phasing of the two spin-density waves on the Co(1-1)/Co(1-2) and Co(2-1)/Co(2-2) orbits with respect to the Co(c) wave. These phases, in units of 2π radians, were found to be 0.18(5) and 0.09(5) at 8.2 K where the propagation vector locks at the commensurate value $\delta = \frac{1}{2}$. The results of Chen *et al.* [23] can be reproduced by adding a global phase of 0.25 to the values reported here.

On warming the sample the phase values increase and at 10.7 K, where $\delta = 0.54$, they reach 0.27(5) and 0.15(5) for the two spin-density waves respectively. The magnetic structure at 9.7 K in the HT_{inc} phase is presented in Figure 4.11. It is similar to that found in the $HT_{\delta=\frac{1}{2}}$ phase, the low magnetic moments on cross-tie sites are located in layers for which adjacent spine chains are aligned antiferromagnetically. At 8.2 K, the amplitude of the waves were found to be 1.1(2) and 2.99(2) μ_B on the Co cross-tie and Co spine sites respectively. Whereas the expected value for high spin Co^{2+} in an octahedral configuration (spin only) is achieved on the spine site, there is a marked reduction of the moment on the cross-tie site indicating large fluctuations even in the commensurate $HT_{\delta=\frac{1}{2}}$ phase. At 10.7 K the amplitudes of the waves decrease to 0.90(18) and 1.99(4) μ_B respectively.

Next we consider the LT_F magnetic phase. Symmetry analysis is now performed in the group Cmca since all symmetry operators belong to the little group for $\mathbf{k} = 0$. There are eight one-dimensional representations in this case and the atomic positions for each Co site belong to the same orbit. The projected basis vectors are shown in Table 4.2. Although the transition to the ferromagnetic state is first order and Landau theory does not restrain the magnetic modes to belong to the same irreducible representation in this case, the data below 5.7 K are consistent with a ferromagnetic structure described by a single representation, Γ_3. Similar to the HT structure, the magnetic moments are directed along the a-axis. A weak canting along c, allowed by

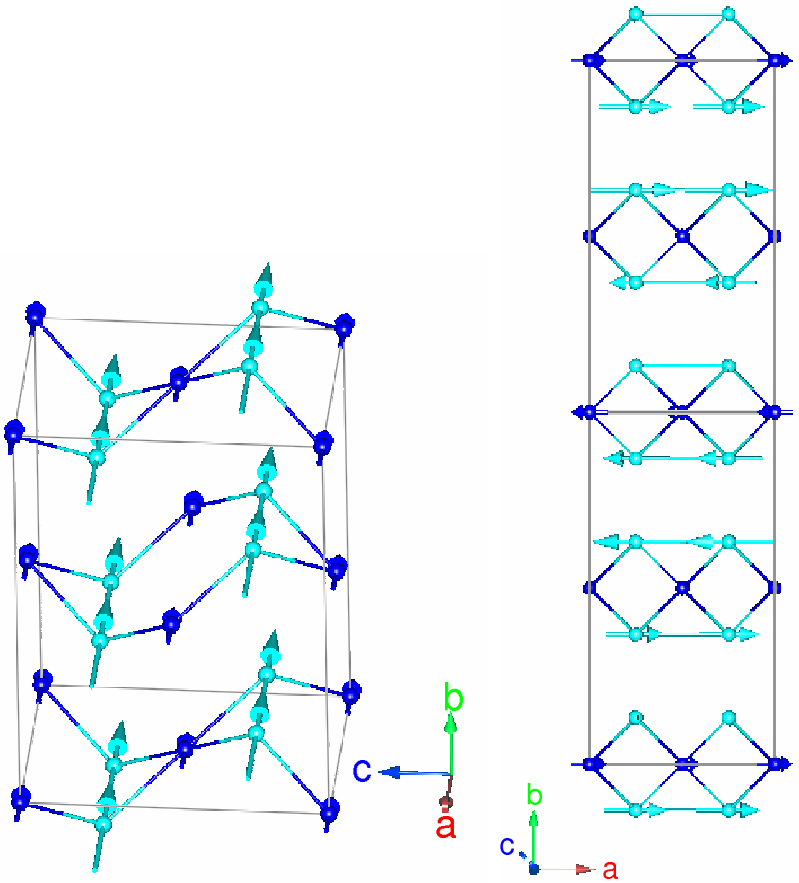

Figure 4.11: Proposed magnetic structure of $Co_3V_2O_8$ in the LT_F (left) and HT phases (right). The Co spine site is shown in light blue, and the cross-tie site is shown in darker blue. All moments lie along the a-axis.

symmetry, is not excluded since the data shows a weak hump around the (1 1 0) Bragg position. However, the contribution is too small to extract a sizeable component along this direction. The extracted moments at 2 K are 1.81(4) μ_{B} and 3.04(2) μ_{B} on the cross-tie and spine sites respectively. Between 2 K and 5.7 K, there are no noticeable variations of the magnetic moment. Again, the moment on the cross-tie site is largely reduced with respect to the expected spin contribution of 3 μ_{B} and the average saturated Co moment from magnetisation measurements of 3.6 μ_{B} [35].

4.3.2 In an applied field

To gain further insight into the magnetic behaviour of $Co_3V_2O_8$, powder neutron diffraction experiments in magnetic fields have been conducted. First, the field was applied at 9 K where the system is in the HT_{inc} phase. The data are presented in Figure 4.12. At 5 kOe, we observe a shift in the positions of magnetic Bragg peaks, indicating a change in propagation vector of 0.02 even at this moderate field value. Simultaneously, new magnetic Bragg peaks appear, indexed at $\mathbf{k} = 0$. In particular, we notice a strong increase of the (0 2 1) reflection (see inset of Figure 4.13). With further increase of the magnetic field, the incommensurate magnetic state completely disappears leaving an essentially pure ferromagnetic pattern, similar to that observed for the LT_F structure in zero-field. However, the relative intensities of several magnetic Bragg peaks are different from the zero-field data and vary with increasing magnetic field: the (1 1 1), (0 2 0) and (0 2 1) peaks increase continuously between 15 and 80 kOe suggesting a possible spin-reorientation.

Applied field neutron diffraction patterns collected in the LT_F state at 2 K are also presented in Figure 4.12. No additional magnetic reflections appear, indicating that the $\mathbf{k} = 0$ structure is stable under application of magnetic fields up to 80 kOe. However, we observe a redistribution of the scattering intensities (see inset of Figure 4.13): the (1 1 1) and (0 2 0) peaks strongly increase with field. In addition, the integrated intensity of the (1 1 1) reflection, increases from being smaller than the (0 2 0) integrated intensity

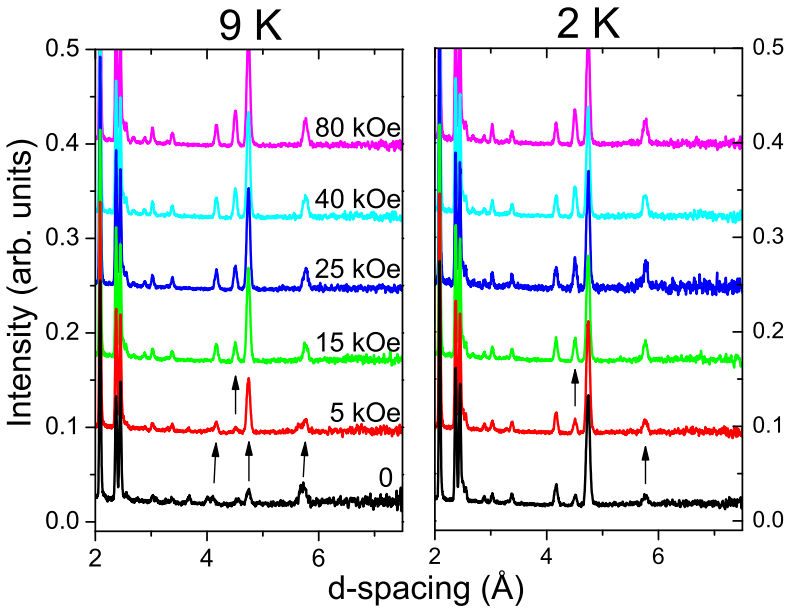

Figure 4.12: Neutron powder diffraction data at 9 K (left) and 2 K (right) in magnetic fields of 0, 5, 15, 25, 40, and 80 kOe. The data is from a bank of detectors situated at the scattering angle 35°. The arrows indicate the changes between the data at different fields. Individual curves are offset arbitrarily for display purposes.

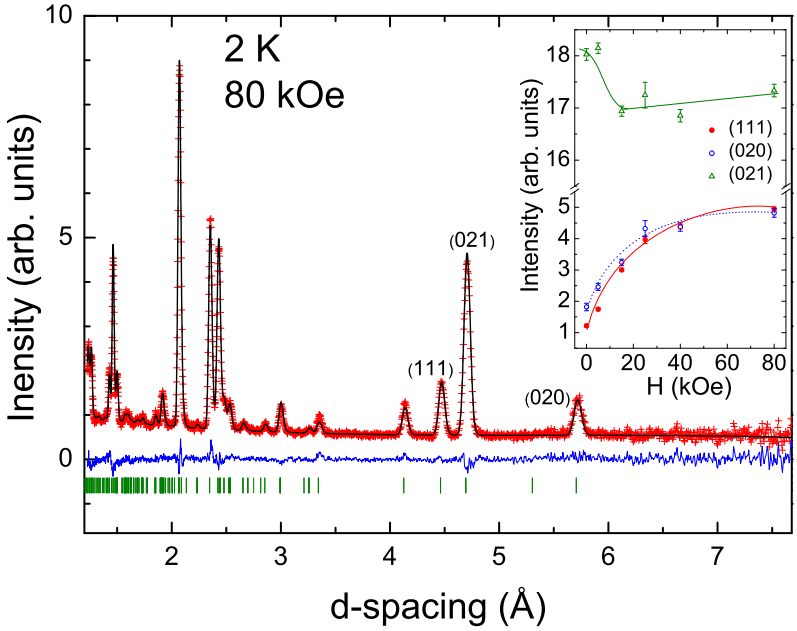

Figure 4.13: Rietveld refinement of the nuclear and magnetic structure of $Co_3V_2O_8$ at 2 K and 80 kOe. Inset: Integrated intensities of selected reflections as a function of magnetic field. Curves are guides to the eye only.

at 0 kOe, to slightly higher at 80 kOe. At the same time, the intensity of the strongest magnetic peak (0 2 1) does not vary up to 5 kOe, and only decreases slightly for higher field values.

The initial attempt at modeling the diffraction data in magnetic fields was made with identical arrangements to the zero-field LT_F structure, allowing only the magnetic moment on both sites to vary. This model led to an enhancement of the magnetic moments on the Co cross-tie site but failed overall to accurately reproduce the experimental data, resulting in a poor agreement factor for the magnetic phase of $\mathrm{R_{Mag}}$ =16.8%. Subsequent analysis showed that the data are best reproduced with a model in which the spins of both Co sites are allowed to rotate in the ac-plane. This corresponds to a structure where modes belonging to the irreducible representation Γ_3 along a and Γ_7 along c

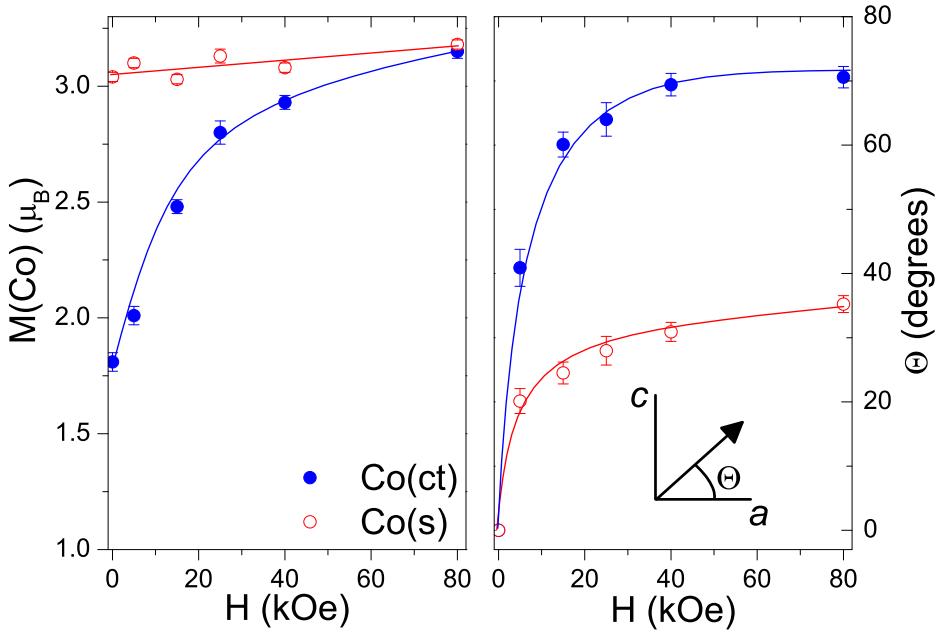

Figure 4.14: The dependence of the low-temperature magnetic structure parameters on magnetic field extracted from Rietveld refinements. Left panel: magnetic moments on the cross-tie (Co(ct)) site and spine site (Co(s)). Right panel: angular deviation of spins in the ac plane for the cross-tie site. $\Theta = 0$ corresponds to a collinear structure with spins lying along the a-axis. Curves are guides to the eye only.

are mixed. The agreement with the experiment is very good, as shown by Figure 4.13; a reliability factor of $\mathrm{R_{Mag}}$ =8.8% is obtained for Rietveld refinement of the data collected at 80 kOe.

Two essential characteristics can be extracted from the refinement, these are summarized in Figure 4.14. Firstly, the magnetic moment on the Co cross-tie site increases rapidly with application of the magnetic field and saturates at 3.15(3) μ_{B} at 80 kOe. In zero field the moment magnitude is only 57% of the fully saturated value observed in an applied field of 80 kOe. The magnetic moment on the Co spine site barely changes with field and is refined at 3.18(2) μ_{B} at 80 kOe. Both values agree well with the expected spin-only contribution for high-spin octahedral Co^{2+}. It is clear that

one must be cautious when reporting analysis of this kind due to the intrinsic limitations of the experiment with polycrystalline samples. However, semi-quantitative information can be accessed because a large $\mathbf{Q}$-range is probed, a condition not realized for single-crystal instruments due to the geometrical constraints imposed by a cryomagnet.

Secondly, the refinement clearly indicates a re-orientation of the spins in the ac-plane in an applied field. With powder experiments, extracted moment directions are averaged over all possible orientations of the field with respect to the crystal axes. From magnetisation measurements [22, 24, 35] it has been shown that the b-axis of this material is clearly the hard axis. The magnetisation is an order of magnitude smaller than that from the c-axis, which is a further order of magnitude smaller than that of the a-axis. For an ideal ferromagnetic material for which a and c are equally easy directions and the b axis is perfectly hard, one can expect that the magnetic moments will be fully polarized along the applied field irrespective of the field direction in the ac-plane. For such an idealised material, a powder measurement integrated over all possible orientations would show an average moment direction pointing at 45° in the ac-plane. In $Co_3V_2O_8$, however, the moment orientation on the spine site is approximately 35°; less than the expected 45° value, while the moment orientation angle of the cross-tie site is much higher than expected. From the zero field and magnetisation data presented here, it is clear that the a-axis is the easy axis of the system. However, on application of a magnetic field the c-axis becomes an easier direction than the a-axis for the Co cross-tie site.

In the LT_F phase, the cross-tie moments are not as large as expected and lie along the a-axis parallel to the fully saturated spine site moments. In an applied field of 80 kOe, the cross-tie moments have reached the expected saturation value and point more along the c-axis than the a-axis. The spine site moments have also re-orientated to have a larger component along the c-axis than in zero field, but not as much as the cross-tie moments. This suggests that the single ion anisotropies for the two sites are different and that the application of a field may influence the two moments in different

ways.

One should discuss this behaviour qualitatively and in the limits of the model approximations, in particular the hypothesis of a perfectly hard direction along b (obviously not fulfilled). Overall, these results are in good agreement with magnetisation measurements showing that a and c are definitely easy-directions in $Co_3V_2O_8$ [22, 35]. The fact that the moment on the cross-tie site increases rapidly from the reduced 1.81(4) μ_B value is also in agreement with the fully polarized ferromagnetic structure observed in magnetisation measurements in moderate magnetic fields. The slightly different anisotropies for both Co sites suggested by our neutron experiments could explain the different magnetic behaviours observed when the field is applied along c and a.

4.4 Magnetic structure from single crystal measurements

Single crystal diffraction was performed on the D10 diffractometer at the ILL, Grenoble, France. A single crystal of size 4 mm×2 mm×2 mm was aligned in the four circle Eulerian cradle of the instrument. A He-flow cryostat was used and the detector was position sensitive, of size 80 mm×80 mm. Measurements were performed with $\mathbf{k}_i$=1.5325 Å^{-1} and $\mathbf{k}_i$=2.3621 Å^{-1}, for the shorter wavelength a longer evacuated incident beam tube was mounted. A pyrolitic graphite filter and monochromator were used for the longer wavelength, for the shorter wavelength a Cu (2 0 0) monochromator was used, still with the graphite filter.

Tables of integrated intensities of Bragg peaks were produced in the paramagnetic (1) and the LT_F (5) phases. The numbers given here with each phase identify the regions in Figure 4.15. An extra phase was also discovered with intensities on the sites of Bragg peaks forbidden by the c-centring symmetry restriction, this phase is labelled the $HT_{\delta=\frac{1}{3}}$ (4) phase and appears between 5.8 and 6.1 K in zero applied field. An example of the Bragg peaks observed in the $HT_{\delta=\frac{1}{3}}$ (4) phase is shown in Figure 4.16. Integrated intensities were also gathered for this phase.

The program FullProf was used to refine the nuclear and magnetic structures in

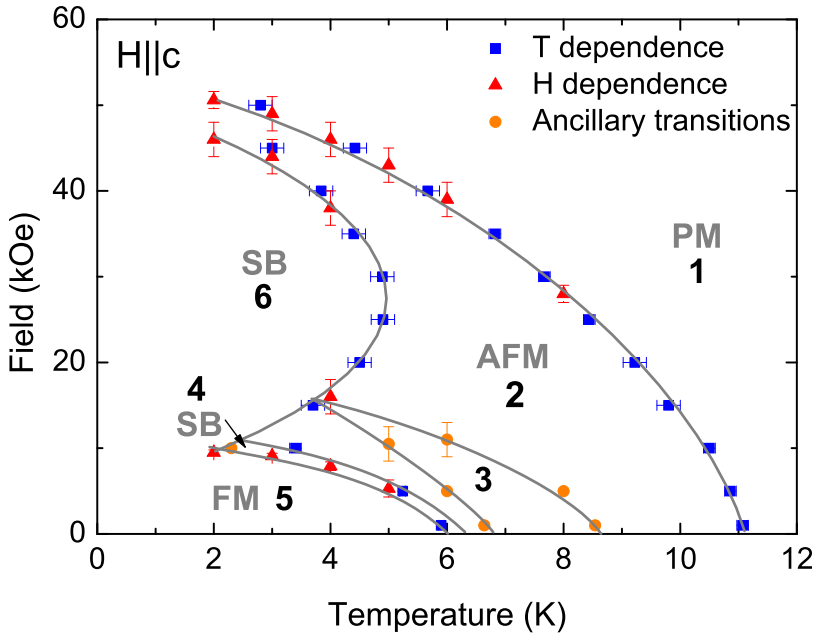

Figure 4.15: The phase diagram of $Co_3V_2O_8$ with the different phases investigated by single crystal neutron diffraction labelled. The lines are only drawn as guides to the eye. For a description of each phase, see the main text. The phases are the paramagnetic, HT_{inc}, $HT_{\delta=\frac{1}{2}}$, $HT_{\delta=\frac{1}{3}}$, LT_F and a region that exists only in applied fields with peaks at c-centring symmetry breaking positions but no satellite peaks (labelled SB number 6).

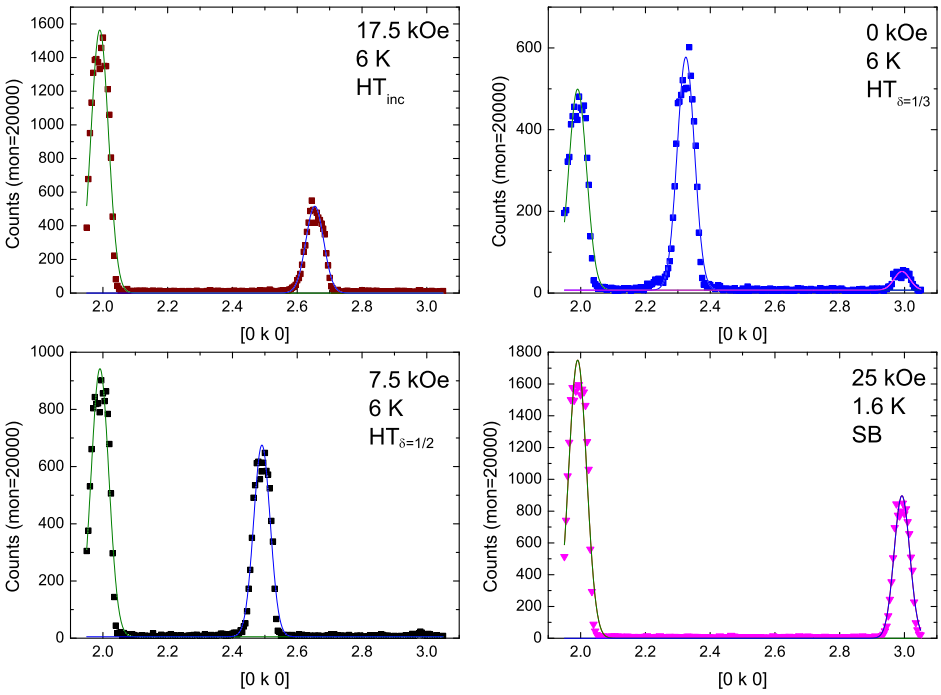

Figure 4.16: The Bragg peaks observed in the different magnetic phases of $Co_3V_2O_8$. The four represented are the HT_{inc}, $HT_{\delta=\frac{1}{2}}$, $HT_{\delta=\frac{1}{3}}$ and a region that exists only in applied fields with peaks at c-centring symmetry breaking positions but no satellite peaks (labelled SB). See Figure 4.15 to refer these phases to the phase diagram.

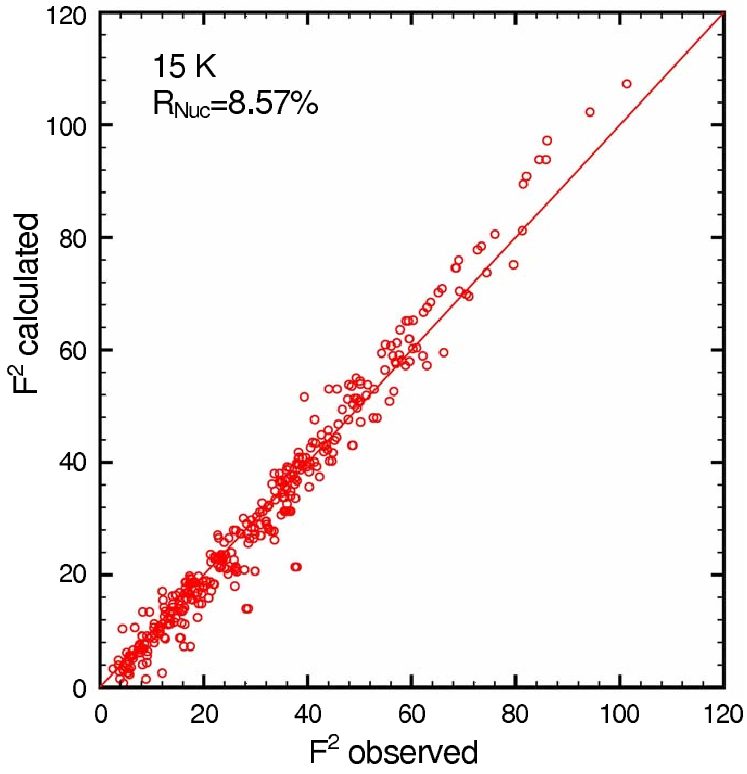

Figure 4.17: The correlation between the calculated and observed structure factors in the refinement of single crystal neutron diffraction data in the paramagnetic phase. The quality of the fit is given by the $\mathrm{R_{Nuc}}$ at 8.57%.

the paramagnetic, LT_F, and $HT_{\delta=\frac{1}{3}}$ phases. Figure 4.17 shows the correlation between the calculated and measured structure factors for the paramagnetic phase. The fit has a $\mathrm{R_{Nuc}}$ value of 8.57%. The lattice parameters were fixed to be 6.0311, 11.4879 and 8.3066 Å for a, b, and c respectively from the UB matrix of the diffraction measurements. These values compare well with those of Sauerbrei *et al.* [32] at 6.030(4), 11.486(2) and 8.312(5) Å. The refined parameters are the atomic positions, the isotropic temperature factors of all atoms except for vanadium (due to its large incoherent scattering contribution), and the scale factor. The integrated intensities were calculated using the Racer program [78] and converted to a form suitable for FullProf using DataRed, available in the FullProf Suite of programs.

Using the nuclear parameters from the refinement in the paramagnetic phase and the values of the magnetic and symmetry parameters from the powder diffraction refinement as fixed values, the LT_F phase was refined. The correlation between measured and calculated structure factors has a $\mathrm{R_{Mag}}$ value of 8.13%. This is an emphatic confirmation of the structure already determined by powder diffraction.

The magnetic structure in the $HT_{\delta=\frac{1}{3}}$ phase has been partially refined. All peaks except those at positions forbidden by symmetry restrictions were used to give the refined structure shown in Figure 4.18. The structure has a propagation vector of $(0,\ 1/3,\ 0)$ and the model gives a $\mathrm{R_{Mag}}$ value of 14.31%. Not all of the peaks were used in the refinement due to difficulties in modeling peaks at forbidden positions. The unused peaks could theoretically be fitted with a propagation vector of (0, 1, 0). They have positions [and integrated intensities] such as: (0 1 0) [258], (0 3 0) [135], (0 5 0) [164] and (2 5 0) [101]. All positions with $h + k$=odd were investigated but only those corresponding to allowed positions plus **k**=$(0,\ 1,\ 0)$ had significant intensity. For example, the (1 2 0), (1 2 2), (3 2 0) and the (3 2 2) peaks all have integrated intensities of less than 30. This extra detail to the structure would act to square the modulation of the moment magnitudes.

From the magnetic structure refinements in the magnetic phases it was discov-

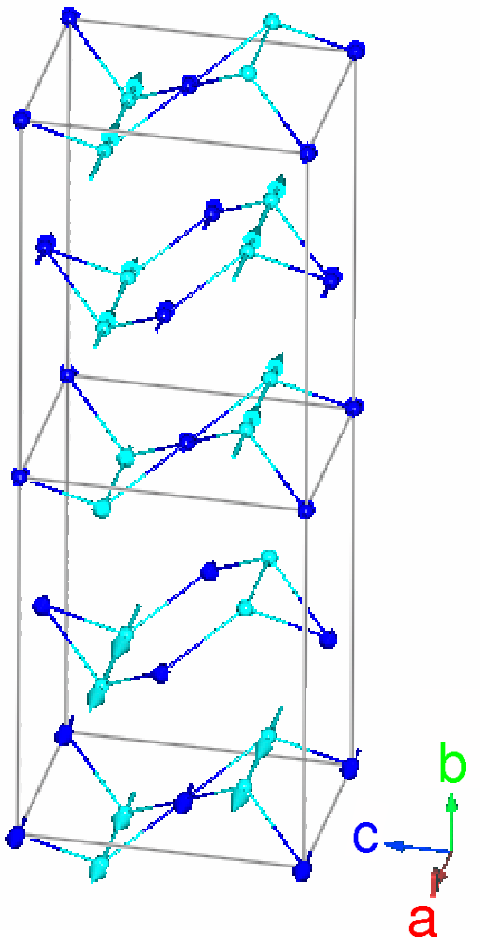

Figure 4.18: The proposed magnetic structure of $Co_3V_2O_8$ in the c-centring symmetry breaking phase with propagation vector $(0,\ 1/3,\ 0)$ between 5.8 and 6.1 K.

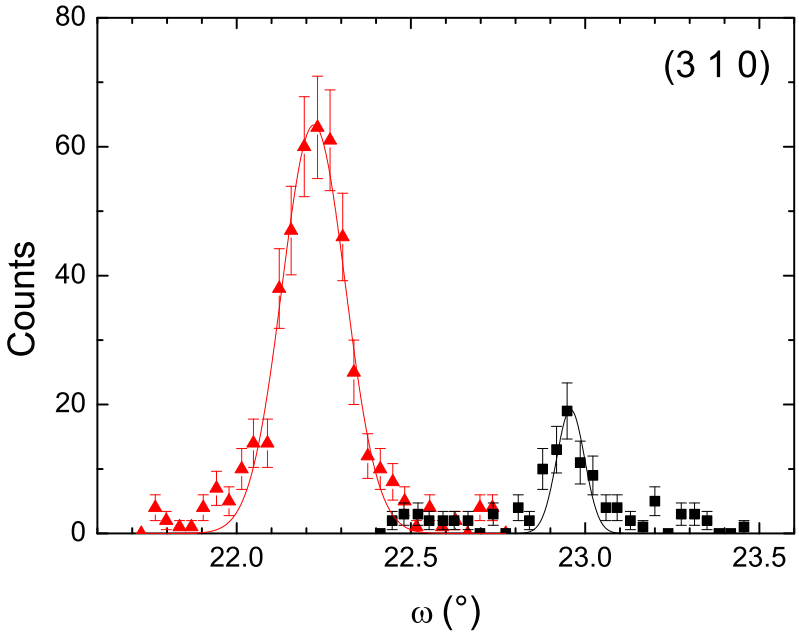

Figure 4.19: The intensity of the (3 1 0) Bragg peak at two different rotations about the scattering vector. The peaks are shown at different positions on the x-axis as this rotation causes an adjustment to be made to the alignment of the sample (ω) so as to remain centred on the peak. The difference in intensity shows that a significant contribution comes from multiple scattering.

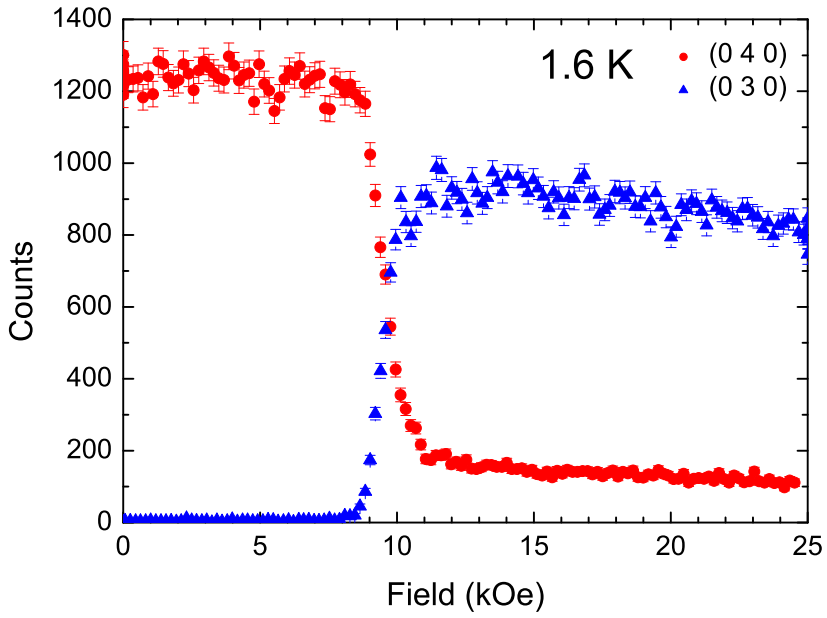

Figure 4.20: The intensities of the Bragg peaks (0 4 0) and (0 3 0) as a function of applied magnetic field at 1.6 K. The data clearly shows the transition to a phase with peak intensities at c-centring symmetry breaking positions. The sample was aligned with $\mathbf{H} \parallel c$.

ered that a small number of peaks had poor correlations between their measured and calculated structure factors. These peaks were identified as most likely being formed through multiple scattering events. To determine the extent of multiple scattering, the sample was rotated about the scattering vector and the change in intensity of specific Bragg peaks was observed. The results of the scans are shown in Figure 4.19. The change in intensity of the (3 1 0) peak clearly shows that there is a significant contribution to the peak from multiple scattering. It is simple to ignore peaks that should be extinct but have a multiple scattering contribution. It is however, much more difficult to know how much intensity comes from multiple scattering in non-extinct peaks. This is an error that must be taken into account when considering the accuracy of refinements and proposed structures from single crystal diffraction data.

The sample was put in various applied fields using a 25 kOe vertical field cryomagnet. Two scattering planes were investigated; [0 k l] with $\mathbf{H} \parallel a$ and [h k 0] with $\mathbf{H} \parallel c$, only the latter contributed any new information to the phase diagram. It was discovered that the symmetry breaking phase observed between 5.8 and 6.1 K in zero applied field exists up to around 10 kOe. It continues to occupy a very narrow region in the phase diagram; it closely follows the first order transition from the HT_{inc} to the LT_F phase. The symmetry breaking region is labelled number 4 in Figure 4.15.

Another symmetry breaking phase was also found; the area at low temperatures and intermediate applied fields for $\mathbf{H} \parallel a$, labelled SB number 6 in Figure 4.15. This area has c-centring symmetry breaking peaks, but no observed satellite peaks from non zero propagation vectors. Figure 4.20 shows the variation in two Bragg peaks as the transition to this phase is crossed by increasing the applied field from the LT_F phase. The (0 3 0) peak is the c-centring symmetry breaking peak (as $h + k$=odd) and the (0 4 0) is an allowed peak with a large magnetic contribution. The decrease in intensity of the allowed magnetic peaks implies that the peaks at symmetry breaking positions are also magnetic and a sharp restructuring is happening at this phase transition. These peaks could then be produced by a magnetic structure with a propagation vector of (0, 1, 0). It is surprising to see a new phase appear only in applied fields, especially one that has magnetic Bragg peaks forbidden by symmetry restrictions. This new phase means a very complex series of transitions from the LT_F phase on application of a magnetic field. At 4.5 K, this ferromagnetic phase gives way to the $HT_{\delta=\frac{1}{3}}$ phase, then the HT_{inc} and $HT_{\delta=\frac{1}{2}}$ phases before entering this completely new phase with forbidden peaks. The magnetic structure then briefly re-enters the HT_{inc} phase before changing state yet again. It has also been suggested by Yasui *et al.* [39] that another phase with propagation vector (0, $2/3$, 0) exists in a narrow region next to the boundary of the $HT_{\delta=1}$ phase. No evidence was found for this phase during our D10 experiment, but this is not surprising considering the very narrow temperature range of the phase.

4.5 Magnetic excitations

The PRISMA instrument was used in both of its configurations to first map out the Bragg peaks observed, then to probe the magnetic excitations. The instrument was operating with a nimomic chopper to reduce the noise at very short flight times. The disc chopper was running at 50 Hz, and the standard PRISMA collimation was used: 30' for the elastic arm and 60' for the inelastic arm. A crystal approximately 2 cm^3 in volume was used for the experiment. The instrument jaws were tightened, their separations were 33 and 16 mm for the top/bottom and east/west jaws respectively. Figure 4.21 shows the reciprocal space maps at 25, 9 and 1.3 K. The fourth map shows the difference between the paramagnetic (25 K) and base temperature maps. It is evident from these figures that the crystal used had some twinning. These maps gave the first approximation of the propagation vector found in the HT_{inc} phase and were invaluable in later experiments. They provide clear evidence as to which magnetic Bragg peaks are strongest and most suitable to study.

To investigate the excitations, scans were performed either in the [0 k k] direction around the magnetic (0 4 0) peak or in the direction parallel to the [0 k $k/4$] line and passing through the ferromagnetic Bragg peak at (0 2 3) (as shown in Figure 4.22). The more obvious choice of a scan in the direction [0 k 0] could not be performed due to restrictions in PRISMA's geometry. Figure 4.22 suggests that multiple branches of the spin-waves may exist in this compound. For the lowest branch the observed gap at the zone centre is about 1.3 meV. The highest energy of this branch is 2.3 meV at the zone boundary. The relatively small amplitude of the energy variation compared to the gap suggests that the strength of exchange interactions in this compound is comparable with the single-ion anisotropy. This observation is consistent with the results of measurements of magnetic susceptibility where an unusually large difference (up to a hundred times) in $\chi(T)$ was found for different directions of magnetic field. Due to the different magnetic moment magnitudes of the two Co^{2+} sites in the unit cell it is not surprising that the excitation spectrum of $Co_3V_2O_8$ consists of more than one branch.

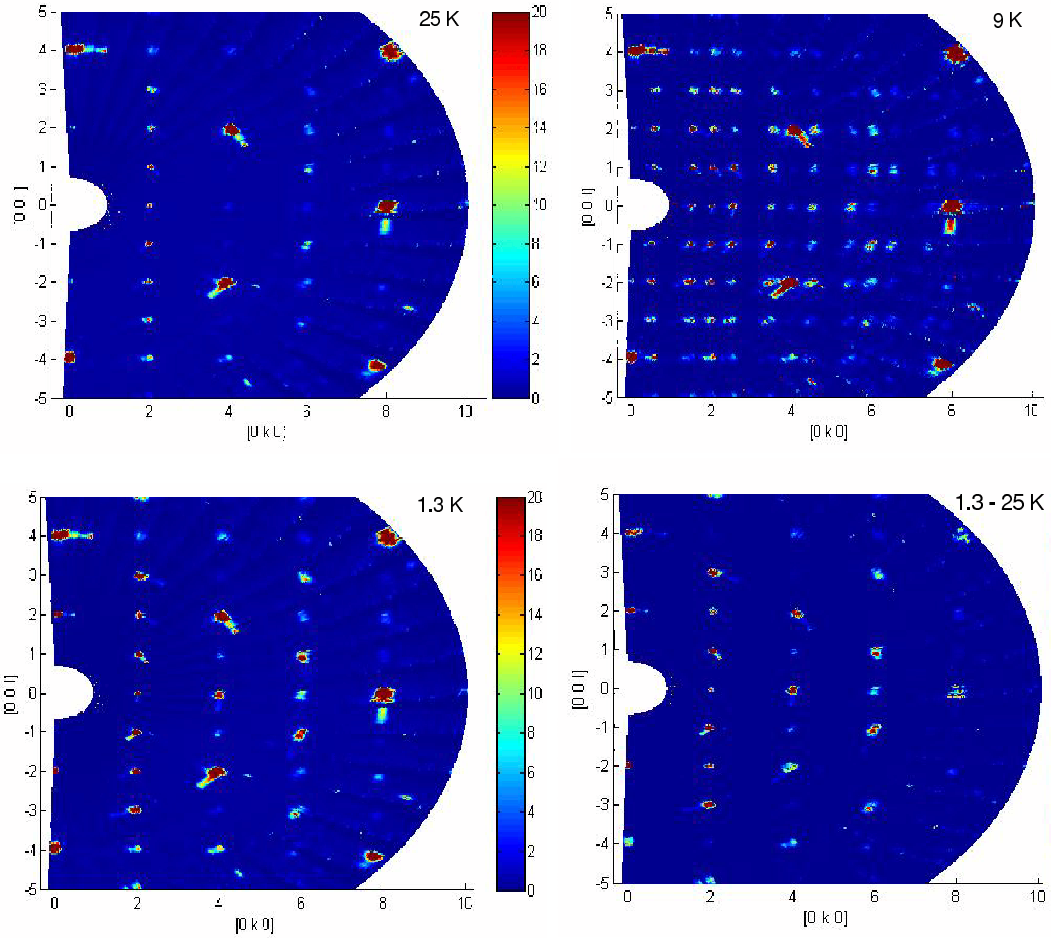

Figure 4.21: Reciprocal space maps of $Co_3V_2O_8$ in the [0 k l] plane. Measurements were taken with the PRISMA instrument in the paramagnetic (25 K), HT_{inc} (9 K) and LT_F (1.3 K) phases of $Co_3V_2O_8$. Also shown is the difference between the paramagnetic and LT_F phase to demonstrate the magnetic contribution to the pattern.

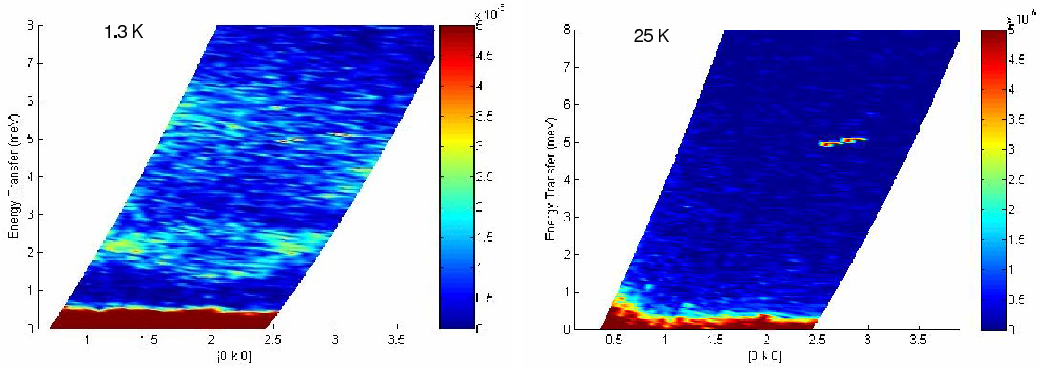

Figure 4.22: Inelastic single crystal neutron measurements taken at 25 K in the paramagnetic phase and 1.3 K in the LT_F phase using the PRISMA instrument at ISIS. Magnetic excitations are observed in the LT_F phase, the paramagnetic phase shows no excitations proving that those observed in the LT_F phase are magnetic in origin. The high intensity spots at approximately 5 meV in both data sets are caused by electronic noise in one of the detectors.

Measurements of the excitation spectrum were attempted at $T = 9$ K around the magnetic Bragg peaks (0 2.5 1) and (0 1.5 2). Although the magnetic excitations are still visible, their energy is significantly lower when compared to the ferromagnetic phase, making it difficult to separate the inelastic and quasi-elastic signals. Measurements on an instrument with improved energy resolution would be required for a detailed study of excitations in the antiferromagnetic phase of $Co_3V_2O_8$.

The cold neutron triple-axis spectrometer 4F1 at the LLB was used to further investigate the excitations. An improved crystal was used for this experiment which was performed in the W configuration [79]. Using this set-up, looking down on the experiment the path of the neutrons traces a W shape. Three configurations were used with a vertically focusing monochromator and horizontally focusing analyser. The settings were: $\mathbf{k}_f$=2.662 Å^{-1} with a pyrolitic graphite filter on $\mathbf{k}_f$ and a resolution width of 1.367(5) meV, $\mathbf{k}_f$=1.970 Å^{-1} with a pyrolitic graphite filter on $\mathbf{k}_f$ and a resolution width 0.536(3) meV and finally $\mathbf{k}_f$=1.550 Å^{-1} with a Be filter on $\mathbf{k}_f$ with a resolution width of 0.234(1) meV. The sample had a volume of approximately 2 cm^3

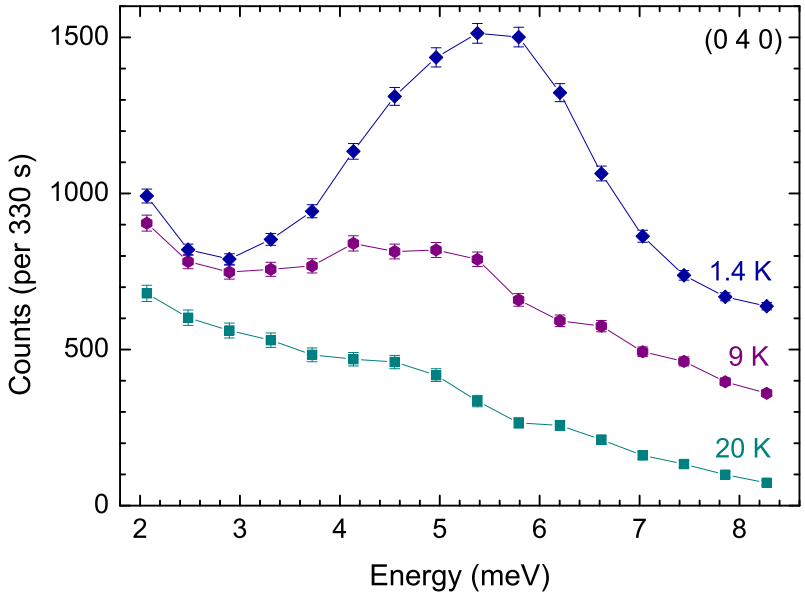

Figure 4.23: A comparison of the excitations observed in the different magnetic phases of $Co_3V_2O_8$. The energy scans were centred on the commensurate Brillouin zone centre (0 4 0) using the 4F1 spectrometer at the LLB. The upper scans have each been offset by 250 counts for clarity.

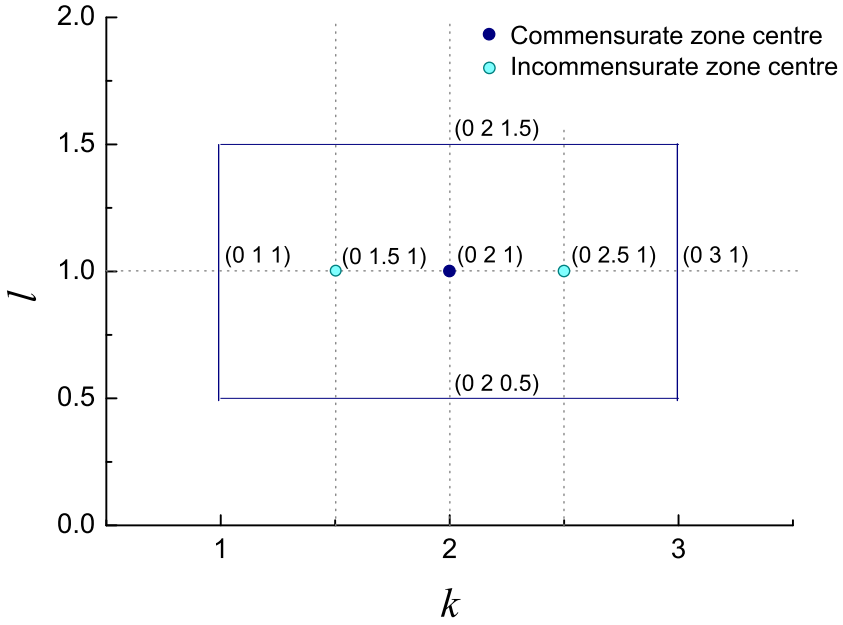

Figure 4.24: The Brillouin zone of $Co_3V_2O_8$ in the [0 k l] plane. Magnetic excitations were investigated along the [0 k 1] and [0 2 l] directions between the zone centres and boundaries.

and the mosaic spread of this crystal (not the crystal used on PRISMA) was found to be less than 0.5° (the resolution limit of the instrument). The sample was mounted in an Orange Cryostat capable of reaching 1.4 K. The energy range investigated was 0 to around 6 meV in the scattering plane [0 k l]. Figure 4.23 shows a comparison of the excitations observed around the (0 4 0) Bragg peak at decreasing temperatures. At the base temperature of 1.4 K the excitations are strongest, but evidence for the appearance of the excitations can also be seen at the intermediate temperature.

The sample was investigated in detail at 1.4 K. Multiple excitations were observed across the Brillouin zone in the two directions [0 k 1] and [0 2 l]. Shown in Figure 4.25 are the best Gaussian fits to the excitations observed in the [0 k 1] direction at 1.3 K. The zone centre is at (0 2 1) and the boundary at (0 1 1), a sketch of the Brillouin zone is shown in Figure 4.24. Up to four excitations branches were observed, reduced to

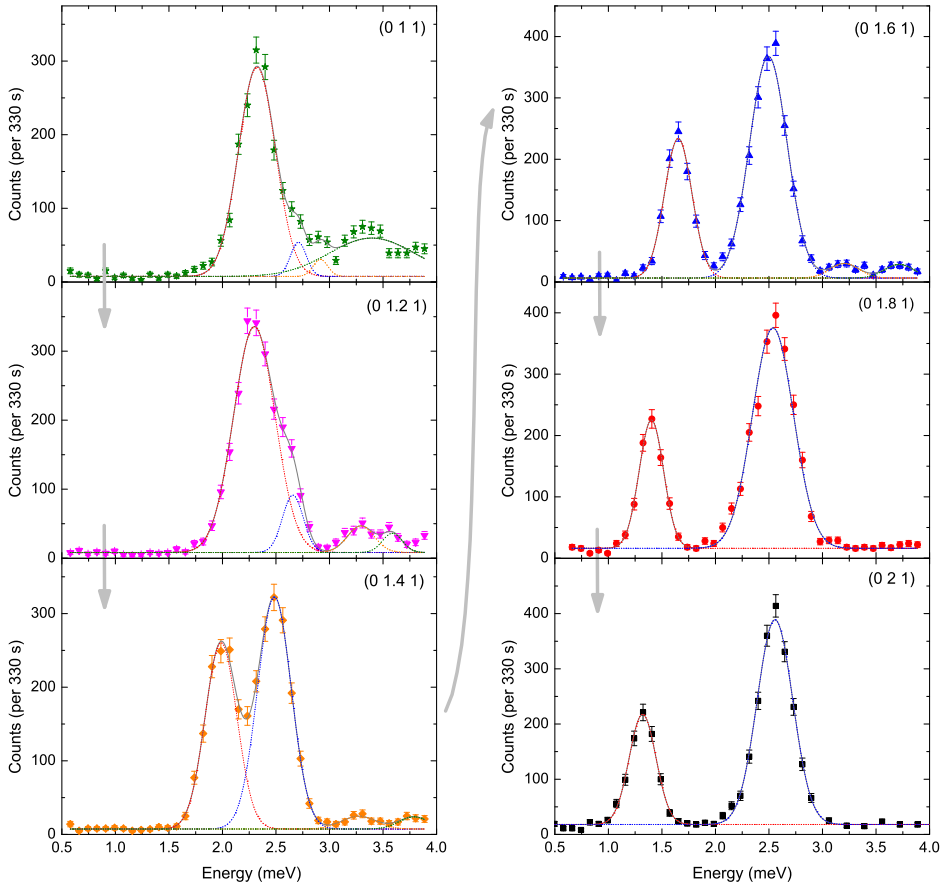

Figure 4.25: Magnetic excitations observed in $Co_3V_2O_8$ across the Brillouin zone in the [0 k 1] direction using the 4F1 spectrometer at the LLB. The energy scans were all performed at 1.3 K. The observed excitations have been fitted with Gaussian functions. The precise energies of the excitations are given in Table 4.3.

Position		Excitation energies (meV)				χ^2	Back-ground
boundary	(0 1 1)	2.32(1)	2.71(4)	2.92(8)	3.40(5)	3.05	7
	(0 1.2 1)	2.30(1)	2.66(2)	3.24(6)	3.57(8)	1.67	8
k	(0 1.4 1)	1.99(1)	2.485(7)	3.27(4)	3.79(5)	0.52	7
direction	(0 1.6 1)	1.65(1)	2.494(4)	3.20(3)	3.72(3)	1.79	6
	(0 1.8 1)	1.40(1)	2.538(5)	-	-	2.09	16
centre	(0 2 1)	1.32(1)	2.556(4)	-	-	1.69	18
centre	(0 2 1)	1.32(1)	2.556(4)	-	-	1.69	18
	(0 2 0.9)	1.393(6)	2.490(4)	3.61(6)	-	3.06	12
l	(0 2 0.8)	1.467(6)	2.357(3)	4.1(4)	-	2.59	9
direction	(0 2 0.7)	1.537(7)	2.168(3)	3.9(2)	-	1.72	7
	(0 2 0.6)	1.66(2)	1.991(7)	4.2(4)	-	0.93	7
boundary	(0 2 0.5)	1.816(6)	1.800(9)	3.9(2)	-	0.76	9

Table 4.3: The energies of the observed magnetic excitations in $Co_3V_2O_8$. The fitted data from which these positions are taken are shown in Figures 4.25 and 4.27. The numbers in brackets are the errors in the last decimal place of the associated numbers.

two at the zone centre. The evolution of the excitations is demonstrated more clearly in Figure 4.26, where the dispersion is also plotted. This plot confirms the conjecture from the inelastic PRISMA data that the dispersion is approximately equal to the observed gap.

Across the Brillouin zone in the [0 2 l] direction up to three excitations are observed (Figure 4.27). The zone boundary in this direction is (0 2 0.5) and the same centre (0 2 1) was used, again studied at 1.3 K. The evolution of the excitations is best observed in a waterfall plot shown in Figure 4.28. The dispersion displayed in the same figure shows how the two most intense excitations converge and overlap at the zone boundary.

Measurements were also taken at 9 K in the incommensurate phase of the sample. Figure 4.29 shows the change in the excitation spectrum across the Brillouin zone in the [0 2.5 l] and [0 k 1] directions from the incommensurate zone centre (0 2.5 1). It can be seen that the excitations, if present, are hidden within the quasi-elastic scattering

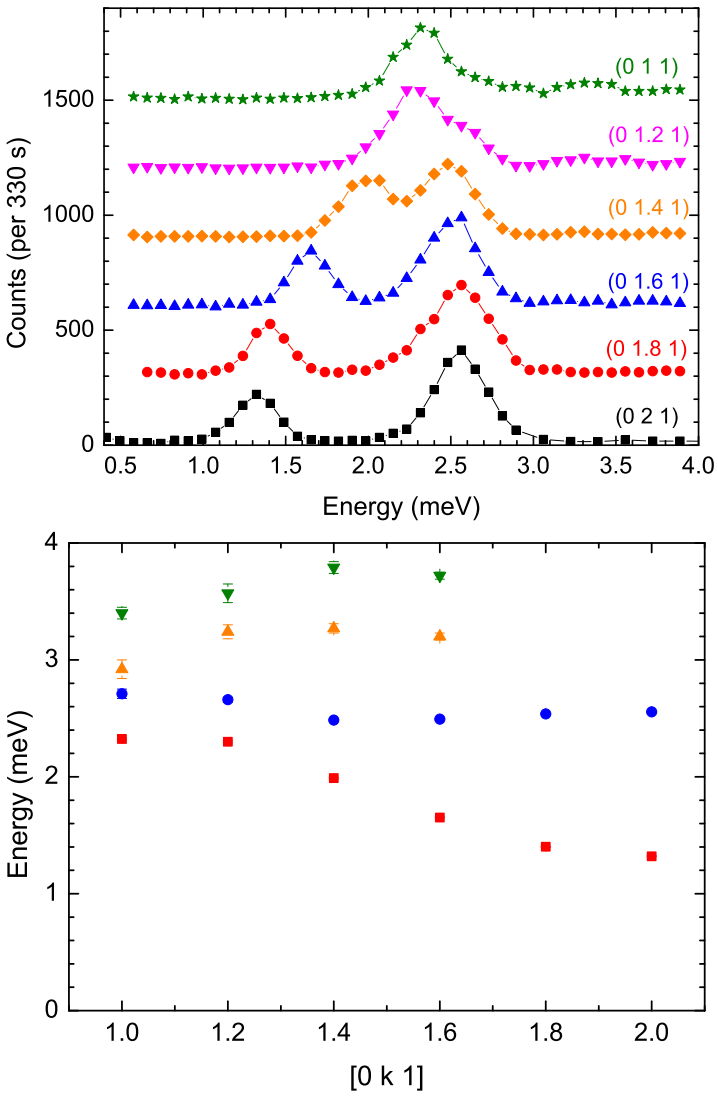

Figure 4.26: Left: Magnetic excitations observed in $Co_3V_2O_8$ across the Brillouin zone in the [0 k 1] direction using the 4F1 spectrometer at the LLB. The energy scans were all performed at 1.3 K, and have been offset by 300 counts for clarity. Right: The dispersion curve shows the variation in the position of the peaks, determined from the fitted functions shown in Figure 4.25. The colours used relate the points to the specific peaks in the fits shown in Figure 4.25

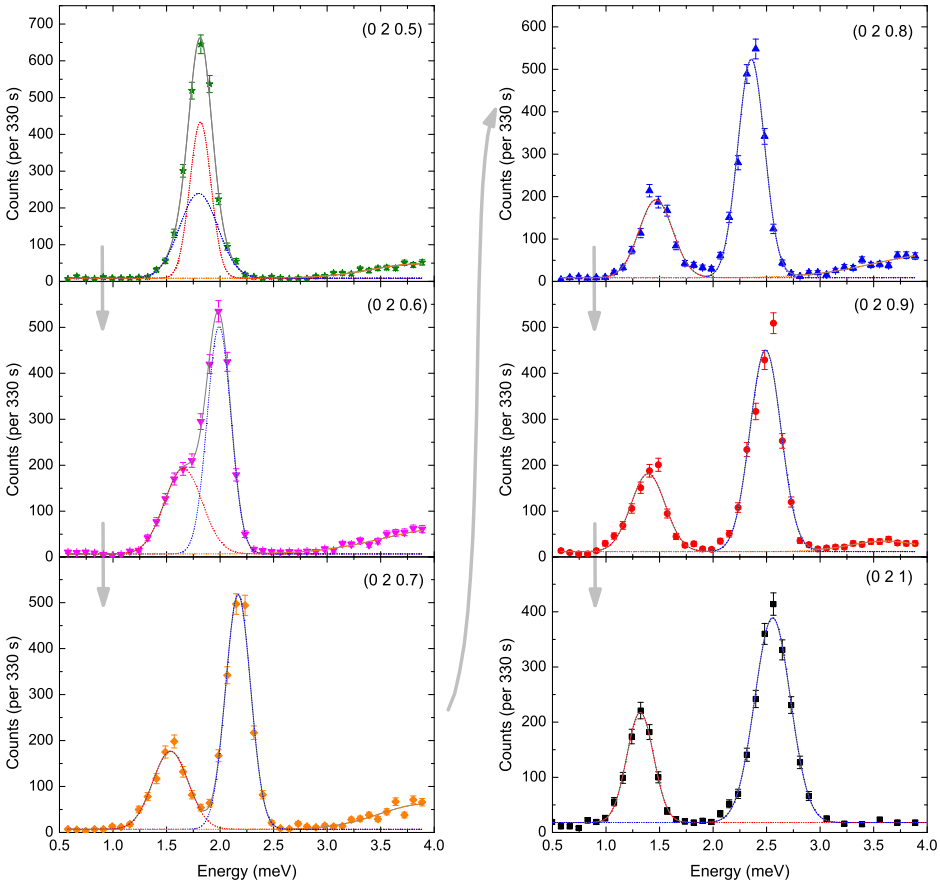

Figure 4.27: Magnetic excitations observed in $Co_3V_2O_8$ across the Brillouin zone in the [0 2 l] direction using the 4F1 spectrometer at the LLB. The energy scans were all performed at 1.3 K. The observed excitations have been fitted with Gaussian functions. The precise energies of the excitations are given in Table 4.3.

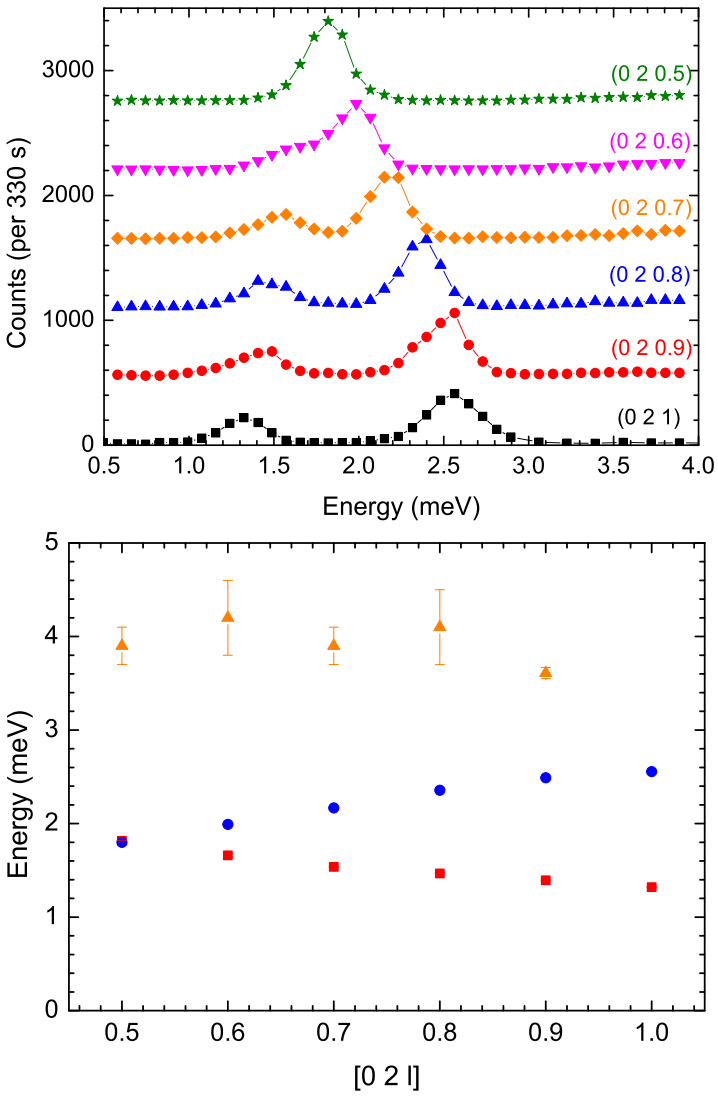

Figure 4.28: Left: Magnetic excitations observed in $Co_3V_2O_8$ across the Brillouin zone in the [0 2 l] direction using the 4F1 spectrometer at the LLB. The energy scans were all performed at 1.3 K, and have been offset by 550 counts for clarity. Right: The dispersion curve shows the variation in the position of the peaks as determined by the fits shown in Figure 4.27. The colours used relate the points to the specific peaks in the fits shown in Figure 4.27

that increases with temperature. The quasi-elastic contribution is consistent across the zone.

As there are 12 Co atoms in the unit cell, each arranged in distorted octahedra of O atoms, it was considered highly possible that further excitation branches existed at higher energies than had been previously probed. The Mari chopper spectrometer was employed to investigate powder $Co_3V_2O_8$ at energies up to 150 meV. An Orange Cryostat was used to reach down to a temperature of 1.4 K. Figure 4.30 shows the spectrum observed below 100 meV at 1.4 K. Phonons can be seen at higher values of $\mathbf{Q}$, and at least two magnetic excitations at low values of $\mathbf{Q}$. These magnetic excitations become more apparent when a cut is taken in energy transfer at constant $\mathbf{Q}$. Figure 4.31 shows such cuts summed over a $\mathbf{Q}$ range of 2.5 to 3.5 $Å^{-1}$ at 15, 7.8 and 1.4 K. These cuts clearly show more excitations than can be seen when the whole spectrum is displayed. There are at least five definable excitations centred at approximately 19, 30, 37, 50 and 68 meV. These excitations become more distinct as the temperature decreases.

In an octahedral configuration including spin-orbit coupling, the twelve-fold degenerate ground state of Co^{2+} is lifted, giving rise to splitting of the energy levels into a doublet, a quartet and a sextet (see section 7.14 of reference [80]). The quartet lies at an estimated 33.1 meV above the doublet, and the sextet sits a further 55.2 meV above the quartet. These energy levels do not easily compare with the excitations energies observed. The estimation is however, not including the effect of the complex distortions of the Co-O octahedra, or the fact that there are two entirely different Co sites in this material, each with different distortions to their octahedra. Distortions would split the quartet and sextet, and produce a number of Kramers doublets. Using all inelastic data, a theorist may propose a model for the interaction routes and strengths within the $Co_3V_2O_8$ structure. Considering the complexity of the model required, this is a procedure beyond the scope of this experimentally based thesis.

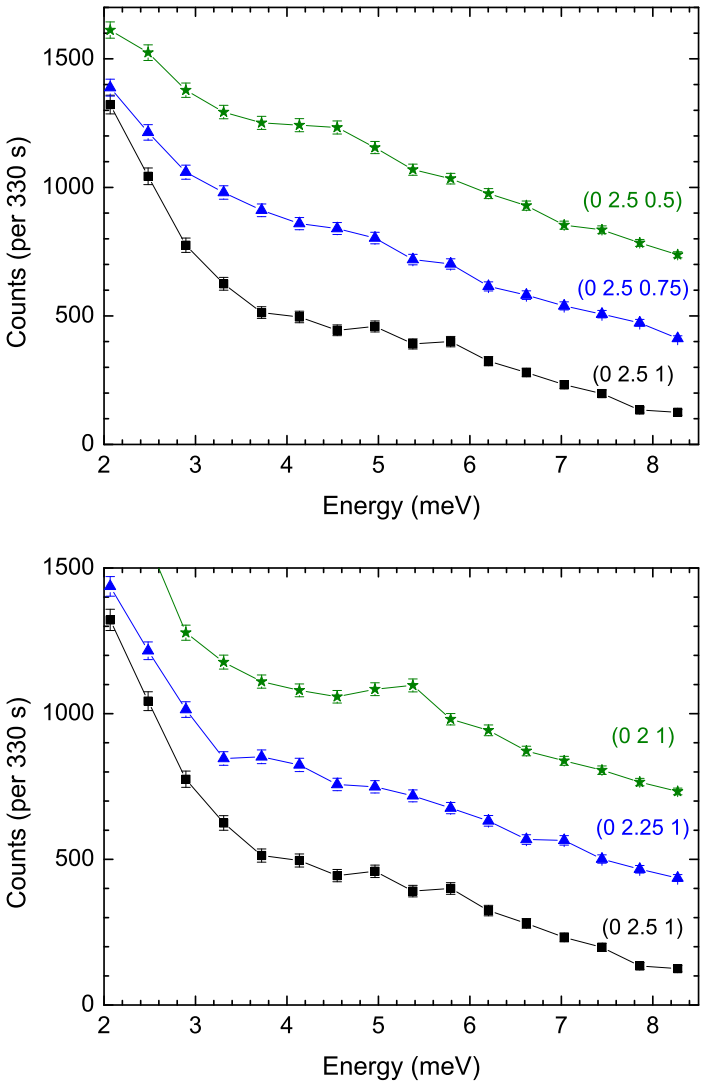

Figure 4.29: Magnetic excitations observed in $Co_3V_2O_8$ across the Brillouin zone from the incommensurate zone centre (0 2.5 1), in the [0 k 1] (left) and [0 2.5 l] (right) directions. The energy scans were all performed at 9 K, and the upper plots have each been offset by +300 counts for clarity.

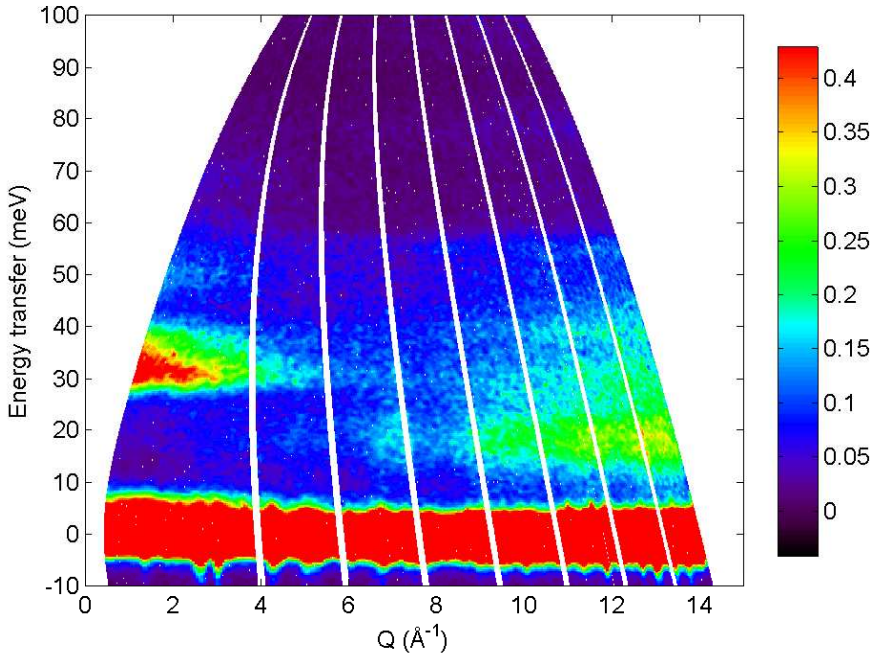

Figure 4.30: Neutron powder spectrometry data of $Co_3V_2O_8$ taken on the Mari instrument at ISIS at 1.4 K. The data show phonon modes at high $\mathbf{Q}$ values and magnetic exctiations at low $\mathbf{Q}$ values. The number of magnetic excitations and the extent to which they can be observed in energy is best seen by the $\mathbf{Q}$ slice shown in Figure 4.31.

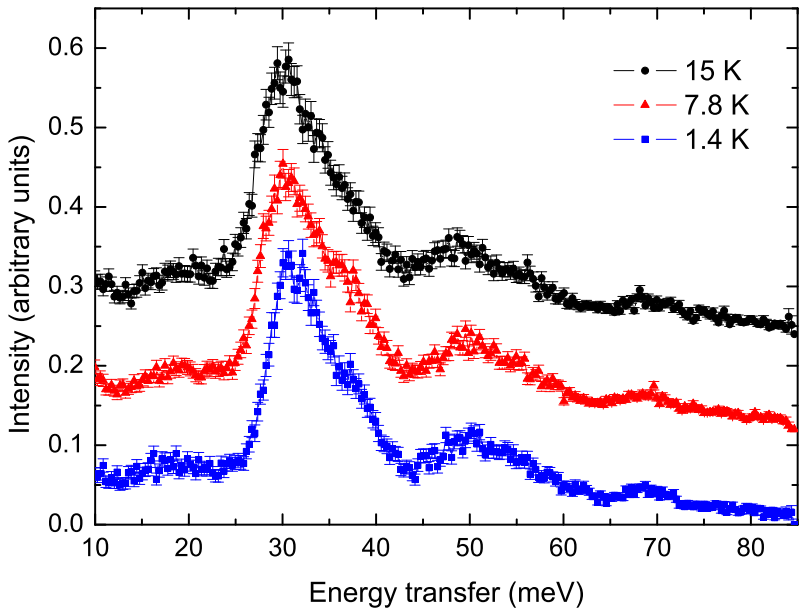

Figure 4.31: Neutron powder spectrometry data of $Co_3V_2O_8$ taken on the Mari instrument at ISIS. The data is the average intensity from a slice taken between 2.5 and 3.5 $Å^{-1}$ in $\mathbf{Q}$ from the data shown in Figure 4.30.

4.6 Summary

All of the data gathered here combine to show the complexity of this system. Using magnetisation and specific heat measurements, $Co_3V_2O_8$ has been shown to have a detailed magnetic field vs. temperature phase diagram with at least four distinct magnetic phases. The two most distinct phase transition temperatures are at 11 and 6 K. Two further transitions are observed at 8.7 and 6.7 K. Susceptibility measurements show the sample to be highly anisotropic. There is a factor of almost 100 between the easy a-axis and the hard b-axis.

Powder neutron diffraction studies have been performed in zero and applied magnetic fields of up to 80 kOe. The magnetic structures have been refined using the FullProf program. The system has two main phases below 11 K: a spin density wave structure with $\mathbf{k} = (0,\ \delta,\ 0)$, where δ varies around $\frac{1}{2}$ above 6 K and a commensurate $\mathbf{k} = 0$ ferromagnetic structure below. The magnetic moment magnitudes of the two Co sites were found to differ by a factor of almost 3. In an applied field, the reduced moment magnitude of the cross-tie site is found to increase to the expected saturation value. During this increase, a re-orientation of all of the Co moments is also observed. These results indicate that the application of a magnetic field relieves the frustration on the cross-tie site and that the two Co sites have different anisotropies.

Single crystal neutron diffraction has shown that the phase diagram is more complex than initially suspected. A narrow region between 5.8 and 6.1 K in zero applied field was found to have intensities at positions forbidden by c-centring symmetry restrictions. These peaks were found to be magnetic in origin and through Rietveld refinement the magnetic structure was determined. The data was best fit with a combination of two structures with $\mathbf{k} = (0,\ \frac{1}{3},\ 0)$ and $(0,\ 1,\ 0)$. From data collected in zero field, the magnetic structures proposed by the refinement of powder diffraction data were confirmed. Throughout these experiments, no distortion to the lattice was observed. If the structural distortion suggested by Bellido *et al.* [43] is to be investigated, a much higher resolution experiment is needed.

In an applied field, a further magnetic phase was also discovered. It again possessed c-centring symmetry breaking peaks, but with much stronger intensity and with none of the satellite peaks ($\delta = \frac{1}{3}$) observed in the other symmetry breaking phase.

Multiple magnetic excitations have been observed using inelastic neutron scattering measurements on powder and single crystals. Measurements from the PRISMA instrument show at least two distinct branches at around 2 meV. Better resolved measurements using the triple-axis spectrometer 4F1 showed there to be at least four branches below 5 meV. Measurements at higher energies using the Mari instrument showed a further collection of at least five branches between 10 meV and 68 meV in energy transfer. This data could provide a theorist with the experimental information required to produce a model for the interaction routes and strengths in $Co_3V_2O_8$.

Chapter 5

Magnetic properties of $Ni_3V_2O_8$

5.1 Single crystals

Powder samples of $Ni_3V_2O_8$ were manufactured using the procedure described in Section 3.1.1. The purity of the powder was found to be excellent; no extra or missing Bragg peaks were observed from in-house X-ray diffraction patterns. An example pattern is shown in Figure 5.1.

Single crystals were then prepared using the technique described previously (Section 3.1.2). Multiple crystals were grown, each using the previous crystal as a seed. The best crystals were produced with an initial fast scan at 15mm/hour, and then a much slower growth at 0.5mm/hour. This approach produced a final crystal of very high quality with a mass of approximately 6 g. It was found to have a mosaic spread of 0.8° over its entire 2 cm^3 volume. Using the EDX technique on an SEM, no peaks in the data were found to correspond to impurities within an accuracy of approximately 1 atomic %. Within this accuracy, the relative ratios of the heavier atoms, Ni and V were correct at 3:2. The crystals produced are identical in appearance to the $Co_3V_2O_8$ crystal shown in Figure 4.2. The crystals were aligned using an X-ray Laue camera. Again, the images produced are indistinguishable to those from the $Co_3V_2O_8$ crystal as the structures are identical, an example of which is shown in Figure 4.3. Once aligned along the three

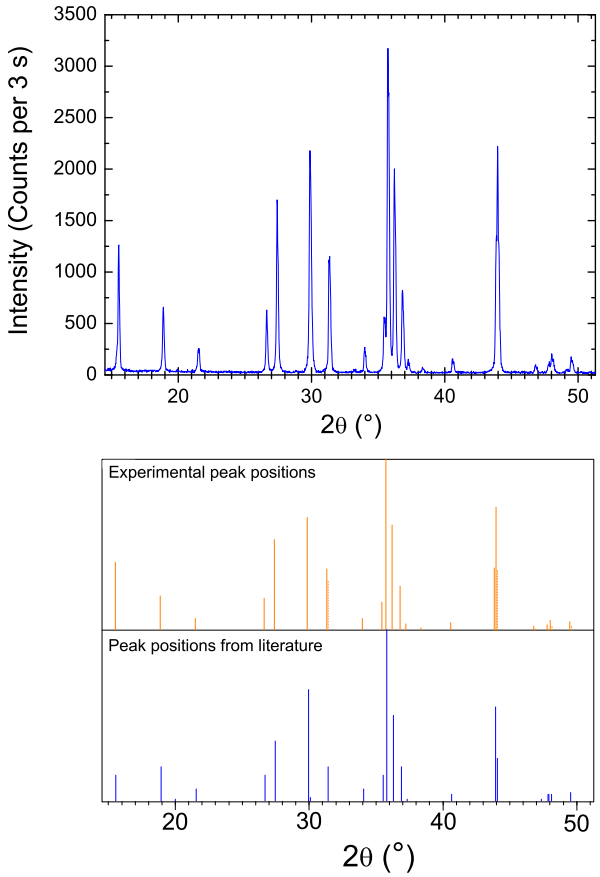

Figure 5.1: X-ray diffraction pattern of $Ni_3V_2O_8$ (upper panel) and the fitted peak positions compared to published peak positions from reference [75] (lower panel). A Cu Kα source was used to produce an X-ray wavelength of 1.5418 Å. The dotted lines mark the Kα_2 experimental peak positions.

crystallographic axes to within an accuracy of 3°, the crystal was cut using a low speed diamond wheel saw and laboratory measurements were taken.

5.2 Magnetic phase diagram

Through magnetometry (VSM and SQUID) and specific heat measurements, the magnetic field vs. temperature phase diagram for $Ni_3V_2O_8$ was produced, and is shown in Figure 5.2. The precise positions of phase transitions were chosen using consistent means throughout. For example, if the transition was observed as a hysteresis in a magnetisation measurement taken as a function of applied field, then the transition point was taken as the average of the two peaks in the derivative formed by the field sweep up and down. The samples were investigated with fields applied along each of the three main crystallographic directions. The phase transitions were tracked in the temperature interval between 1.4 and 12 K in a magnetic field range $\pm$120 kOe.

The phase diagram demonstrates the complexity of this material; the boundaries indicate that there are five different phases present, as found by Lawes *et al.* [27]. In zero field the sample is paramagnetic down to 9.1 K, it then enters the high temperature incommensurate phase (HTI). At 6 K, the material enters the low temperature incommensurate phase (LTI). At 4 K the sample becomes commensurate, this phase is labelled C. At 2 K another transition is observed and the sample is still commensurate, this phase is labelled C'. The structure of these phases will be demonstrated later by neutron diffraction data. For consistency, the notation of the phases follows that of Lawes *et al.* [27].

The phase diagram produced here agrees well with the first published form [27]. This first form however only extended to applied fields of 80 kOe. The ability to extend the diagram to 120 kOe allows for more detail to be observed. To support the phase diagram, a complete range of characteristic magnetisation and susceptibility curves of $Ni_3V_2O_8$ is shown in Figure 5.3. Magnetisation measurements have also been used to measure the Weiss temperature which was found to be -29.6$\pm$0.4 K, as shown in Fig-

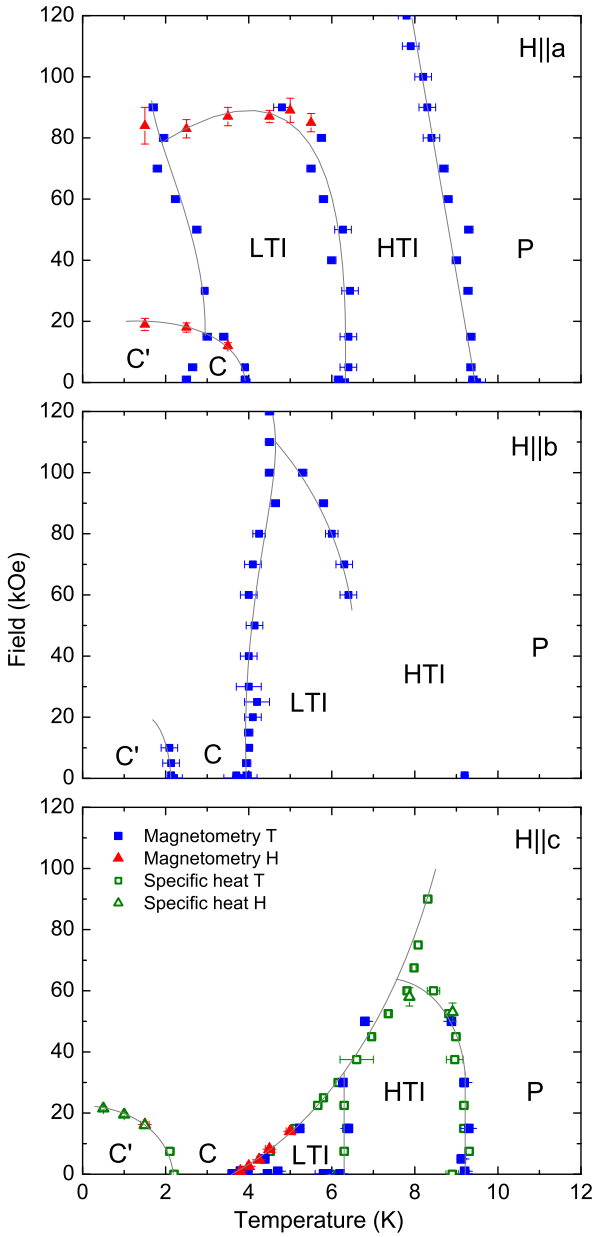

Figure 5.2: The magnetic field vs. temperature phase diagram for $Ni_3V_2O_8$. The data were gathered from magnetisation and specific heat measurements of single crystal samples, both field ($\mathbf{H}$) and temperature (T) dependence measurements were taken. Curves are drawn as guides to the eye only.

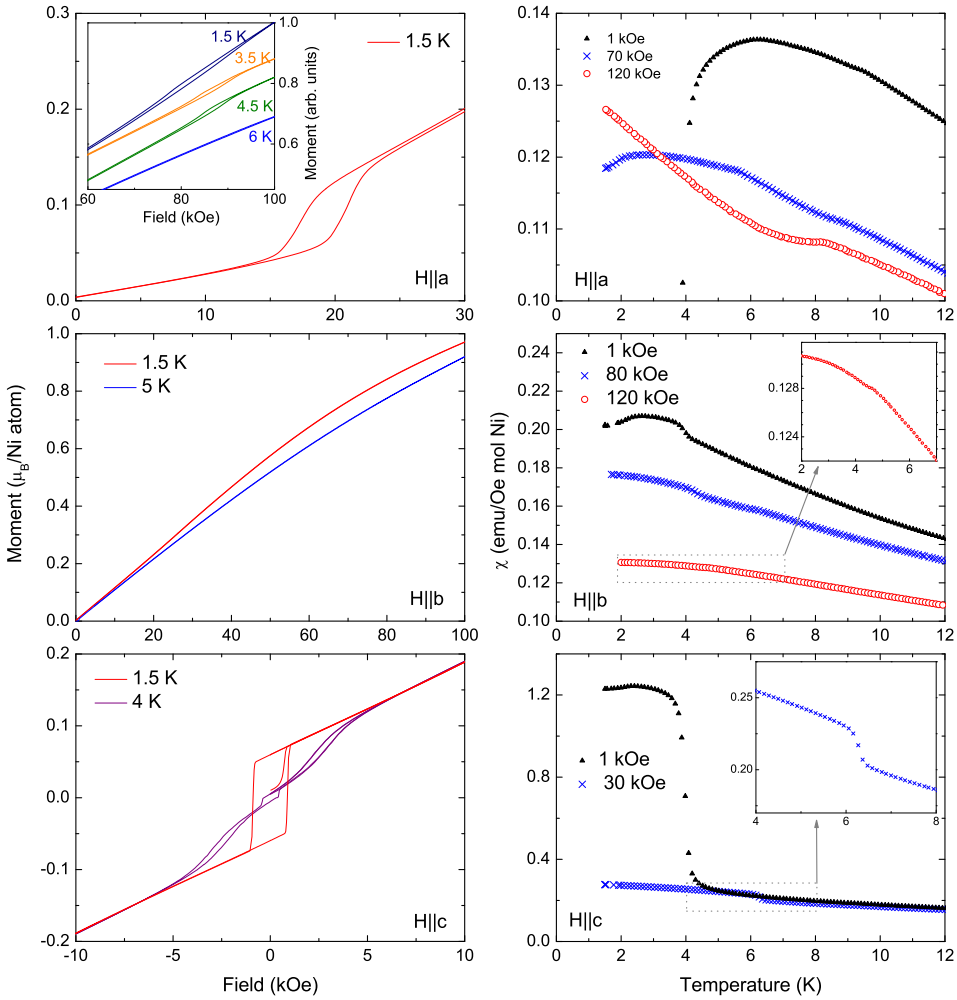

Figure 5.3: Left panels: Characteristic field dependent magnetisation curves for each of the three main crystallographic directions of $Ni_3V_2O_8$. For $\mathbf{H} \parallel a$, the top figure shows there to be no hysteresis about zero applied field (within the 50 Oe field resolution of our measurements). There is a hysteresis centred around 18 kOe at 1.5 K. The inset shows that at much higher fields another hysteresis is observed. The magnetisation curves for $\mathbf{H} \parallel b$ are quite featureless, no phase transitions are crossed when traversing the phase diagram in this direction. For $\mathbf{H} \parallel c$, a significant hysteresis is observed about zero applied field at 1.5 K. By 4 K, this has almost gone but another hysteresis centred around 2.5 kOe is clearly visible. Right panels: Characteristic susceptibility curves performed with various applied fields. The figures show that the c-axis is the easy axis, and the a-axis is the hard axis of the sample. The insets show an expanded view of the higher field data to more clearly show the transitions. The observed phase transitions were used to build the magnetic field vs. temperature phase diagram shown in Figure 5.2.

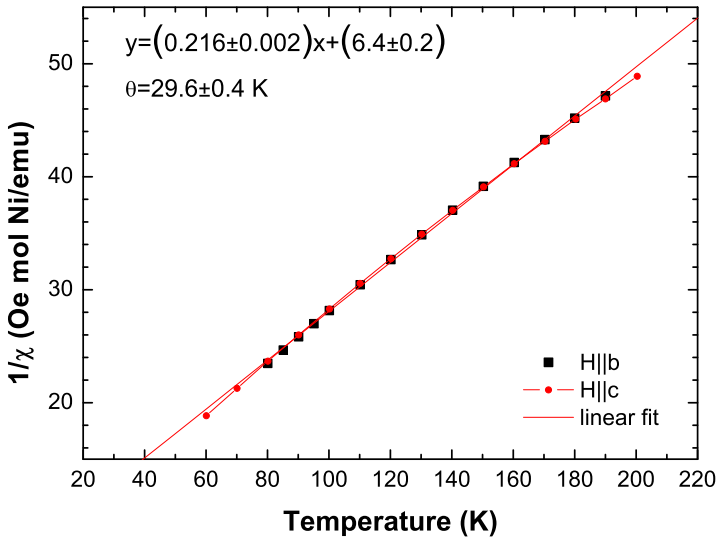

Figure 5.4: The Weiss temperature θ was determined for $Ni_3V_2O_8$ using SQUID magnetometry measurements. A linear fit is applied at temperatures above the magnetic transitions and the x-intercept is found. For fields applied parallel to the b and c-axes the average value was found to be -29.6$\pm$0.4 K.

ure 5.4. As can be seen from this figure, the results are consistent for fields applied in different directions and a linear fit is a good approximation over the temperature range of 60 to 200 K. The effective moment of the sample was calculated as 3.5$\pm$0.1 μ_B/Ni, compared to 3.3 μ_B/Ni as found by Rogado *et al.* [26]. These values are of the same order as the value usually found for Ni^{2+} at 3.12 μ_B/Ni [3]. The saturation magnetisation and field could not be determined with the available magnetic fields. The highest magnetic moment observed was 1.2 μ_B in a field of 120 kOe applied along the c-axis.

For $\mathbf{H} \parallel a$ (see Figure 5.3 upper panel) the $\mathbf{M}(\mathbf{H})$ curves collected between 1.5 and 6 K show slight hysteresis at approximately 80 kOe, but only in the temperature range of the LTI phase [35]. This is evidence for the abrupt closing of this phase, making the cut off very square. In addition to the closing of the LTI phase for $\mathbf{H} \parallel a$, the phase diagram here also contains a further phase boundary at around 20 kOe at the lowest

temperature. This transition is evident from the large hysteresis observed in the $\mathbf{M}(\mathbf{H})$ curves measured at 1.5 and 2 K. The VSM $\mathbf{M}(T)$ measurements for $\mathbf{H} \parallel a$ show features corresponding to all four phase transitions.

For fields applied along the hard b-axis, the $\mathbf{M}(\mathbf{H})$ measurements are featureless, and the $\mathbf{M}(T)$ curves are only sensitive to the two lower temperature transitions (Figure 5.3 central panel). More sensitive SQUID magnetisation measurements contribute to the phase diagram for the paramagnetic to HTI transition in very low fields. The SQUID measurements could still not detect the HTI to LTI transition in low fields. This transition was only observed at fields of 60 kOe and above using the VSM, the SQUID has a field limit of 50 kOe.

For fields applied along the easy c-axis (Figure 5.3 lower panel), the transition from the C' to the C phase is observed as a broad peak in the derivative of the 1.5 K $\mathbf{M}(\mathbf{H})$ data. A much more distinct hysteresis is also observed at this temperature. This gives way around the temperature of the transition to the LTI phase (4 K), where it will later be seen that the magnetic moments are partially disordered. At these temperatures a new hysteresis appears, offset in field at around 2.5 kOe. This hysteresis corresponds to the first order transition from the LTI to the C phase. The $\mathbf{M}(T)$ curves show features corresponding to the higher temperature phase transitions. The change in magnetic structure over the transitions will be discussed in the next section with the neutron diffraction data.

To produce the phase diagram, measurements of the specific heat of $Ni_3V_2O_8$ with a magnetic field applied parallel to the c-axis were also considered. Only the easy axis was investigated with specific heat measurements as a field applied along any other direction would cause the sample to twist on the sample platform. The results from such an experiment would be unreliable as the orientation of the sample would be unknown and damage could be done to the delicate supports of the platform. Figure 5.5 shows the data for applied fields of 0, 45 and 90 kOe parallel to the easy axis. Four transitions can clearly be seen in the zero applied field data. The most intense is the transition

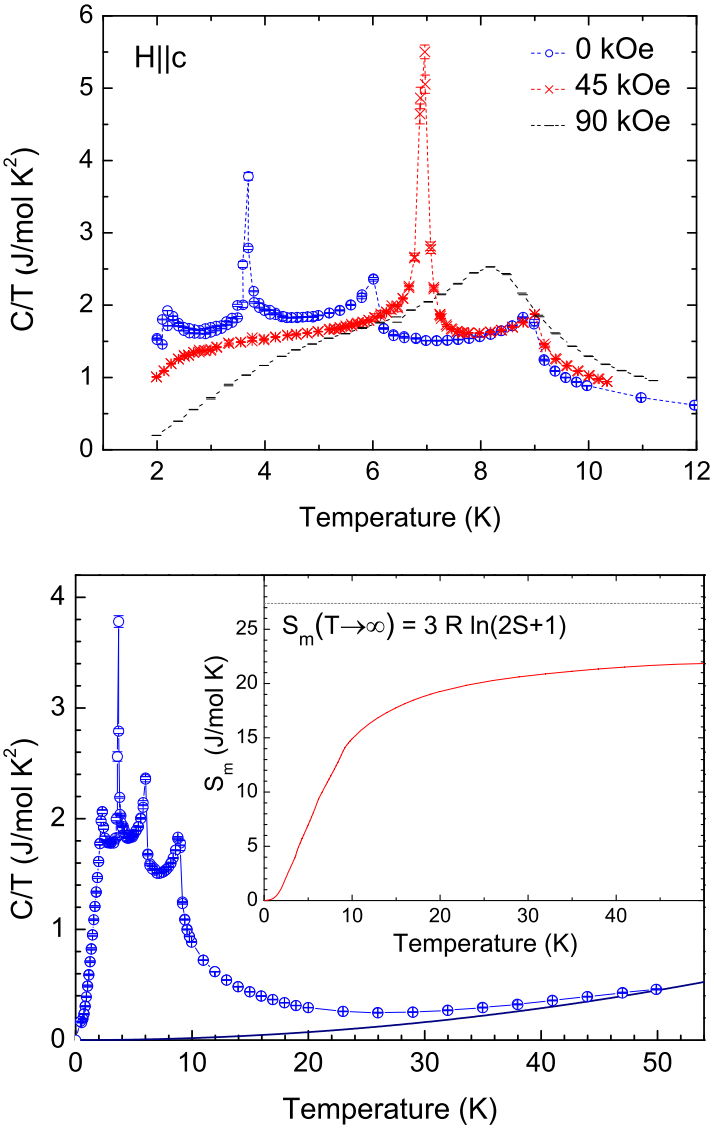

Figure 5.5: Upper panel: The specific heat in $Ni_3V_2O_8$ normalised to temperature for an applied field parallel to the easy c-axis. Measurements were taken in applied fields of 0, 45 and 90 kOe. The most intense peak observed at 4.8 K in the 0 kOe data moves to higher temperatures with higher applied fields. By 90 kOe it has spread and forms a much broader peak at 8 K. Lower panel: Specific heat in zero applied field extended up to 50 K with an estimated T^3 phonon contribution (solid line). The magnitude of this contribution corresponds to a Debye temperature of approximately 250 K. For the inset, this contribution has been subtracted and the remaining signal integrated to calculate the molar magnetic entropy S_m. The asymptotic value for $\mathbf{S}$=1 is shown by the dotted line.

from the LTI to the C phase. It is this transition which moves to higher temperatures with higher applied fields, and remains the most intense and distinct. In an applied field of 90 kOe, this transition is now at 8 K and appears as a much broader peak.

In the lower panel of Figure 5.5, the specific heat in zero applied field is plotted up to 50 K. The T^3 phonon contribution has been estimated at $0.00018T^3$ and is shown as a solid line. The magnitude of this contribution corresponds to a Debye temperature of approximately 250 K. This contribution was then subtracted from the measured values, and the magnetic molar entropy S_m was calculated numerically. The asymptotic value, $S_m(T \rightarrow \infty)$ for $\mathbf{S}$=1 is also shown on the plot, the standard equation is multiplied by 3 as there are 3 Ni atoms per formula unit of the compound. At 10 K, just above the highest transition temperature, approximately 54% of the entropy is recovered. By 50 K, the recovered entropy is approximately 80%. This deficit could be explained by an inaccurate estimate of the T^3 contribution, or by the specific heat measurements not being accurate enough to capture the entire intensity of the peaks.

5.3 Magnetic structure from powder measurements

Neutron powder diffraction measurements have been performed on the GEM diffractometer at the ISIS facility. Around 6 g of powder were packed into a vanadium can for the experiment, and loaded into an Oxford Instruments cryostat. Measurements were taken at 1.8 and 2 K, then at half degree intervals until 11 K. Figure 5.6 shows the interpolated data below 11 K. The counting time for each run was approximately 1 hour, counting for 160 μAh.

As discussed in Section 1.3.2, similar measurements have been performed previously. The magnetic refinements have been published in zero field for powder measurements of the C', HTI and LTI phases [27]. For an applied field with a single crystal, they have been published in the C, HTI and LTI phases [25]. Shown here is a new analysis of powder neutron diffraction measurements and the resulting magnetic structures. Rietveld analysis has been attempted in the HTI, LTI, C and C' phases (see Figure 5.2 to

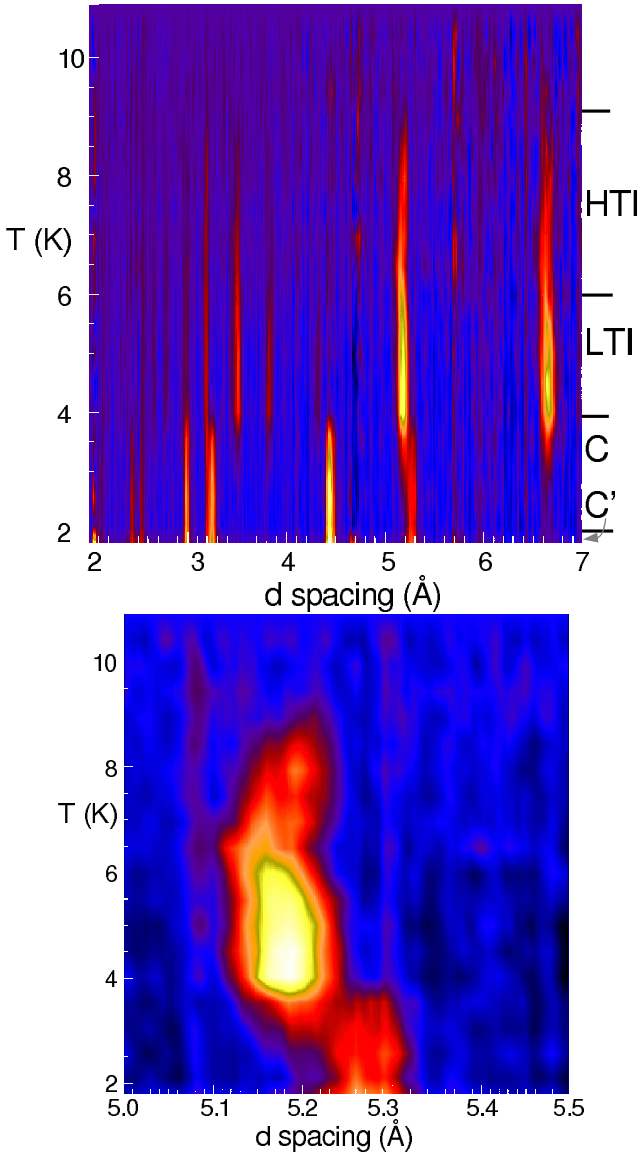

Figure 5.6: Temperature dependence of neutron powder diffraction data of $Ni_3V_2O_8$ taken on the GEM instrument. Line scans were taken at 0.5 K temperature intervals and interpolated between. The transition temperatures are 9.1, 6, 4 and 2 K. The lower panel shows a small scale in d-spacing to demonstrate the phase transitions more clearly. The colour scale ranges from dark blue representing the lowest scattered intensity, through red, yellow to white for the highest intensity. The highest intensity observed at 4.45 Å has 180 counts in 1 hour, the background corresponds to approximately 35 counts and the peak at 5.26 Å at the lowest temperature has 45 counts. The different magnetic phases are indicated by the text on the right of the upper figure.

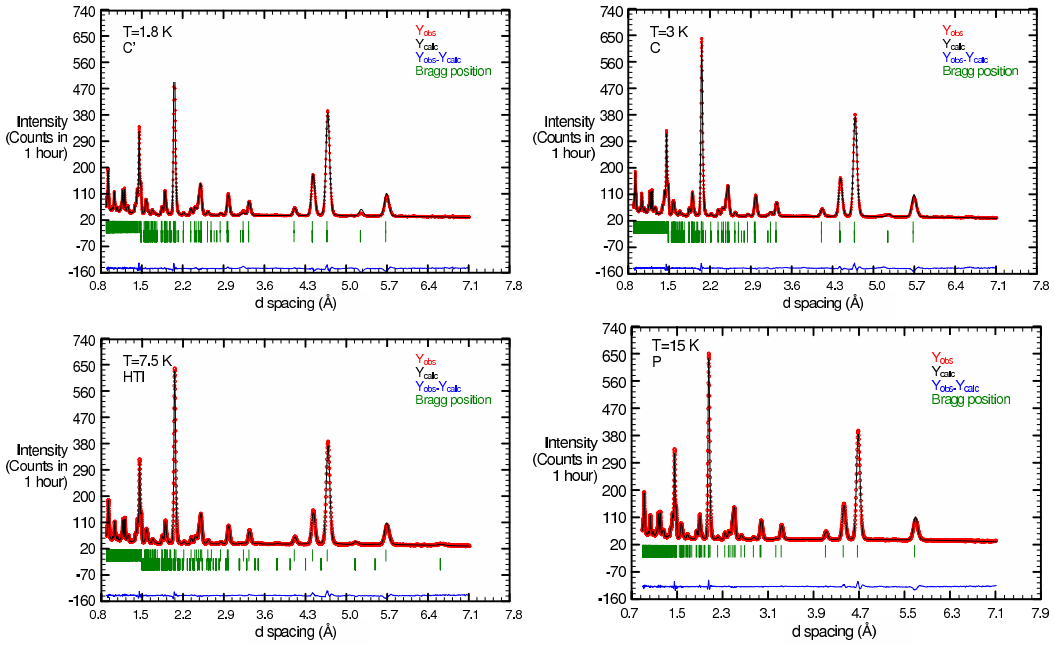

Figure 5.7: Refinement of neutron powder diffraction data of $Ni_3V_2O_8$ performed using FullProf. Characteristic temperatures from the paramagnetic (15 K), HTI (7.5 K), C (3 K) and C' (1.8 K) phases are shown. The upper line of green dashes shows the nuclear Bragg peak positions, the lower line of dashes shows the magnetic Bragg peak positions.

identify these phases). The refined fits to the data from representative temperatures in each of these phases, and from the nuclear only fit in the paramagnetic phase are shown in Figure 5.7. The $\mathrm{R_{Nuc}}$ and $\mathrm{R_{Mag}}$ values (nuclear and magnetic R factors) for each of the fits are given in Table 5.2, along with the values of the most important refined parameters.

It was suggested by Kenzelmann *et al.* [25] that the structure in the commensurate C' phase was formed by a mixture of irreducible representations $\Gamma 1$ and $\Gamma 3$ on both sites ($\Gamma 1$ and $\Gamma 7$ in the notation used in reference [25]). The representations are given in Table 5.1. However, with the high quality data gathered using GEM, this symmetry configuration was not found to give the best fit to the data. In fact, two entirely differ-

	Atoms					
Irreps.	Ni(c-1)	Ni(c-2)	Ni(s-1)	Ni(s-2)	Ni(s-3)	Ni(s-4)
Γ_1	(u_1,0,0)	(-u_1,0,0)	(0,v_2,0)	(0,-v_2,0)	(0,v_2,0)	(0,-v_2,0)
Γ_2	-	-	(0,v_2,0)	(0,-v_2,0)	(0,-v_2,0)	(0,v_2,0)
Γ_3	(0,v_1,w_1)	(0,-v_1,w_1)	(u_2,0,w_2)	(-u_2,0,w_2)	(u_2,0,w_2)	(-u_2,0,w_2)
Γ_4	-	-	(u_2,0,w_2)	(-u_2,0,w_2)	(-u_2,0,-w_2)	(u_2,0,-w_2)
Γ_5	(0,v_1,w_1)	(0,v_1,-w_1)	(0,v_2,0)	(0,v_2,0)	(0,v_2,0)	(0,v_2,0)
Γ_6	-	-	(0,v_2,0)	(0,v_2,0)	(0,-v_2,0)	(0,-v_2,0)
Γ_7	(u_1,0,0)	(u_1,0,0)	(u_2,0,w_2)	(u_2,0,-w_2)	(u_2,0,w_2)	(u_2,0,-w_2)
Γ_8	-	-	(u_2,0,w_2)	(u_2,0,-w_2)	(-u_2,0,-w_2)	(-u_2,0,w_2)

Table 5.1: Basis vectors for symmetry related Ni ions of the cross-tie (c) and spine (s) sites belonging to irreducible representations of the little group G_k, Cmca with $\mathbf{k} = (0, 0, 0)$. Labelling of the irreducible representations follow Kovalev's notation [77]. The absence of modes for irreducible representations not appearing in the decomposition of the magnetic representation is indicated by the "-" sign.

ent configurations were found to give very good fits. One combination was with $\Gamma7$ on both Ni sites, and the other uses $\Gamma7$ for the cross-tie site and $\Gamma3$ for the spine site. The values of the most important refined parameters are given in Table 5.2.

Considering that the expected magnetic moment of Ni^{2+} in an octahedral configuration is around 3.12 μ_B [3], the magnetic structure from these two options are both reasonable. The $\Gamma7$ and $\Gamma3$ configuration gives a much more significant moment value on the cross-tie than the $\Gamma3$ structure. It fits with data from the incommensurate phases to have a larger moment on this site and so the $\Gamma7$ and $\Gamma3$ configuration is considered more favourable. This structure is predominantly collinear along the a-axis, but with canting along the c-axis on one site. The non-canted cross-tie site has approximately 45% of the magnetic moment found on the canted spine site. The spine sites are antiferromagnetic whereas the cross-tie sites align ferromagnetically. The $\Gamma3$ structure is similar, but more of the overall magnetic moment is found on the spine site; the cross-tie site has only 36% of the moment on the other site. The canting in this structure still exists only on the antiferromagnetic spine sites. The ferromagnetic cross-tie moments align along the c-axis. Diagrams of the two possible structures are shown in Figure 5.8.

		P	HTI	C	C	C'	C'
Temperature (K)		15	7.5	3	3	1.8	1.8
Symmetry		-	$\Gamma1$ & $\Gamma1$	$\Gamma7$ & $\Gamma3$	$\Gamma3$ & $\Gamma3$	$\Gamma7$ & $\Gamma3$	$\Gamma3$ & $\Gamma3$
R_{Nuc} (%) bank 3		1.90	2.16	1.93	2.05	1.98	1.69
R_{Nuc} (%) bank 4		1.83	2.35	1.81	1.81	1.72	1.73
R_{Mag} (%) bank 3		-	26.84	4.88	7.37	6.71	6.49
R_{Mag} (%) bank 4		-	29.50	7.63	6.99	6.72	8.04
Cross-tie site	a	-	0.1*	0.956	0.0*	1.037	0.0*
magnetic	b	-	0.0*	0.0*	0.168	0.0*	0.101
moment (μ_B)	c	-	0.0*	0.0*	0.401	0.0*	0.424
Spine site	a	-	1.835	2.026	2.045	2.223	2.240
magnetic	b	-	0.050	0.0*	0.0*	0.0*	0.0*
moment (μ_B)	c	-	0.474	0.640	0.886	0.654	0.906

Table 5.2: The refined parameters for the paramagnetic (P), HTI, C and C' phases of $Ni_3V_2O_8$. All magnetic peaks were within the range of the two detector banks numbered 3 and 4. Refinements were performed using the FullProf suite of programs. Values marked with '*' were fixed and not refined.

The favoured $\Gamma7$ and $\Gamma3$ structure is not completely unlike that suggested by Lawes *et al.* [27]. The main differences are that the structure proposed here only has canting on one site and is larger, and the other site does not alternate its direction.

It has been suggested that in the C phase, evidence for remnant incommensurate modulation can be seen [27]. However, this was not observed in the GEM experiment and the structure found in the C' phase, was also found to hold for the C phase. A slight change in the magnetic moment magnitude is observed, the numbers are given in Table 5.2.

In the incommensurate phases LTI and HTI, the structure is defined by a propagation vector of (0.275, 0, 0). The symmetry is described by the basis vectors given in Table 5.3. The structure of the HTI phase has been suggested as $\Gamma4$ for both Ni sites [27]. In the LTI phase, the structure is suggested to be a combination of $\Gamma1$ and $\Gamma4$ on both sites. The data collected here, however, do not provide enough magnetic peaks to allow a reliable structure refinement. This is most problematic for the LTI

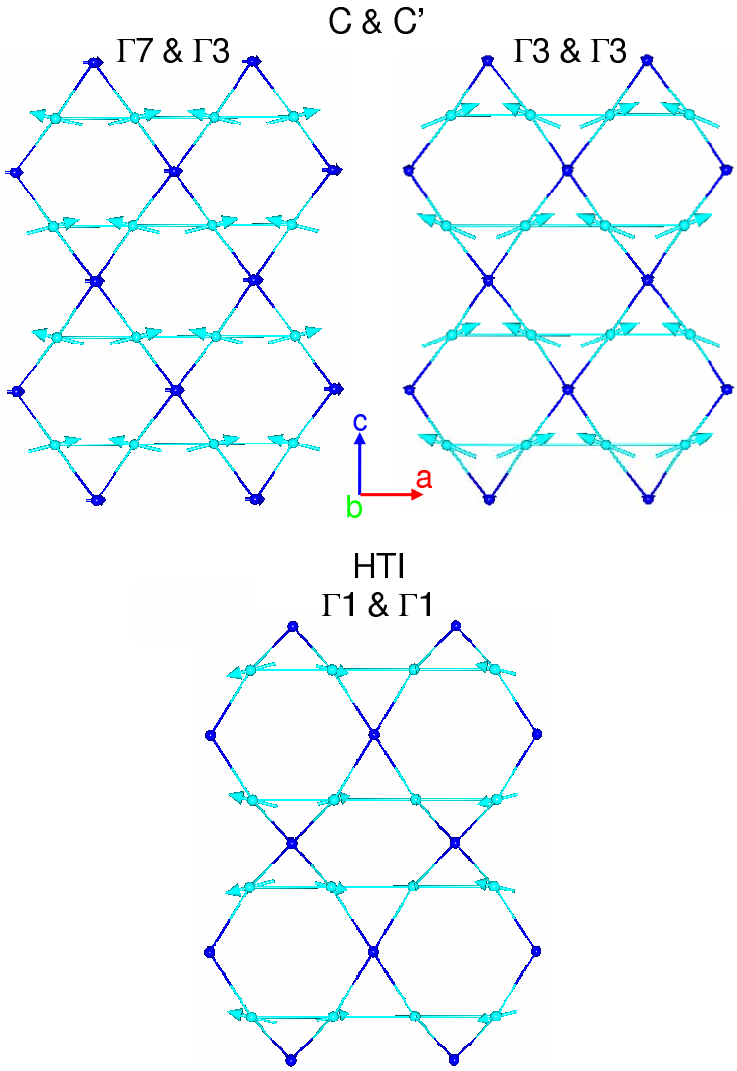

Figure 5.8: The proposed magnetic structures of $Ni_3V_2O_8$ in the C and C' phases, and the HTI phase. The cross-tie Ni sites are shown in dark blue, and the spine sites are shown in light blue. The moment magnitudes on the different sites are to scale.

	Atoms					
Irreps.	Ni(c-1)	Ni(c-2)	Ni(s-1)	Ni(s-2)	Ni(s-3)	Ni(s-4)
Γ_1	(u_1,0,0)	(-u_1,0,0)	(u_2,v_2,w_2)	(u_2,-v_2,-w_2)	(-u_2,-v_2,w_2)	(-u_2,v_2,-w_2)
Γ_2	(u_1,0,0)	(u_1,0,0)	(u_2,v_2,w_2)	(u_2,-v_2,-w_2)	(u_2,v_2,-w_2)	(u_2,-v_2,w_2)
Γ_3	(0,v_1,w_1)	(0,-v_1,w_1)	(u_2,v_2,w_2)	(-u_2,v_2,w_2)	(-u_2,-v_2,w_2)	(u_2,-v_2,w_2)
Γ_4	(0,v_1,w_1)	(0,v_1,-w_1)	(u_2,v_2,w_2)	(-u_2,v_2,w_2)	(u_2,v_2,-w_2)	(-u_2,v_2,-w_2)

Table 5.3: Basis vectors for symmetry related Ni ions of the cross-tie (c) and spine (s) sites belonging to irreducible representations of the little group G_k, Cmca with **k**=(0.275,0,0). Labelling of the irreducible representations follow Kovalev's notation [77].

phase where the suggested structure has a complicated symmetry that would involve a large number of parameters. The structure in this case cannot be fitted to the data.

In the HTI phase, the single representations $\Gamma1$ and $\Gamma4$ separately give reasonably good fits to the data. However, the results are not reliable - particularly in terms of the magnetic moment on the Ni cross-tie site. Different starting parameters and numbers of refinement cycles produce different results and no convergence is ever reached. If the $\Gamma1$ symmetry is used and the magnetic moment is restricted to a small value along the a-axis (the only direction allowed by symmetry for this configuration) then a reasonable fit is achieved, with very reasonable magnetic moment magnitudes. The data and fit from $\Gamma1$ are given in Figure 5.7 and the refined parameters are given in Table 5.2. A sample of the structure is shown in Figure 5.8, although it must be remembered that the reliability of this structure is not absolute. The antiferromagnetic spine site moments are modulated along the a-axis direction and are still canted along c. The negligible magnetic moment on the cross-tie site agrees with the proposed structures from Lawes *et al.* [27] and Kenzelmann *et al.* [25].

5.4 Magnetic excitations

As with the other Kagomé staircase sample $Co_3V_2O_8$, $Ni_3V_2O_8$ was also studied using the PRISMA instrument in both of its configurations. The settings used were the same as those described for $Co_3V_2O_8$ in Section 4.5. Bragg peaks were mapped in each phase and the magnetic excitations were investigated. A crystal approximately 2 cm^3 in volume was used for the experiment. The instrument jaws were tightened, their separations were 27 and 38 mm for the top/bottom and east/west jaws respectively. Figure 5.9 shows the reciprocal space maps in the plane [h k 0] at 20, 7.5, 5 and 1.3 K. As the sample is cooled from the paramagnetic phase into the HTI phase, satellite peaks appear around the [1 k 0] peaks. These satellites increase in intensity as the LTI phase is entered. In the commensurate phases (the C and C' phases produced identical results), the satellites are gone and the intensities of the peaks indexed with integer hkl values are increased by a magnetic contribution. Some twinning of the crystal is evident from the shape and spread of the peaks, but these maps still gave a useful first approximation of the propagation vector found in the LTI and HTI phases at (0.275, 0, 0). They provide clear evidence as to which magnetic Bragg peaks are strongest and most suitable to study.

Investigations into the magnetic excitations were performed along the [h 3 0] direction passing through the magnetic Bragg peak at (1 3 0). At least two excitation branches are clearly seen at T=1.3 K. These are shown in Figure 5.10. The lower energy branch (observed around 1 meV) is much more intense than the upper branch at about 3.5 meV. Background measurements performed at T=20 K have confirmed that both of these branches are of magnetic origin. No excitations were observed in the higher temperature incommensurate phases around the (0.73 3 0) magnetic Bragg peak. However, with the restricted geometry of the PRISMA instrument, this was the only available incommensurate peak. A more versatile instrument was required to look more closely at the higher temperature phase.

The 4F2 triple-axis spectrometer at the LLB was used to investigate the low energy excitations in more detail. The majority of the measurements were performed

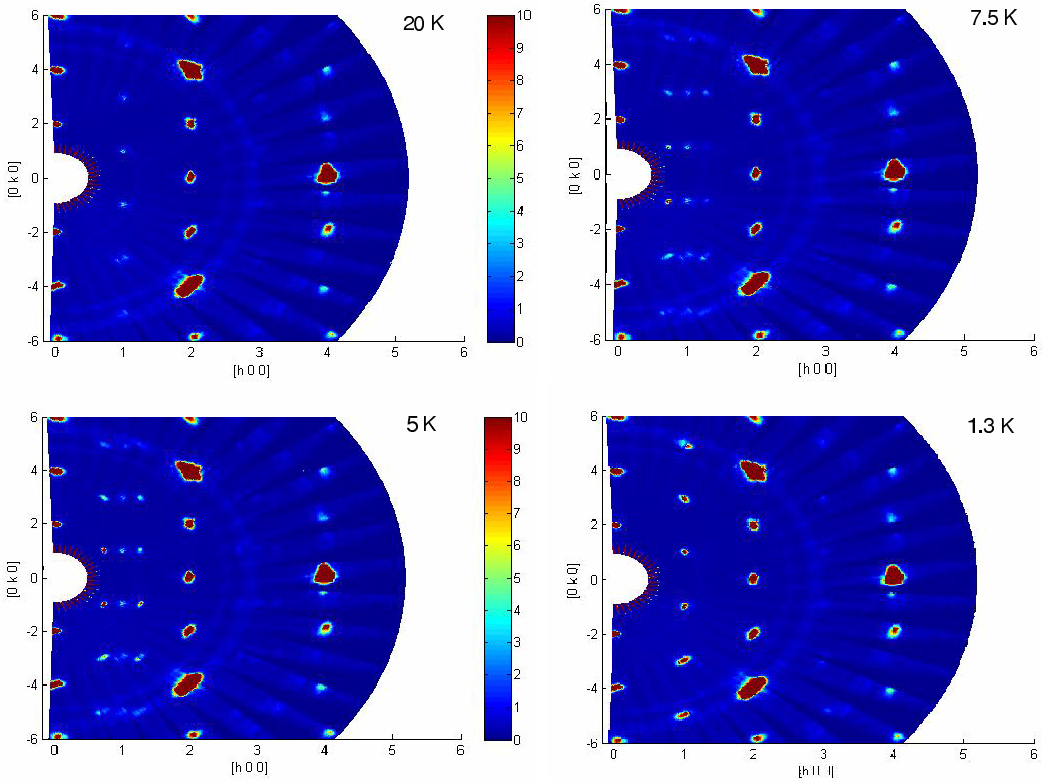

Figure 5.9: Reciprocal space maps of $Ni_3V_2O_8$ in the paramagnetic (20 K), HTI (7.5 K), LTI (5 K), and C' (1.3 K) phases. As the sample is cooled from the paramagnetic phase into the HTI phase, satellite peaks appear around the [1 k 0] peaks. These satellites increase in intensity as the LTI phase is entered. In the commensurate phases, the satellites are gone and all peaks have higher intensities, this is most clear when looking at the [1 k 0] peaks.

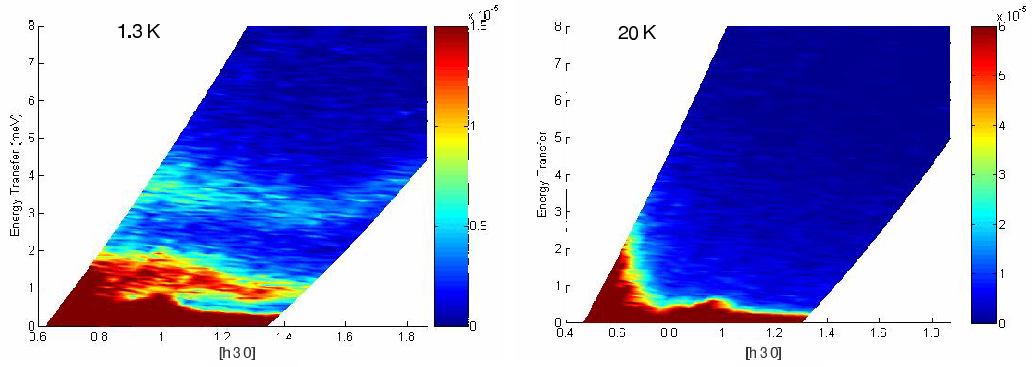

Figure 5.10: Inelastic PRISMA measurements collected at a base temperature of 1.3 K in the commensurate C' phase and in the paramagnetic phase at 20 K. The measurements were taken along the [h 3 0] direction and centred on the (1 3 0) Bragg peak. The contribution from the Bragg peak can be seen at both temperatures but the magnetic excitations are only observable at the lower temperature.

with $\mathbf{k}_f$=1.55 Å^{-1} and some at $\mathbf{k}_f$=1.30 Å^{-1}. A vertically focusing monochromator and horizontally focusing analyser were used with a Be filter on $\mathbf{k}_f$, cooled to 77 K. The width of the incoherent elastic scattering from the crystal was approximately 0.25 meV. All measurements were performed in the W configuration.

A 48 mm long crystal piece of volume 2 cm^3 was used. This crystal was an improvement upon the crystal used for the PRISMA experiment. No twinning was visible and the mosaic spread was found to be approximately 0.8°. The scattering plane used was [h k 0], and the energy range was 0 to 6 meV. The sample was mounted in an Orange Cryostat capable of reaching 1.3 K. Figure 5.11 shows a comparison of the excitations observed around the (1 3 0) Bragg peak at decreasing temperatures. At the base temperature of 1.3 K the excitations are clearly strongest, but evidence for the appearance of the excitations can also be seen at the intermediate temperature of 7.5 K.

Multiple excitations were observed across the Brillouin zone in both available directions. The shape of the Brillouin zone in the [h k 0] plane is demonstrated in

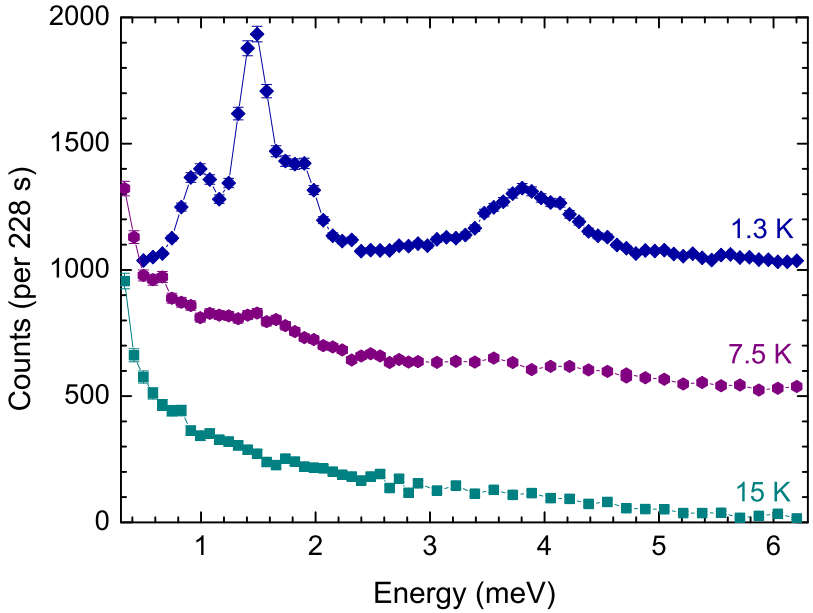

Figure 5.11: A comparison of the excitations observed in the different magnetic phases of $Ni_3V_2O_8$. The energy scans were centred on the Brillouin zone centre (1 3 0) using the 4F2 spectrometer at the LLB. The upper scans have been offset for clarity by 550 counts each.

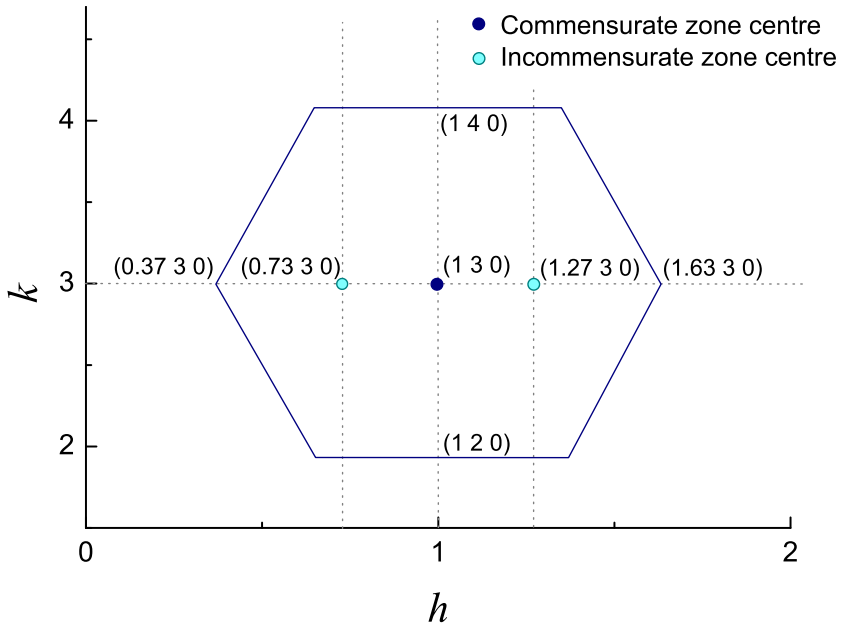

Figure 5.12: The Brillouin zone of $Ni_3V_2O_8$ in the [h k 0] plane. Magnetic excitations were investigated along the [1 k 0] and [h 3 0] directions between the zone centres and boundaries.

Figure 5.12. Shown in Figure 5.13 are the best Gaussian fits to the excitations observed in the [1 k 0] direction at 1.3 K. A flat background contribution was also fitted. Four excitation branches are clearly visible in this direction. The zone centre is at (1 3 0) and the boundary is at (1 2 0). The evolution of the excitations is demonstrated more clearly in Figure 5.14 where the dispersion is also plotted. The dispersion shows that the observed gap of approximately 1 meV for $Ni_3V_2O_8$ is about 75% of the equivalent value for $Co_3V_2O_8$. The dispersion in $Ni_3V_2O_8$ is, however, only approximately 40% of that found in $Co_3V_2O_8$ for this direction of scan. The direction of the scan (k) is perpendicular to the buckled Kagomé planes, the direction in which one might expect the interactions to be weakest and fewer. A dispersion that can be modeled with fewer interactions might be expected along this direction. The energies of all observed excitations are given in Table 5.4.

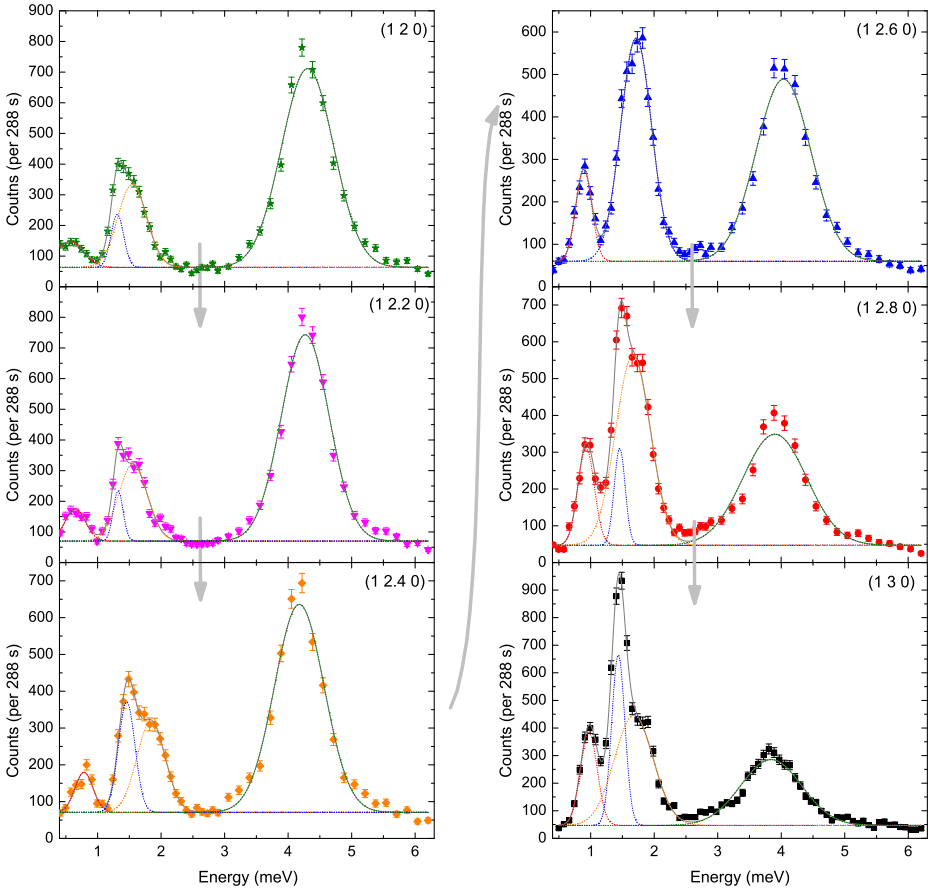

Figure 5.13: Magnetic excitations observed in $Ni_3V_2O_8$ across the Brillouin zone in the [1 k 0] direction using the 4F2 spectrometer at the LLB. The energy scans were all performed at 1.3 K. The observed excitations have been fitted with Gaussian functions. The energies of all excitations are given in Table 5.4.

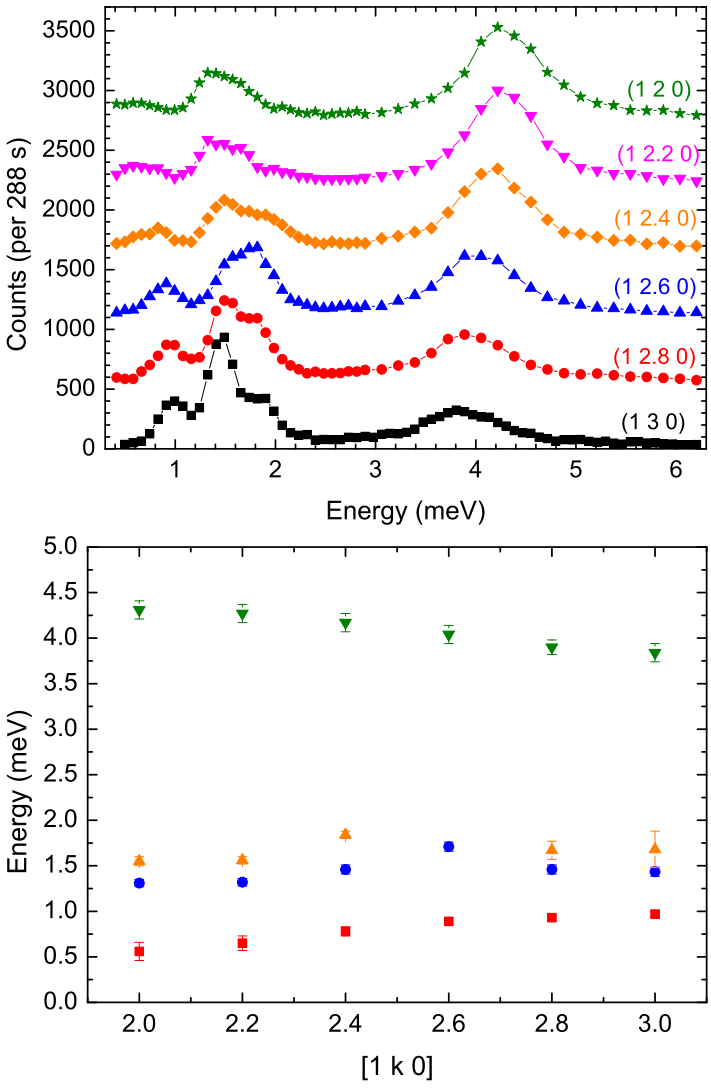

Figure 5.14: Upper: Magnetic excitations observed in $Ni_3V_2O_8$ across the Brillouin zone in the [1 k 0] direction using the 4F2 spectrometer at the LLB. The energy scans were all performed at 1.3 K, and have each been offset by 550 counts for clarity. Lower: The dispersion shows the variation in the position of the peaks determined from the fitted functions shown in Figure 5.13. The colour of the points matches the colour of the fitted functions. The energies are given in Table 5.4.

Position		Excitation energies (meV)					χ^2	Back-ground
boundary	(1 2 0)	0.56(10)	1.31(4)	1.55(5)	4.3(1)	-	2.90	63
	(1 2.2 0)	0.65(10)	1.32(4)	1.56(4)	4.3(1)	-	3.74	70
k	(1 2.4 0)	0.78(5)	1.46(5)	1.84(4)	4.2(1)	-	3.03	71
direction	(1 2.6 0)	0.89(3)	1.71(5)	-	4.0(1)	-	2.90	60
	(1 2.8 0)	0.93(3)	1.459(5)	1.7(1)	3.90(8)	-	4.44	47
centre	(1 3 0)	0.97(2)	1.43(1)	1.68(4)	3.8(1)	-	2.80	47
centre	(1 3 0)	0.97(2)	1.43(1)	1.68(4)	3.8(1)	-	2.80	47
	(1.1 3 0)	1.01(4)	1.40(1)	1.7(4)	3.8(1)	-	3.50	42
h	(1.2 3 0)	0.91(4)	1.27(2)	1.76(4)	3.6(2)	-	2.23	35
direction	(1.3 3 0)	0.82(8)	1.17(8)	1.7(1)	3.4(1)	-	2.20	29
	(1.4 3 0)	0.7(1)	1.1(1)	1.6(4)	3.2(1)	-	1.87	29
	(1.5 3 0)	0.85(4)	1.19(6)	1.57(10)	2.7(1)	3.4(2)	1.97	26
boundary	(1.63 3 0)	0.72(2)	1.20(2)	1.74(10)	3.3(2)	-	1.15	23

Table 5.4: The energies of the observed magnetic excitations in $Ni_3V_2O_8$. The fitted data from which these positions are taken are shown in Figures 5.13 and 5.15. The numbers in brackets are the errors in the last decimal place of the associated numbers.

Across the Brillouin zone in the [h 3 0] direction, five excitation branches were observed (Figure 5.15). The zone boundary in this direction is (1.63 3 0) and the same centre (1 3 0) was used, again studied at 1.3 K. The Brillouin zone is shown in Figure 5.12. The evolution of the excitations is again best observed in the combined plot shown in Figure 5.16. In this direction the lower energy excitations are considerably flatter - the maximum dispersion at approximately 0.3 meV is only around 50% of the energy gap. The dispersion observed in $Co_3V_2O_8$ in this direction is also much flatter. The direction of this scan is within the plane of the buckled Kagomé structure. Along this direction, the symmetry related spine sites are closely positioned and the interactions are antiferromagnetic. The spine site atoms are also each close to two cross-tie sites which align ferromagnetically with themselves. The close proximity of so many magnetic atoms implies a complex collection of interactions in this direction of investigation. The exact positions of the excitations observed are given in Table 5.4.

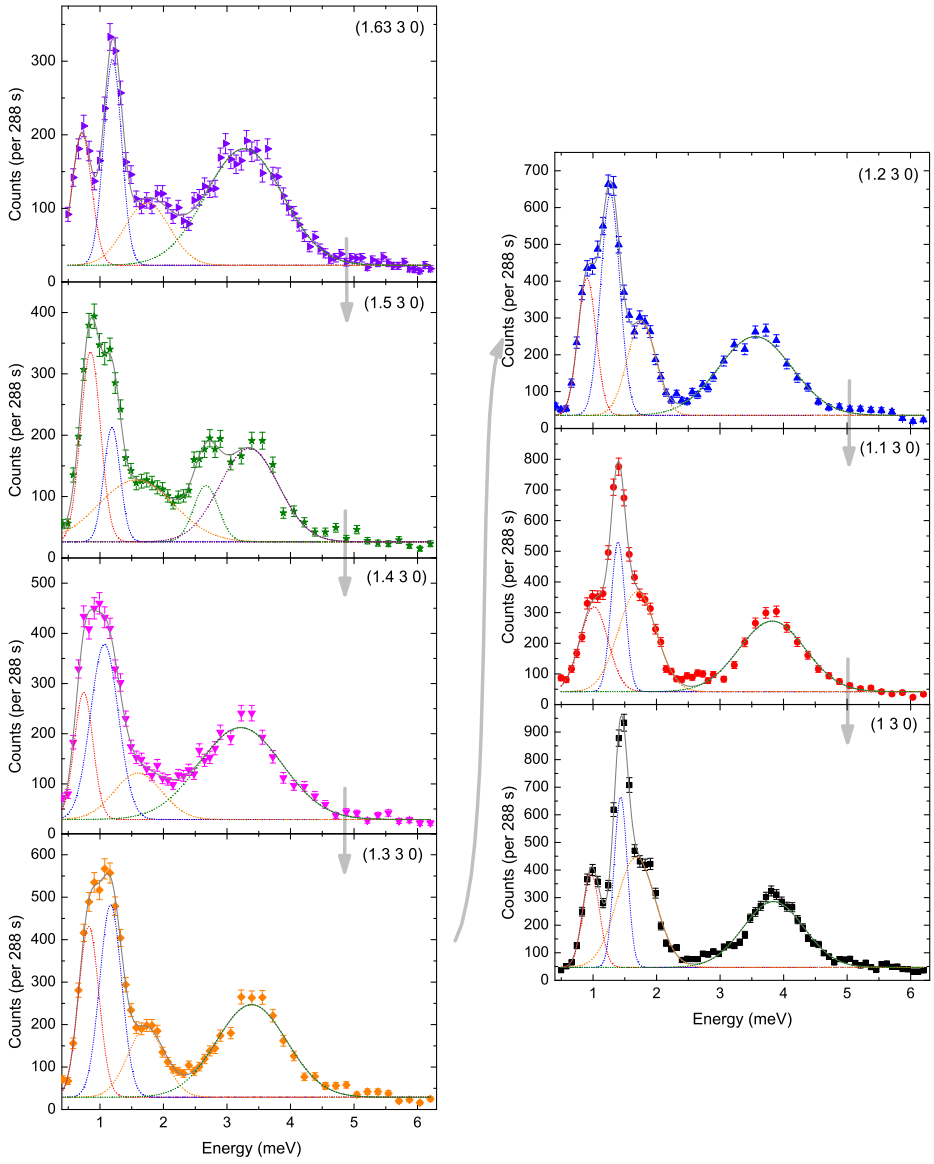

Figure 5.15: Magnetic excitations observed in $Ni_3V_2O_8$ across the Brillouin zone in the [h 3 0] direction using the 4F2 spectrometer at the LLB. The energy scans were all performed at 1.3 K. The observed excitations have been fitted with Gaussian functions. The energies are given in Table 5.4.

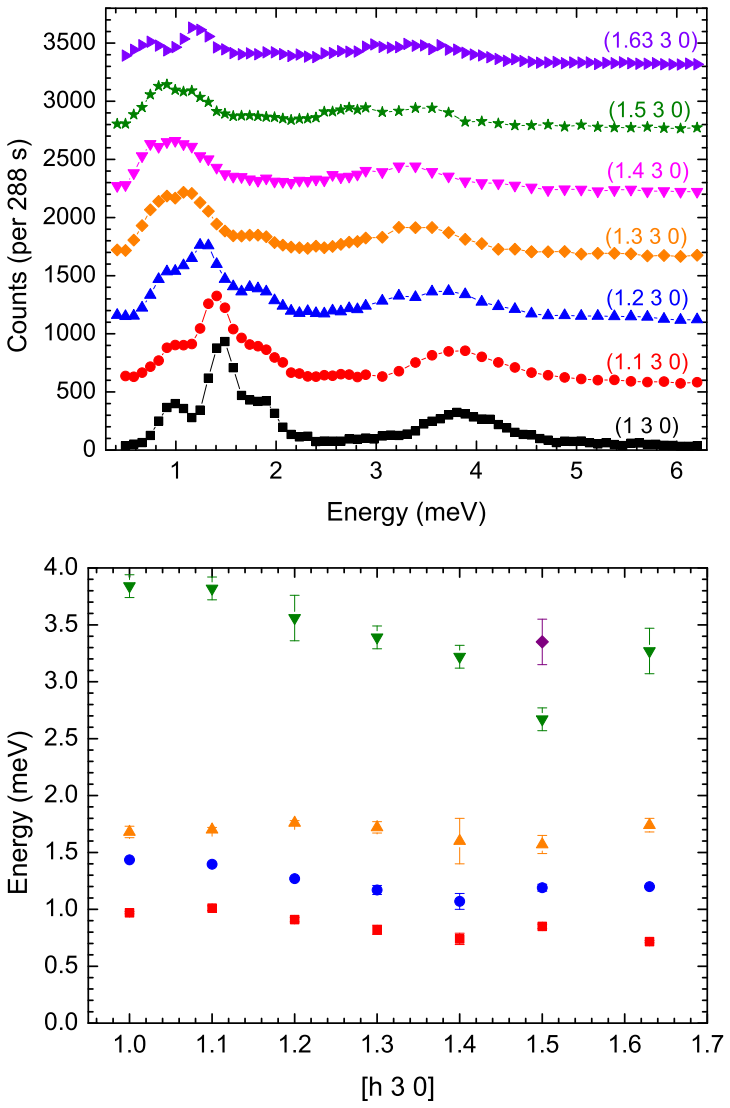

Figure 5.16: Upper: Magnetic excitations observed in $Ni_3V_2O_8$ across the Brillouin zone in the [h 3 0] direction using the 4F2 spectrometer at the LLB. The energy scans were all performed at 1.3 K, and have each been offset by 550 counts for clarity. Lower: The dispersion shows the variation in the position of the peaks, determined from the fitted functions shown in Figure 5.15. The colour of the points matches the colour of the fitted functions. The energies are given in Table 5.4.

Measurements were also taken at 7.5 K in the HTI phase of the material. Figure 5.17 shows the change in the excitation spectrum across the Brillouin zone in the [h 3 0] and [0.73 k 0] directions from the incommensurate zone centre (0.73 3 0). Excitations clearly exist in this temperature region, but are much less intense and well defined than in the low temperature region. From this data, it is also clear that the quasi-elastic scattering contribution is not constant across the Brillouin zone. This is most clear when looking at the crossing of the Brillouin zone in the k direction, as shown in Figure 5.18. As the scan moves away from the zone centre in k, the quasi-elastic contribution significantly reduces. In the h direction, the quasi-elastic contribution remains almost constant.

Figure 5.19 shows the intensity of quasi-elastic scattering as a function of temperature. This was measured at the position (0.9 3 0), close enough to the Bragg peak at the zone centre to see a significant contribution but far enough away so as not to be measuring the Bragg peak itself. The scattered intensity drops sharply when the temperature reduces to 4 K. This is the temperature of the first order transition between the LTI and C phases. Such quasi-elastic scattering is an indicator of magnetic disorder in the sample. The magnitude of the magnetic moments in this phase from powder neutron diffraction indicate that the moments are not fully saturated. In fact, in the incommensurate phases one site has moments that are negligible. In the predominantly collinear low temperature phases the moments on both sites are much larger. It is clear that the disorder disappears sharply with the transition to the collinear state.

Despite the slight differences in structures proposed here from those predicted by Lawes *et al.* [27], the progression of the magnetic structure as temperature decreases still fits with Lawes' predictions of a mean-field treatment. This progression found from neutron diffraction - a modulated antiferromagnetic structure leading to a predominantly collinear antiferromagnetic state - is supported by the dramatic changes observed with inelastic scattering at the 4 K transition temperature. Overall, the data gathered combine to show the complexity of the phase diagram of $Ni_3V_2O_8$.

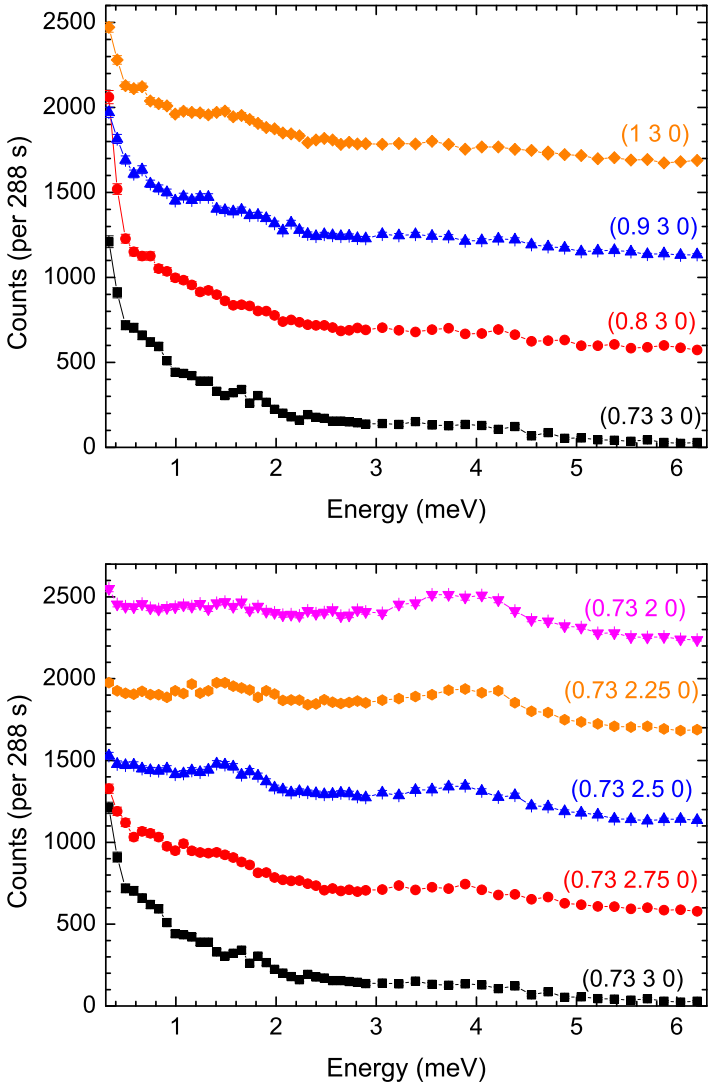

Figure 5.17: Magnetic excitations observed in $Ni_3V_2O_8$ across the Brillouin zone from the incommensurate zone centre (0.73 3 0), in the [h 3 0] (upper panel) and [0.73 k 0] (lower panel) directions. These figures demonstrate the $\mathbf{Q}$ dependence of the quasi-elastic scattering. Along the [h 3 0] direction the quasi-elastic contribution is almost constant, whereas along [0.73 k 0], the contribution drops off sharply when heading away from the zone centre. The energy scans were all performed at 7.5 K and the upper plots have each been offset by 550 counts for clarity.

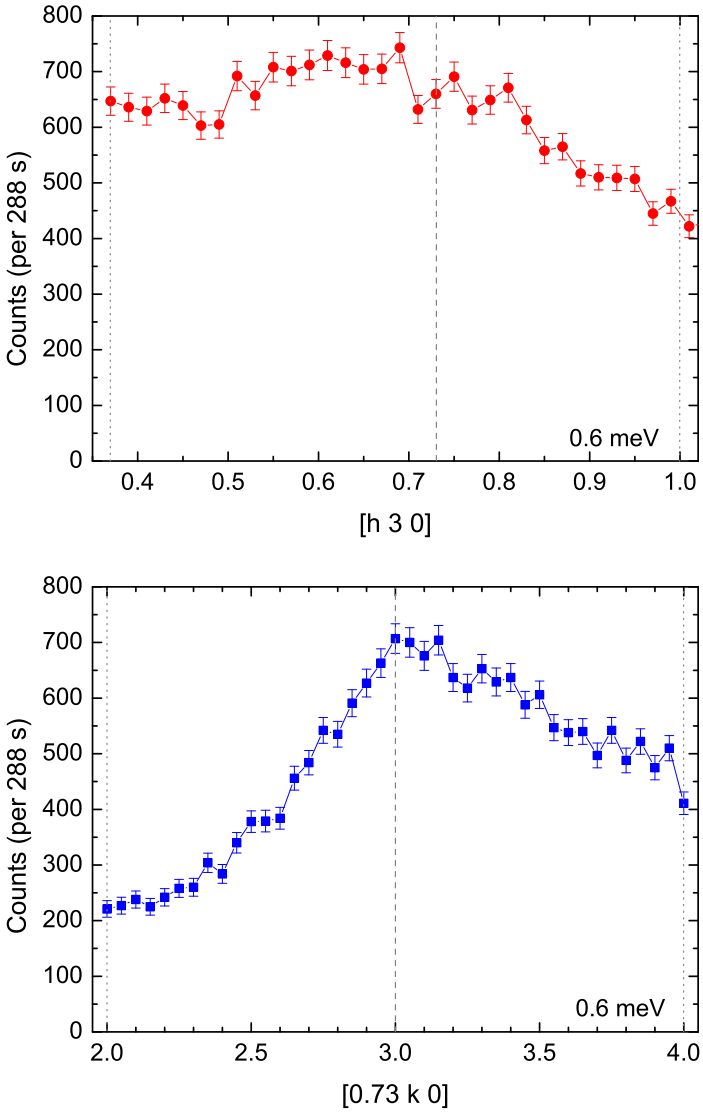

Figure 5.18: $\mathbf{Q}$ dependence of the quasi-elastic scattering observed in $Ni_3V_2O_8$. The measurements were all performed at 0.6 meV and 7.5 K. Measurements were taken from one Brillouin zone boundary (dotted line), across the zone centre (dashed line), to the other boundary.

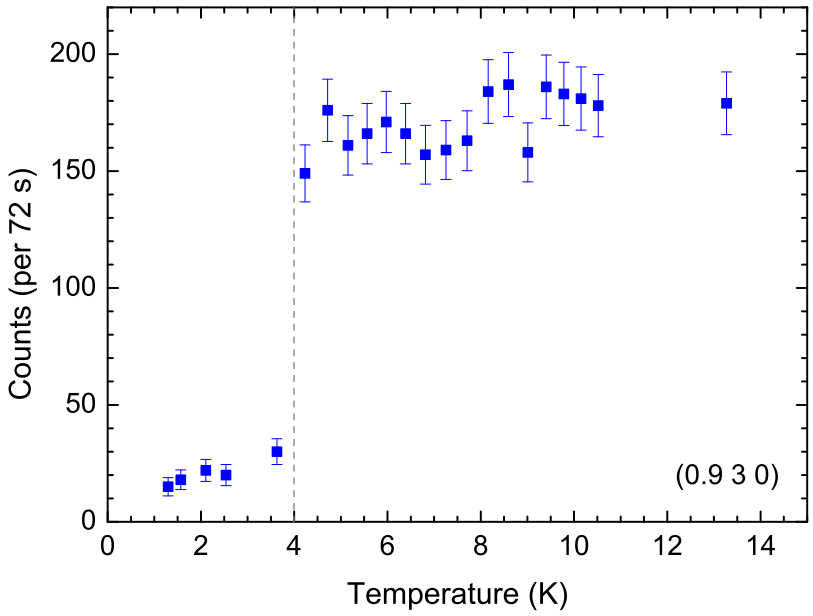

Figure 5.19: Temperature dependence of the quasi-elastic scattering observed in $Ni_3V_2O_8$. The measurements were all performed at the position [0.9 3 0], offset from the Brillouin zone centre [1 3 0]. The dashed line is placed at 4 K - the temperature of the transition from the LTI to the C phase.

5.5 Summary

High quality large samples of $Ni_3V_2O_8$ have been grown with the floating zone technique. The quality of the samples was checked using powder X-ray diffraction, the X-ray Laue technique and EDX on the polished single crystal. The results showed the samples to all be of very high quality, with no observed impurities.

The magnetic phase diagram of the compound was previously presented [27] but has been extended here in magnetic field to show a new boundary that closes the low temperature incommensurate phase when the magnetic field is applied along the a-axis. Also added to the phase diagram for a field applied along the a-axis was the low temperature transition between the C and C' phases. The remainder of the phase diagram shows that four magnetic phases exist in this material in applied fields of up to 120 kOe. The phase transitions were found to be at 9.1, 6, 4 and 2 K. On cooling, the material is paramagnetic then enters the high temperature incommensurate phase (HTI), next is the low temperature incommensurate phase (LTI), then a commensurate antiferromagnetic phase (C), and finally a very similar commensurate phase (C') where a slight elongation of the magnetic moments is observed.

Powder neutron diffraction has been refined in the HTI, C and C' phases of the material. The proposed structures have been presented and show that the first magnetically ordered state is modulated along the a-axis where one of the two Ni sites has a negligible magnetic moment. In a first order phase transition, the magnetic structure becomes commensurate and both Ni sites are ordered. However, one site remains partially disordered with a reduced magnetic moment. Investigation of the structure in high applied fields [25] shows that saturation is still not achieved by 80 kOe.

Inelastic neutron scattering measurements show a significant quasi-elastic scattering contribution that disappears on reducing the temperature past the transition to a commensurate structure. This is the same temperature at which the powder diffraction refinements have shown that the magnetic moments on the previously disordered cross-tie site now posses a reasonable magnitude.

These inelastic measurements have shown up to five excitation branches to exist below 6 meV. The energy gap is small but the observed dispersion is also small. There are 12 magnetic atoms per unit cell, and the separations between the buckled Kagomé layers are not much more than between atoms in the same layer. A complex group of interactions is expected and a detailed model would be required to fit this data. Significant differences in magnetic structures exist between the compounds $Co_3V_2O_8$ and $Ni_3V_2O_8$. A model may help to expose the reasons for these differences.

Chapter 6

Thesis overview

When this thesis work was started, there were only two publications on the properties of the Kagomé staircase materials [22, 26]. Just three years later, a search for publications produces around 20 results. These materials have proved not only to be extremely captivating in terms of their magnetic properties, their dielectric properties have also attracted considerable interest. Here has been presented a study of the magnetic properties of two Kagomé staircase systems: $Co_3V_2O_8$ and $Ni_3V_2O_8$. The structure of the magnetic atoms in these materials is not purely two dimensional, the Kagomé layers are buckled in and out of the plane. This variation means that the symmetry of the system is reduced and further neighbour interactions are much more significant. These structural changes partially relieve the geometric frustration and allow long-range order to be established.

These materials have been produced as high purity powders and very high quality large single crystals. All of the data gathered here combine to show the complexity of these systems. Magnetisation measurements have been used to produce the magnetic field vs temperature phase diagram of $Co_3V_2O_8$. A complex series of transitions is observed, with at least four distinct magnetic phases. Magnetisation measurements show the sample to be highly anisotropic - the susceptibility varies by a factor of almost 100 between the easy a-axis and the hard b-axis.

Powder and single crystal neutron diffraction studies have allowed the magnetic structures to be refined using the FullProf program. The system has two main phases below 11 K: a spin density wave structure with $\mathbf{k} = (0,\ \delta,\ 0)$, where δ varies around $\frac{1}{2}$ above 6 K and a commensurate $\mathbf{k} = 0$ ferromagnetic structure below. The magnetic moment magnitudes of the two Co sites were found to differ by a factor of almost 3 in this phase, and by a factor of almost 2 in the low temperature ferromagnetic phase. In an applied field, the moment magnitude of the cross-tie site is found to increase from this much reduced value to the expected saturation value. During this increase, a re-orientation of all of the Co moments is observed. These results indicate that the application of a magnetic field relieves the frustration on the cross-tie site and that the two Co sites have different anisotropies.

From single crystal diffraction, the narrow region between 5.8 and 6.1 K in zero applied field was found to have Bragg peaks at positions forbidden by c-centring symmetry restrictions. These peaks were found to be magnetic in origin and through Rietveld refinement the magnetic structure was determined. The data was best fit with a combination of two structures with $\mathbf{k} = (0,\ \frac{1}{3},\ 0)$ and $(0,\ 1,\ 0)$. In an applied field, a further magnetic phase was also discovered. It again possessed c-centring symmetry breaking peaks, but with much stronger intensity and with none of the satellite peaks ($\delta = \frac{1}{3}$) observed in the other symmetry breaking phase.

Multiple magnetic excitations have been observed using inelastic neutron scattering measurements on powder and single crystals. Below 5 meV, four excitation branches were observed and a further collection of at least five branches were seen between 10 meV and 68 meV in energy transfer. This data is a significant resource for any work that may be done on a model of the interaction routes and strengths in $Co_3V_2O_8$.

A complete set of similar measurements has also been performed on the compound $Ni_3V_2O_8$. The phase diagram shows that four magnetic phases exist in this material in applied fields of up to 120 kOe. On cooling, the material is paramagnetic then enters the high temperature incommensurate phase, next is the low temperature

incommensurate phase, then a commensurate antiferromagnetic phase, and finally a very similar commensurate phase where a slight elongation of the magnetic moments is observed. The phase diagram of this material has been extended in magnetic field to show a new boundary that closes the low temperature incommensurate phase when the magnetic field is applied along the a-axis.

Powder neutron diffraction data has been refined in the majority of the phases of the material. The proposed structures have been presented and show that the first magnetically ordered state is modulated along the a-axis where one of the two Ni sites has a negligible magnetic moment. In a first order phase transition, the magnetic structure becomes commensurate and both Ni sites are ordered. However, one site remains partially disordered with a reduced magnetic moment. These proposed structures complement the results from inelastic neutron scattering measurements which show a significant quasi-elastic scattering contribution that disappears on reducing the temperature past this transition to a commensurate structure. The inelastic measurements have detected up to five excitation branches below 6 meV. They also show that the quasi-elastic scattering is $\mathbf{Q}$ dependent in the incommensurate phases of the material.

To further the understanding of these materials, high resolution diffraction is required to check for structural distortions at the phase transition temperatures. Particularly for $Co_3V_2O_8$ where less work has been done on the interactions involved, a model of the system would prove invaluable to understanding the complex series of transitions observed in variable fields and temperatures. Further work on this family of materials in the near future will most likely concentrate on the lesser studied $Mn_3V_2O_8$, $Cu_3V_2O_8$ and mixtures, combining Co and Ni for example. It will be very interesting to see how the phase diagrams and magnetic structures of the related materials compare.

Appendix A

Publications

The following publications arising from this thesis are included:

- N. R. Wilson, O. A. Petrenko and L. C. Chapon, *Phys. Rev. B*, 75:094432, 2007.
- N. R. Wilson, O. A. Petrenko and G. Balakrishnan, *J. Phys.: Condens. Matter*, 19:145257, 2007.
- N. R. Wilson, O. A. Petrenko, G. Balakrishnan, P. Manuel and B. Fåk, *J. Magn. Magn. Mater.*, 310:1334, 2007.

Magnetic phases in the Kagomé staircase compound $Co_3V_2O_8$ studied using powder neutron diffraction

N. R. Wilson,[1,*] O. A. Petrenko,[1] and L. C. Chapon[2]
[1]*Department of Physics, University of Warwick, Coventry, CV4 7AL, United Kingdom*
[2]*ISIS Facility, Rutherford Appleton Laboratory, Chilton, Didcot, OX11 0QX, United Kingdom*
(Received 4 October 2006; revised manuscript received 5 January 2007; published 28 March 2007)

The low temperature properties of the Kagomé-type system $Co_3V_2O_8$ have been studied by powder neutron diffraction both in zero field and in applied magnetic fields of up to 8 T. Below 6 K, the zero-field ground state is ferromagnetic with the magnetic moments aligned along the *a* axis. The size of the moment on one of the two Co sites, the so-called cross-tie site, is considerably reduced compared to the fully polarized state. The application of a magnetic field in this phase is found to rapidly enhance the cross-tie site magnetic moment, which reaches the expected value of $\sim 3\mu_B$ by the maximum applied field of 8 T. Different reorientation behaviors are found for the Co cross-tie and spine sites, suggesting a more pronounced easy-axis anisotropy for moments on the spine sites. Rietveld refinements reveal that a simple model, where the spins on both cross-tie and spine sites rotate in the *ac* plane in a magnetic field, reproduces the experimental diffraction patterns well. In addition, it is found that at higher temperatures and moderate magnetic fields, the incommensurate antiferromagnetic order, corresponding to a transverse sinusoidal modulation above 8 K, is suppressed to be replaced by ferromagnetic order.

DOI: 10.1103/PhysRevB.75.094432 PACS number(s): 75.25.+z, 75.50.Ee

I. INTRODUCTION

A Heisenberg antiferromagnet on the two dimensional Kagomé lattice (a net of corner sharing triangles) with only nearest neighbor interactions has an infinitely large number of classical ground states. The system remains a disordered spin liquid down to zero temperature, reflecting this macroscopic degeneracy. Recently, a new class of frustrated magnets, Kagomé staircase oxides, have become a central point of intensive investigations.[1–6] These compounds, of formula $M_3V_2O_8$ (M=Ni, Co or Cu) present an exchange topology closely related to the Kagomé lattice. In these staircase oxides, layers of edge-sharing MO_6 octahedra are separated by nonmagnetic VO_4 tetrahedra. The specific chemical bonding in these materials creates layers of magnetic M^{2+} ions (the V^{5+} ions are nonmagnetic) buckled into a staircase formation—hence the so-called Kagomé staircase lattice.[4] The magnetic layers have lower symmetry than that found in the exact Kagomé lattices which, combined with next-nearest neighbor interactions and possible anisotropic exchange, partially releases the geometrical frustration.

These systems have attracted considerable interest because of the complex sequences of magnetic transitions observed. In particular, the magnetically ordered states for the Ni and Co analogs indicate strongly competing interactions. On lowering the temperature, the Ni system presents two incommensurate phases followed by a commensurate phase with remnant high temperature structures, and a final low-temperature commensurate phase.[5] It was found that inversion symmetry is broken in the low temperature incommensurate cycloidal phase, giving rise to a macroscopic polar vector in a narrow temperature range.[6] This multiferroic behavior has been related to similar effects recently observed in several other frustrated systems such as $TbMnO_3$ (Ref. 7) and $CuFeO_2$,[8] where ferroelectric order is induced by a symmetry breaking process associated with a noncollinear magnetic arrangement.

Very recently, Chen *et al.*[1] have reported a detailed investigation of the magnetic ground state of $Co_3V_2O_8$ by powder and single crystal neutron diffraction. The investigation reveals that on cooling a progressive transition from an incommensurate magnetic order to a ferromagnetic state exists along with a number of lock-in transitions related to commensurate antiferromagnetic order at intermediate temperatures. Contrary to what has been reported based on bulk properties measurements,[2] the magnetic behavior is totally different to what has been observed for the Ni counterpart,[9] suggesting different strengths of the long-range interactions and the magnetic anisotropy.[1]

We report here the results of a powder neutron diffraction study of the antiferromagnetic incommensurate and ferromagnetic structures of $Co_3V_2O_8$ as a function of temperature and magnetic field. The analysis of the data brings to light new aspects of the magnetic properties of this material. In particular, the large magnetic anisotropy and unsaturated Co moments in the ferromagnetic ground state. Our results for the commensurate magnetic phases in zero field are in perfect agreement with those reported by Chen *et al.*[1] We further report the parameters extracted from Rietveld refinement of data in the high-temperature incommensurate region, showing a smooth variation of phase factors in the vicinity of the lock-in transition. In addition, neutron diffraction reveals that both incommensurate and ferromagnetic states are extremely sensitive to the application of a magnetic field. At 9 K, moderate magnetic fields destabilize the incommensurate magnetic state inducing a direct transition to a ferromagnetic state analog to that found in zero-field at low temperatures. A magnetic field applied in the low-temperature ferromagnetic state does not change the periodicity of the magnetic structure. However, the magnetic moment of the Co ion on the cross-tie site that is considerably reduced in the zero-field structure, shows a net increase, eventually saturating at the same value as the Co spine moment. High-field

data at low temperatures can be explained by a spin-reorientation process predominantly in the *ac* plane, with different behaviors for the two Co sites.

II. EXPERIMENTAL

Polycrystalline samples were prepared from the starting materials CoO and V_2O_5.[10] The reagents were thoroughly mixed by grinding and then heated in air to 800 °C for 24 h. The compound was then ground and heated in air at 1050 °C for 24 h, followed by a final grinding. Around 6 g of powder were used for the neutron experiment. Medium resolution neutron powder diffraction experiments were conducted on the GEM (General Materials) diffractometer at the ISIS facility of the Rutherford Appleton Laboratory, UK. Diffraction patterns were collected in zero-field at half degree intervals over the phase transition temperatures, and then at degree intervals over the remaining temperatures between 2 and 12 K. The counting time for each run was approximately 1 h. The diffraction patterns in magnetic fields were collected using a 10 T Oxford Instruments superconducting magnet. Data were recorded at constant temperatures of 2 and 9 K with an increasing magnetic field of 0.5, 1.5, 2.5, 4.0, and 8.0 T. The counting time for each run was approximately 2 h. For in-field experiments, the sample was tightly packed into a vanadium can to avoid reorientation of the crystallites. Rietveld refinements were performed with the FULLPROF program.[11] Possible symmetry arrangements of the low-temperature magnetic structure were determined using representation analysis. The results are presented using Kovalev's notation.[12]

III. RESULTS

A. Zero-field magnetic structure

$Co_3V_2O_8$ was found to order around 11 K, in agreement with previous reports.[1,2,4,10] On cooling, it shows a complex sequence of phase transitions as indicated by the temperature dependence of the neutron diffraction pattern, shown in Fig. 1. These data clearly demonstrate abrupt shifts in the positions and relative intensities of magnetic Bragg peaks. First, incommensurate magnetic ordering sets in with a propagation vector $\mathbf{k}=(0,\delta,0)$, where $\delta=0.54(1)$ at 9.7 K and decreases rapidly to lock at $\delta=\frac{1}{2}$ around 8.0 K. With further cooling, the structure becomes incommensurate again with a rapid decrease of δ. At 5.7 K, a sudden lock-in transition to $\mathbf{k}=(0,0,0)$ is evidenced, again in excellent agreement with recent results.

The temperatures measured in each phase are as follows: The high temperature incommensurate phase (HT_{inc}) includes 10.7, 9.7, and 8.7 K, the high temperature $\delta=\frac{1}{2}$ phase ($HT_{\delta=1/2}$) includes 8.2, 7.7, and 7.2 K, the intermediate phase where δ rapidly decreases includes 6.7 and 6.2 K, and the low temperature ferromagnetic phase (LT_F) includes 5.7 K and below. Due to relatively large temperature steps (1 K) in our experiments, the exact temperature dependence including further lock-in transitions in the intermediate phase as reported by Chen *et al.*[1] could not be precisely mapped out.

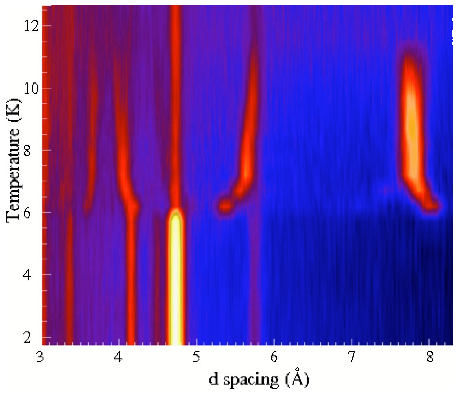

FIG. 1. (Color online) Zero field neutron diffraction pattern of $Co_3V_2O_8$ as a function of temperature. Data from a bank of detectors situated at $2\theta=18°$ are shown and the intensity is color coded.

Rietveld analysis of the magnetic structure has been performed in the HT_{inc} phase, the $HT_{\delta=1/2}$ phase and in the LT_F $\mathbf{k}=0$ phase. In the intermediate temperature range, however, the presence of magnetic Bragg peaks indexed with third order harmonics of the propagation vector complicates the analysis. In particular, the fundamental reflection is only partially observed in the *d*-spacing range accessible from our lowest scattering angle detectors; the large peak occurs at 22.8 Å at 7.2 K and moves up to 25 Å at 6.2 K.

Symmetry analysis of the magnetic structures for the HT_{inc}, $HT_{\delta=1/2}$, and the LT_F phases have been performed using representation analysis. The labeling of atomic positions for cross-tie and spine sites is shown in Fig. 2. Analysis of the magnetic configurations for atomic sites generated from C-centering translation of the labeled positions is not explicitly reported but can be easily calculated by including the phase factor $2\pi\mathbf{k}\cdot\mathbf{T}$ where $\mathbf{T}=(\frac{1}{2},\frac{1}{2},0)$. For the HT structures ($\mathbf{k}=\mathbf{k}_8$ in Kovalev's notation), only the screw axis along *y*, mirror plane perpendicular to *x*, and *b* glide plane

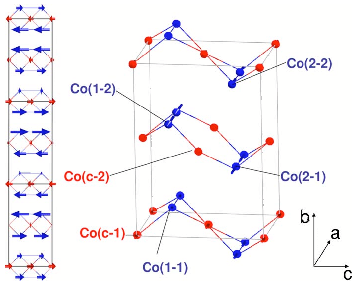

FIG. 2. (Color online) Incommensurate magnetic structure at 9.7 K. Only Co ions on the cross-tie sites and spine sites are shown in red (light gray), and blue (dark gray), respectively. Connections between first neighbor Co atoms are shown as thin solid lines. The right panel displays a single crystallographic unit cell and labels the different atoms related by symmetry (see text for details).

TABLE I. Basis vectors for symmetry-related Co ions of the cross-tie and spine sites belonging to irreducible representations of the little group G_k, *Cmca* with $\mathbf{k}=(0,\delta,0)$, $\phi=\exp(i\pi\mathbf{k})$. Labeling of the atoms follows the conventions shown in Fig. 2. Labeling of the irreducible representations follow Kovalev's notation (Ref. 12).

	Atoms					
Irreps.	Co(c-1)	Co(c-2)	Co(1-1)	Co(1-2)	Co(2-1)	Co(2-2)
Γ_1	$(u_1,0,0)$	$(-u_1,0,0)\phi$	$(0,v_2,0)$	$(0,-v_2,0)\phi$	$(0,v_3,0)$	$(0,-v_3,0)\phi$
Γ_2	$(0,v_1,w_1)$	$(0,v_1,-w_1)\phi$	$(0,v_2,0)$	$(0,v_3,0)\phi$	$(0,v_3,0)$	$(0,v_3,0)\phi$
Γ_3	$(u_1,0,0)$	$(u_1,0,0)\phi$	$(u_2,0,w_2)$	$(u_2,0,-w_2)\phi$	$(u_3,0,w_3)$	$(u_3,0,w_3)\phi$
Γ_4	$(0,v_1,w_1)$	$(0,-v_1,w_1)\phi$	$(u_2,0,w_2)$	$(-u_2,0,w_2)\phi$	$(u_3,0,w_3)$	$(-u_3,0,w_3)\phi$

perpendicular to the z axis are valid operators in the little group.[12] The loss of symmetry operators indicate that the four equivalent positions for the Co spine sites split into two orbits, Co(1-1) with Co(1-2) and Co(2-1) with Co(2-2). The two Co cross-tie site, Co(c-1) and Co(c-2) belong to the same orbit. Basis vectors of the HT magnetic structures are reported in Table I for the four irreducible representations labeled $\Gamma_i(i=1,4)$, all monodimensional. In agreement with the results of Chen *et al.*,[1] we found that only Γ_3 fits the experimental data with modes along the a axis. There is no canting along c within the resolution of our experiment.

Although the Co spine sites split into two orbits, corepresentation analysis including the complex conjugation operator constrain the moment on both orbits to be the same. However, there are no symmetry constraints as such for the phase differences. Therefore, in addition to a global phase factor, set to be 0 on the first Co(c-1) site, there are two phases to be refined describing the relative phasing of the two spin-density waves on the Co(1-1)/Co(1-2) and Co(2-1)/Co(2-2) orbits with respect to the Co(c) wave. These phases, in units of 2π radians, were found to be 0.18(5) and 0.09(5) at 8.2 K where the propagation vector locks at the commensurate value $\delta=\frac{1}{2}$. The results of Ref. 1 can be reproduced by adding a global phase of 0.25 to the values reported here.

On warming the sample the phase values increase and at 10.7 K, where $\delta=0.54$, they reach 0.27(5) and 0.15(5), for the two spin-density waves, respectively. The magnetic structure at 9.7 K in the HT_{inc} phase is presented in Fig. 2. It is similar to that found in the $HT_{\delta=\frac{1}{2}}$ phase, the low-magnetic moments on cross-tie sites are located in layers for which adjacent spine chains are aligned antiferromagnetically. At 8.2 K, the amplitudes of the waves were found to be 1.1(2) and 2.99(2)μ_B on the Co cross-tie and Co spine sites, respectively. Whereas the expected value for high spin Co^{2+} in octahedral configuration (spin only) is achieved on the spine site, there is a marked reduction of the moment on the cross-tie site indicating large fluctuations even in the commensurate $HT_{\delta=1/2}$ phase. At 10.7 K, the amplitudes of the waves decreases to 0.90(18) and 1.99(4)μ_B, respectively.

Next we consider the LT_F magnetic phase. Symmetry analysis is now performed in the group *Cmca* since all symmetry operators belong to the little group for $\mathbf{k}=0$. There are eight one-dimensional representations in this case and the atomic positions for each Co site belong to the same orbit. The projected basis vectors are shown in Table II. Although the transition to the ferromagnetic state is first order and Landau theory does not restrain the magnetic modes to belong to the same irreducible representation in this case, the

TABLE II. Basis vectors for symmetry-related Co ions of the cross-tie and spine sites belonging to irreducible representations of the space group *Cmca*. Labels of the atoms follow the convention shown in Fig. 2. Labeling of the irreducible representations follows Kovalev's notation. The absence of modes for irreducible representations not appearing in the decomposition of the magnetic representation is indicated by the * sign.

	Atoms					
Irreps.	Co(c-1)	Co(c-2)	Co(1-1)	Co(1-2)	Co(2-1)	Co(2-2)
Γ_1	$(u_1,0,0)$	$(-u_1,0,0)$	$(0,v_2,0)$	$(0,-v_2,0)$	$(0,v_2,0)$	$(0,-v_2,0)$
Γ_2	*	*	$(0,v_2,0)$	$(0,v_2,0)$	$(0,-v_2,0)$	$(0,-v_2,0)$
Γ_3	$(u_1,0,0)$	$(u_1,0,0)$	$(u_2,0,w_2)$	$(u_2,0,-w_2)$	$(u_2,0,w_2)$	$(u_2,0,-w_2)$
Γ_3	$(u_1,0,0)$	$(u_1,0,0)$	$(u_2,0,w_2)$	$(u_2,0,-w_2)$	$(u_2,0,w_2)$	$(u_2,0,-w_2)$
Γ_4	*	*	$(u_2,0,w_2)$	$(-u_2,0,w_2)$	$(-u_2,0,-w_2)$	$(u_2,0,-w_2)$
Γ_5	$(0,v_1,w_1)$	$(0,v_1,-w_1)$	$(0,v_2,0)$	$(0,v_2,0)$	$(0,v_2,0)$	$(0,v_2,0)$
Γ_6	*	*	$(0,v_2,0)$	$(0,-v_2,0)$	$(0,-v_2,0)$	$(0,v_2,0)$
Γ_7	$(0,v_1,w_1)$	$(0,-v_1,w_1)$	$(u_2,0,w_2)$	$(-u_2,0,w_2)$	$(u_2,0,w_2)$	$(-u_2,0,w_2)$
Γ_8	*	*	$(u_2,0,w_2)$	$(u_2,0,-w_2)$	$(-u_2,0,-w_2)$	$(-u_2,0,w_2)$

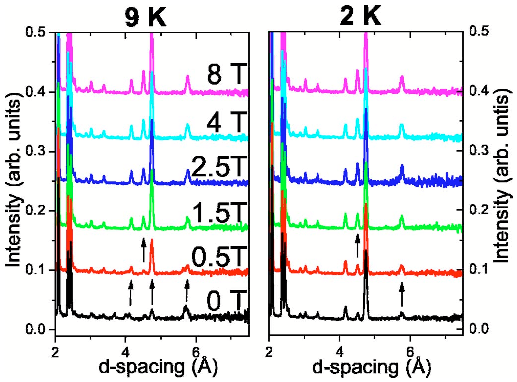

FIG. 3. (Color online) Neutron powder diffraction data at 9 K (left) and 2 K (right) under magnetic fields of 0, 0.5, 1.5, 2.5, 4.0, and 8.0 T. Data from a bank of detectors situated at the scattering angle 35° are shown. The arrows indicate the changes between the data at different fields. Individual curves are offset arbitrarily for display purposes.

data below 5.7 K are consistent with a ferromagnetic structure described by a single representation Γ_3. Similarly to the HT structure, the magnetic moments are directed along the *a* axis. A weak canting along *c*, allowed by symmetry, is not excluded since the data shows a weak hump around the (110) Bragg position. However, the contribution is too small to extract a sizeable component along this direction. The extracted moments at 2 K are $1.81(4)\mu_B$ and $3.04(2)\mu_B$ on the cross-tie and spine sites respectively. Between 2 and 5.7 K, there are no noticeable variations of the magnetic moment. Again, the moment on the cross-tie site is largely reduced with respect to the expected spin contribution of $3\mu_B$, and the average saturated Co moment from magnetization measurements of $3.6\mu_B$.[9]

B. Magnetic structure under magnetic field

To gain further insight into the magnetic behavior of $Co_3V_2O_8$, powder neutron diffraction experiments in magnetic fields have been conducted. First, the field was applied at 9 K where the system is in the HT_{inc} phase. The data are presented in Fig. 3. At 0.5 T, we observe a shift in the positions of magnetic Bragg peaks, indicating a change in propagation vector of 0.02 even at this moderate field value. Simultaneously, new magnetic Bragg peaks appear, indexed at $\mathbf{k}=0$. In particular, we notice a strong increase of the (021) reflection. With further increase of the magnetic field, the incommensurate magnetic state completely disappears, leaving an essentially pure ferromagnetic pattern, similar to that observed for the LT_F structure in zero field. However, the relative intensities of several magnetic Bragg peaks are different from the zero-field data and vary with increasing magnetic field: the (111), (020), (021), and (220) peaks increase continuously between 1.5 and 8 T, suggesting a possible spin reorientation.

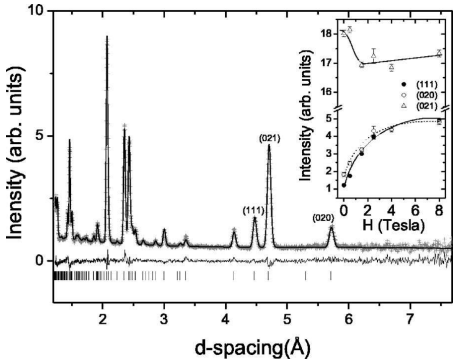

FIG. 4. Rietveld refinement of the nuclear and magnetic structure of $Co_3V_2O_8$ at 2 K, 8 T. Experimental data points and results of the refinement are shown as gray crosses and a thin solid line, respectively. The lower solid line represents the difference curve between experimental and calculated patterns. The positions of Bragg reflections are indicated by tick marks. Inset: Integrated intensities of selected reflections as a function of magnetic field. Curves are guides to the eye.

Applied field neutron diffraction patterns collected in the LT_F state at 2 K are presented in Fig. 3. No additional magnetic reflections appear, indicating that the $\mathbf{k}=0$ structure is stable under application of magnetic fields up to 8 T. However, we observe a redistribution of the scattering intensities (see inset of Fig. 4): the (111) and (020) peaks strongly increase with field. In addition, the integrated intensity of the (111) reflection, increases from being smaller than the (020) integrated intensity at 0 T, to slightly higher at 8.0 T. At the same time, the intensity of the strongest magnetic peak (021) does not vary up to 0.5 T, and only decrease slightly for higher field values.

We initially tried to model the diffraction data in magnetic fields with an identical arrangement to the zero-field LT_F structure, allowing only the magnetic moment on both sites to vary. This model led to an enhancement of the magnetic moments on the Co cross-tie site but failed overall to accurately reproduce the experimental data, resulting in a poor agreement factor for the magnetic phase of $R(F^2)_{mag}=16.80\%$. Subsequent analysis showed that the data are best reproduced with a model in which the spins of both Co sites are allowed to rotate in the *ac* plane. This corresponds to a structure where modes belonging to the irreducible representation Γ_3 along *x* and Γ_7 along *z* are mixed. The agreement with the experiment is very good, as shown in Fig. 4 and a reliability factor of $R(F^2)_{mag}=8.76\%$ is obtained for Rietveld refinement of the data collected at 8 T.

Two essential characteristics can be extracted from the refinement, these are summarized in Fig. 5. Firstly, the magnetic moment on the Co cross-tie site increases rapidly with application of the magnetic field and saturates at $3.15(3)\mu_B$ at 8 T. In zero field the moment magnitude is only 57% of the fully saturated value observed in an applied field of 8 T. The magnetic moment on the Co spine site barely changes with field and is refined at $3.18(2)\mu_B$ at 8 T. Both values

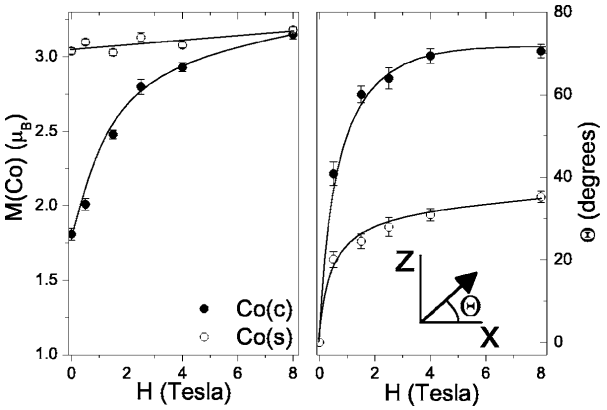

FIG. 5. Dependence of the low-temperature magnetic structure parameters on magnetic field, extracted from Rietveld refinements. Left panel: magnetic moments on the cross-tie site (solid circle) and spine site (open circle). Right panel: angular deviation of spins in the *ac* plane for the cross-tie site (solid circle) and spine site (open circle). $\Theta=0$ corresponds to a collinear structure with spins lying along the *a* axis. Curves are guides to the eye.

agree well with the expected spin-only contribution for high-spin octahedral Co^{2+}. It is clear that one must be cautious when reporting analysis of this kind due to the intrinsic limitations of experiments with polycrystalline samples. However, semiquantitative information can be accessed because a large Q range is probed, a condition not realized for single-crystal instruments due to the geometrical constraints imposed by a cryomagnet.

Secondly, the refinement clearly indicates a reorientation of the spins in the *ac* plane in an applied field. With powder experiments, extracted moment directions are averaged over all possible orientations of the field with respect to the crystal axes, including the *b* axis. From magnetization measurements,[2,9,10,13] it has been shown that the *b* axis of this material is clearly the hard axis. The magnetization is an order of magnitude smaller than that from the *c* axis, which is a further order of magnitude smaller than that of the *a* axis. For an ideal ferromagnetic material for which *a* and *c* are equally easy directions and the *b* axis is perfectly hard, one can expect that the magnetic moments will be fully polarized along the applied field irrespective of the field direction in the *ac* plane. For such an idealized material, a powder measurement integrated over all possible orientations would show an average moment direction pointing at 45° in the *ac* plane. In $Co_3V_2O_8$, however, the moment orientation on the Co spine site is slightly less than the expected 45° value, while the moment orientation angle of the cross-tie site is much higher than expected. From the zero field data presented here, and the magnetization data presented elsewhere,[9] it is clear that the *a* axis is the easy axis of the system. However, on application of a magnetic field, the *c* axis becomes an easier direction than the *a* axis for the Co cross-tie site.

In the LT_F phase, the cross-tie moments are not as large as expected, and lie along the *a* axis parallel to the fully saturated spine site moments. In an applied field of 8 T, the cross-tie moments have reached the expected saturation value and point more along the *c* axis than the *a* axis. The spine site moments have also reorintated to have a larger component along the *c* axis than in zero field, but not as much as the cross-tie moments. This suggests that the single ion anisotropies for the two sites are different and that the application of a field may influence the two moments in different ways.

One should discuss this behavior qualitatively and in the limits of the model approximations, in particular the hypothesis of a perfectly hard direction along *b* (obviously not fulfilled). Overall, these results are in good agreement with magnetization measurements showing that *a* and *c* are definitely easy directions in $Co_3V_2O_8$.[9,10,13] The fact that the moment on the cross-tie site increases rapidly from the reduced $1.81(4)\mu_B$ value is also in agreement with the fully polarized ferromagnetic structure observed in magnetization measurements in moderate magnetic fields. The slightly different anisotropies for both Co sites, suggested by our neutron experiments, could explain the different magnetic behaviors observed when the field is applied along *c* or *a*.

IV. CONCLUSION

Powder neutron diffraction studies have been performed in zero and applied magnetic fields of up to 8 T on the Kagomé staircase oxide $Co_3V_2O_8$. The magnetic structures in the system have been refined using the FULLPROF program. The system has two main phases below 11 K: a spin density wave structure with $\mathbf{k}=(0,\delta,0)$, where δ varies around $\frac{1}{2}$ above 6 K and a commensurate $\mathbf{k}=0$ ferromagnetic structure below. In an applied field, the moment magnitude of the cross-tie site (one of two Co sites) is found to increase from a much reduced value to the expected saturation value. During this increase, a reorintation of all of the Co moments is observed. These results indicate that the application of a magnetic field relieves the frustration on the cross-tie site and that the two Co sites have different anisotropies.

ACKNOWLEDGMENTS

We are grateful to B Fåk for useful discussions and to the EPSRC for financial support.

*Electronic address: Nicola.R.Wilson@warwick.ac.uk

[1] Y. Chen, J. W. Lynn, Q. Huang, F. M. Woodward, T. Yildirim, O. Entin-Wohlman, and A. B. Harris, Phys. Rev. B **74**, 014430 (2006).

[2] R. Szymczak, M. Baran, R. Diduszko, J. Fink-Finowicki, M. Gutowska, A. Szewczyk, and H. Szymczak, Phys. Rev. B **73**, 094425 (2006).

[3] M. Kenzelmann A. B. Harris, A. Aharony, O. Entin-Wohlman, T. Yildirim, Q. Huang, S. park, G. Lawes, C. Broholm, N. Rogado, R. J. Cava, K. H. Kim, G. George, and A. P. Ramirez, Phys. Rev. B **74**, 014429 (2006).

[4] N. Rogado, G. Lawes, D. Huse, A. Ramirez, and R. Cava, Solid State Commun. **124**, 229 (2002).

[5] G. Lawes, M. Kenzelmann, N. Rogado, K. H. Kim, G. A. George, R. J. Cava, A. Aharony, O. Entin-Wohlman, A. B. Harris, T. Yildirim, Q. Z. Huang, S. Park, C. Broholm, and A. P. Ramirez, Phys. Rev. Lett. **93**, 247201 (2004).

[6] G. Lawes, A. B. Harris, T. Kimura, N. Rogado, R. J. Cava, A. Aharony, O. Entin-Wohlman, T. Yildirim, M. Kenzelmann, C. Broholm, and A. P. Ramirez, Phys. Rev. Lett. **95**, 087205 (2005).

[7] A. B. Harris, J. Appl. Phys. **99**, 08E303 (2006).

[8] T. Kimura, J. C. Lashley, and A. P. Ramirez, Phys. Rev. B **73**, 220401(R) (2006).

[9] N. R. Wilson, O. A. Petrenko, and G. Balakrishnan, J. Phys.: Condens. Matter **19**, 145257 (2007).

[10] G. Balakrishnan, O. A. Petrenko, M. R. Lees, and D. M. Paul, J. Phys.: Condens. Matter **16**, L347 (2004).

[11] J. Rodriguez-Carvajal, Physica B **192**, 55 (1993).

[12] O. V. Kovalev, *Irreducible Representations of the Space Groups* (Gordon and Breach, New York, 1965).

[13] Reference 10 uses a different notation to this paper and to Ref. 2 for labeling axes, the space group *Acam* was used so the *c* and *a* axes are swapped.

IOP PUBLISHING JOURNAL OF PHYSICS: CONDENSED MATTER

J. Phys.: Condens. Matter **19** (2007) 145257 (6pp) doi:10.1088/0953-8984/19/14/145257

Magnetic phase diagrams of the Kagomé staircase compounds $Co_3V_2O_8$ and $Ni_3V_2O_8$

N R Wilson, O A Petrenko and G Balakrishnan

Department of Physics, University of Warwick, Coventry CV4 7AL, UK

E-mail: nicola.r.wilson@warwick.ac.uk

Received 5 September 2006
Published 23 March 2007
Online at stacks.iop.org/JPhysCM/19/145257

Abstract

An extensive low temperature magnetization study of high quality single crystals of the Kagomé staircase compounds $Ni_3V_2O_8$ and $Co_3V_2O_8$ has been performed, and the H–T phase diagrams have been determined from these measurements. The magnetization and susceptibility curves for $Co_3V_2O_8$ are analysed in terms of their compatibility with the different ferromagnetic and antiferromagnetic structures proposed for this compound. For $Ni_3V_2O_8$, the phase diagram is extended to magnetic fields higher than previously reported; for a field applied along the a axis, the low temperature incommensurate phase is found to close at around 90 kOe.

1. Introduction

The magnetic effects caused by the Kagomé type lattice have interested theorists and experimentalists for many years. The two dimensional layers of corner sharing triangles possess macroscopic degeneracy when each vertex is occupied by a Heisenberg spin interacting antiferromagnetically with its nearest neighbours. This causes a high degree of magnetic frustration and the system remains a disordered spin liquid down to zero temperature.

Samples that possess a perfect form of this structure are difficult to find, and so experimentalists are turning to structures with variations of the Kagomé lattice. The Kagomé staircase systems $M_3V_2O_8$ [1, 2] with M = Ni, Co or Cu have a structure of magnetic atoms that is based on the Kagomé lattice. Their structure is different in that the layers are not two dimensional but are buckled in and out of the plane. This variation means that the symmetry of the system is reduced and further neighbour interactions are much more significant. These changes partially relieve the frustration and allow long-range order to be established.

The magnetic properties of $Ni_3V_2O_8$ have been characterized using magnetization, specific heat and neutron diffraction techniques [3, 4]. The system passes from a paramagnetic phase to a high temperature incommensurate phase at 9.1 K. The next transition is at 6.3 K where the system enters a low temperature incommensurate phase. At 3.9 K the system then enters a commensurate phase with remnant structures, then finally a purely commensurate

0953-8984/07/145257+06$30.00

antiferromagnetic phase below 2 K. An additional interest in $Ni_3V_2O_8$ is associated with the low-temperature ferroelectricity observed in this compound [5] and the related complex behaviour caused by the magnetoelectric interactions [4].

It has been suggested that the Co system passes through similar phase transitions [6], but our recent neutron powder diffraction study has shown otherwise [7]. At 11 K, $Co_3V_2O_8$ moves from a paramagnetic state to an incommensurate antiferromagnetic state. At 6 K there is a transition to a ferromagnetic state, in which the system remains down to the lowest temperature studied of 1.7 K. The Curie–Weiss temperature for this system is approximately 15 K. Here, we present the temperature and field dependence of the magnetization measured in the various magnetic phases of both compounds for different directions of applied magnetic field. For $Co_3V_2O_8$, the magnetic phase diagram is presented here for the first time and for $Ni_3V_2O_8$, a new phase boundary is shown.

2. Experimental details

The Kagomé staircase compounds $Ni_3V_2O_8$ and $Co_3V_2O_8$, where Ni has $S = 1$ and Co has $S = 3/2$, have the space group *Cmca* with lattice parameters [8] $a = 5.936(4)$ Å, $b = 11.420(6)$ Å and $c = 8.240(5)$ Å for $Ni_3V_2O_8$ and $a = 6.030(4)$ Å, $b = 11.486(2)$ Å and $c = 8.312(5)$ Å for $Co_3V_2O_8$. The atoms form layers of edge-sharing MO_6 octahedra, separated by non-magnetic VO_4 tetrahedra. The samples were prepared using the floating zone technique previously described [9]. Single crystals of both samples of approximately 2 cm^3 in volume were produced with mosaic spreads of less than 1°. An Oxford Instruments Vibrating Sample Magnetometer (VSM) and a Quantum Design SQUID magnetometer were used to measure the temperature and field dependence of the magnetization in these compounds. The samples were investigated with fields applied along each of the three main crystallographic directions, aligned with an accuracy of at least 3°. The phase transitions were tracked in the temperature interval between 1.4 and 12 K in a magnetic field range of up to ±120 kOe.

3. Results and discussion

A range of characteristic magnetization and susceptibility curves measured in $Co_3V_2O_8$ is shown in figure 1. The $M(H)$ curve for a field applied along the easy a axis at 2 K shows a very rapid increase caused by a small field—the magnetic moment is practically saturated at 2 kOe. From the value of magnetization at $H = 80$ kOe, the lower limit for the average Co moment was found to be 3.6 μ_B. From the inset of this figure, it is evident that there is no significant remanent magnetization in zero field (less than 4% of the saturation magnetization) and no significant hysteresis, within the measurement field resolution of 50 Oe. From the neutron diffraction data [7] it has been seen that in the ferromagnetic state the system is not completely ordered; the magnetic moment on one of the two Co sites only has a value of approximately 1.81(4) μ_B. In order to fully understand this magnetization process, one should take into consideration not just the trivial movement of domain walls but also the possible elongation of existing magnetic moments in an applied magnetic field.

In the antiferromagnetic phase at 8 K, it is again very easy to saturate the magnetization. In the small field range before saturation, the system clearly passes through a region of hysteresis centred around 2.7 kOe indicating the presence of an additional phase transition. The phase transitions are also clearly seen as anomalies in the $\chi(T)$ curves at low fields. However, by 6 kOe, the susceptibility curve is very smooth, making it impossible to pin-point the transition temperature. Specific heat measurements may prove more useful for plotting the phase diagram for $H \parallel a$, as has been demonstrated for the $Ni_3V_2O_8$ phase diagram [3].

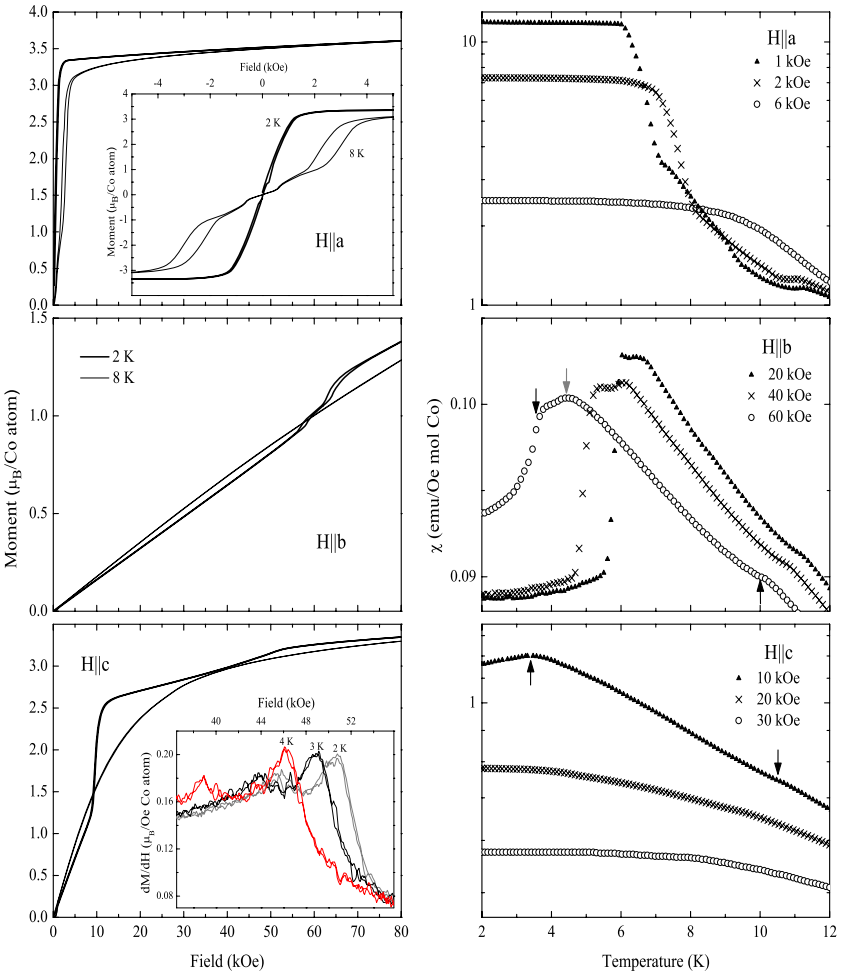

Figure 1. Left panel: characteristic magnetization curves for each of the three main crystallographic directions of $Co_3V_2O_8$. The 2 K data lie within the ferromagnetic phase, and the 8 K data in the antiferromagnetic phase. For $H \parallel a$, the inset of the top panel shows there to be no significant hysteresis around zero field in the ferromagnetic phase (within the 50 Oe field resolution of our measurements) and a considerable hysteresis observed around 2.7 kOe in the antiferromagnetic phase. For $H \parallel c$, the derivatives of magnetization, dM/dH, indicate more definitely the location of phase transition fields, as can be seen in the inset on the bottom panel. Right panel: characteristic susceptibility curves for each of the three main crystallographic directions performed with various applied fields. The black arrows indicate the locations of the paramagnetic to antiferromagnetic or antiferromagnetic to ferromagnetic phase transitions. The grey arrow points to the feature in the $\chi(T)$ curve associated with the locking of the incommensurate antiferromagnetic structure into a particular value of the magnetic propagation vector (see main text for details).

(This figure is in colour only in the electronic version)

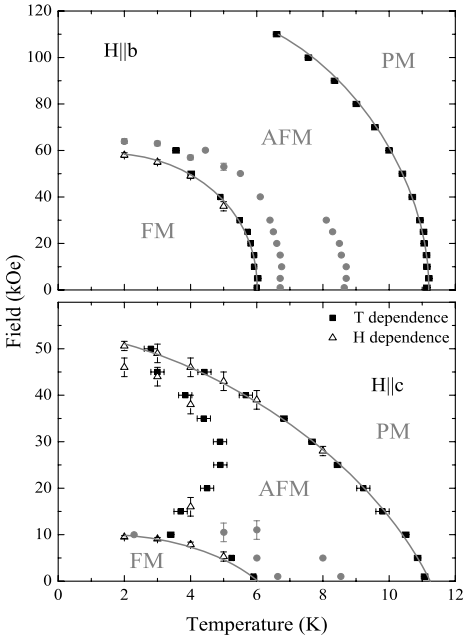

Figure 2. Magnetic phase diagram of $Co_3V_2O_8$ for magnetic field applied along two main crystallographic directions. Magnetization temperature and field curves (closed and open symbols) were used to follow the transitions; lines are plotted as guides to the eye. The grey symbols represent anomalies in the magnetization curves that correspond to the locking and unlocking of the propagation vector within the incommensurate antiferromagnetic phase. Note the different scales of field for each direction.

From the magnetization curves shown for $H \parallel b$, it is obvious that the (010) direction is the hard axis of the system. In a field of 80 kOe, the average magnetic moment is less than 40% of that found for a field applied along the a axis. The $\chi(T)$ curves measured for these two directions differ by a factor of almost 100 [9][1]. In the ferromagnetic phase at 2 K, the $M(H)$ curve shows two step-like hysteretic anomalies at 58 and 64 kOe. These features, and others, are easily followed across $\chi(T)$ curves measured in different applied fields. From comparison with neutron powder diffraction data it is obvious that the anomaly observed at around 11 K corresponds to the transition from a paramagnetic state to an antiferromagnetic state. The neutron data also show that the feature at around 6 K corresponds to the transition from an antiferromagnetic state to a ferromagnetic state. These two transitions are shown by black arrows on the $\chi(T)$ curve measured at 60 kOe. The grey arrow corresponds to an anomaly associated with the unlocking of the propagation vector from (0, 0.5, 0) within the antiferromagnetic phase.

For $H \parallel c$ in the ferromagnetic phase at 2 K, the saturation magnetic moment approaches that for $H \parallel a$. The $M(H)$ curve for $H \parallel c$ shows multiple features at 9.5, 46 and 51 kOe. To

[1] Reference [9] uses a different notation to this paper and to reference [6] for labelling axes; space group *Acam* was used, so the c and a axes are swapped.

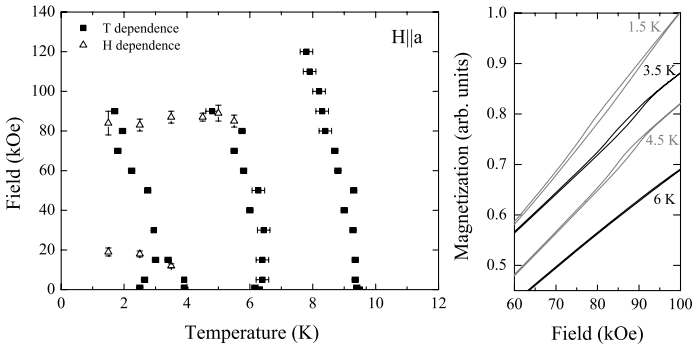

Figure 3. Left panel: magnetic phase diagram of $Ni_3V_2O_8$ for magnetic field applied along the *a* axis. Magnetization temperature curves (solid symbols) and field curves (open symbols) were used to follow the transitions. Right panel: field dependence of the magnetization measured within the low temperature incommensurate phase. The hysteresis apparent at the lower temperatures is no longer observed by 6 K. The curves are offset along the *y* axis for clarity.

observe all of these, the derivative of the magnetization must be considered. These irregularities can also be followed in the $\chi(T)$ curves.

All features observed in the $\chi(T)$ and $M(H)$ curves for $H \parallel b$ and $H \parallel c$ are summarized in the magnetic phase diagram in figure 2. The reduced symmetry and large number of competing interactions in the system contribute to the complex nature of this diagram. It comprises a high temperature paramagnetic phase, an intermediate antiferromagnetic phase and a low temperature ferromagnetic phase. These phases evolve differently as the temperature is reduced and the field increased along different directions. There is added complexity from the anomalies associated with the locking and unlocking of the magnetic propagation vector.

The ordering temperature decreases significantly with applied magnetic field, for $H \parallel c$ for example, $T_N(40\ \text{kOe}) \approx 1/2\ T_N(1\ \text{kOe})$. Such a dramatic decrease in the ordering temperature is unusual even for highly frustrated systems.

A similar range of measurements has been performed on $Ni_3V_2O_8$, confirming the phase diagram reported by Lawes *et al* [3]. The diagram indicates that five phases exist at low temperatures: paramagnetic, high temperature incommensurate, low temperature incommensurate, and two commensurate phases. Along the *b* and *c* axes, the low temperature incommensurate phase is entirely enclosed by 80 and 30 kOe respectively, but open along the *a* axis. Here, figure 3 (left panel) shows the phase diagram for an applied field parallel to the *a* axis with an extension in magnetic field, up to 120 kOe. The $M(H)$ curves collected between 1.5 and 6 K show slight hysteresis at approximately 90 kOe (figure 3 right panel). This is evidence for the closing of the low temperature incommensurate phase not previously reported. In addition to the closing of this phase, the phase diagram here also contains a further phase boundary at around 20 kOe at the lowest temperature. This transition is evident from the large hysteresis observed in the $M(H)$ curves measured below 2 K.

4. Conclusions

The magnetization measurements performed on the Kagomé staircase compound $Co_3V_2O_8$ show there to be no significant net magnetization in zero field or hysteresis in the

low temperature ferromagnetic phase. The transitions from a paramagnetic state to an antiferromagnetic phase, and then to a ferromagnetic phase, are followed in temperature and applied field. The magnetic phase diagram, shown here for the first time, is complicated further by anomalies caused by the locking and unlocking of the propagation vector within the antiferromagnetic phase. The magnetic phase diagram of the closely related compound $Ni_3V_2O_8$ has been extended in magnetic field to show a new boundary that closes the low temperature incommensurate phase when the magnetic field is applied along the *a* axis.

Acknowledgements

We are grateful to L C Chapon and B Fåk for discussion, to M R Lees for reading the manuscript, and to the EPSRC for financial support.

References

[1] Rogado N *et al* 2002 *Solid State Commun.* **124** 229
[2] Rogado N *et al* 2003 *J. Phys.: Condens. Matter* **15** 907
[3] Lawes G *et al* 2004 *Phys. Rev. Lett.* **93** 247201
[4] Kenzelmann M *et al* 2006 *Phys. Rev.* B **74** 014429
[5] Lawes G *et al* 2005 *Phys. Rev. Lett.* **95** 087205
[6] Szymczak R *et al* 2006 *Phys. Rev.* B **73** 094425
[7] Wilson N R, Petrenko O A and Chapon L C 2006 in preparation
[8] Sauerbrei E E, Faggiani R and Calvo C 1973 *Acta Crystallogr.* B **29** 2304
[9] Balakrishanan G *et al* 2004 *J. Phys.: Condens. Matter* **16** L347

Available online at www.sciencedirect.com
ScienceDirect
ELSEVIER
Journal of Magnetism and Magnetic Materials 310 (2007) 1334–1336
Journal of magnetism and magnetic materials
www.elsevier.com/locate/jmmm

Magnetic excitations in the Kagomé staircase compounds

N.R. Wilson[a,*], O.A. Petrenko[a], G. Balakrishnan[a], P. Manuel[b], B. Fåk[c]

[a]*Department of Physics, University of Warwick, Coventry, CV4 7AL, UK*
[b]*ISIS Facility, Rutherford-Appleton Laboratory, Chilton, Didcot OX11 0QX, UK*
[c]*CEA Grenoble, DRFMC/SPSMS, 38054, Grenoble, Cedex 9, France*

Available online 14 November 2006

Abstract

Inelastic neutron scattering measurements have been performed on single crystal samples of $Co_3V_2O_8$ and $Ni_3V_2O_8$. The magnetic system in these compounds is believed to be frustrated, as the magnetic ions (Co^{2+} with $S=\frac{3}{2}$ and Ni^{2+} with $S=1$) adopt a buckled version of the Kagomé lattice. Magnetic excitations have been observed in both samples using a time-of-flight neutron spectrometer. The excitation spectrum is dispersive for both samples and has a considerable gap in the low-temperature phases, while the intermediate temperature phases are marked by a significant softening of the excitations energy.

PACS: 75.30.Ds; 75.50.Dd

Keywords: Frustrated magnet; Kagomé; Neutron scattering

Antiferromagnetic systems based on a Kagomé lattice have traditionally attracted considerable interest from the theoreticians working in the field of frustrated magnetism. The combination of a depleted triangular lattice of loosely connected corner-sharing magnetic moments and the antiferromagnetic sign of the exchange interactions gives rise to enhanced degeneracy of the ground state and to the presence of the macroscopic number of soft modes. These factors destroy a conventional Neél-type magnetic order and result in a spin liquid state. Finding real examples of the 2D Kagomé lattice has proved to be problematic, as the residual 3D or further neighbour interactions, chemical imperfections, as well as lattice distortions and strong magnetic anisotropy tend to stabilise long-range order instead of a spin liquid state. The ground state in such situations is very sensitive to even weak interactions and often displays a complex dependence as a function of temperature and external magnetic field.

Here we report the observation of magnetic excitations in two compounds, $Ni_3V_2O_8$ and $Co_3V_2O_8$, which have recently been reported to adopt a buckled version of the Kagomé lattice called the Kagomé staircase [1]. The lower symmetry of the staircase magnetic layers and further neighbour interactions cause a reduction in the geometrical frustration and establish long-range magnetic order in these magnets. An additional interest in $Ni_3V_2O_8$ is associated with the low-temperature ferroelectricity observed in this compound [2] and the related complex behaviour caused by the magnetoelectric interactions [3].

Large (up to 2 cm^3 in volume) single crystals of $Co_3V_2O_8$ and $Ni_3V_2O_8$ were grown by the floating zone technique, using an infrared image furnace [4]. The measurements of susceptibility and specific heat performed on these samples have shown that they have transition temperatures which agree well the previously reported values [1]. Neutron scattering measurements were performed using the PRISMA time-of-flight inverse geometry crystal-analyser spectrometer at the ISIS pulsed neutron source. The data were collected simultaneously by five double analyser–detector systems measuring five different $Q(\omega)$ lines in reciprocal space. The $Ni_3V_2O_8$ sample was aligned with the c-axis vertical, defining the scattering plane as (h k 0); for the $Co_3V_2O_8$ sample the a-axis was kept vertical, so that the

*Corresponding author. Tel.: +44 247 6522401.
E-mail address: Nicola.R.Wilson@warwick.ac.uk (N.R. Wilson).

0304-8853/$ - see front matter © 2006 Elsevier B.V. All rights reserved.
doi:10.1016/j.jmmm.2006.10.696

scattering plane was (0 k l). The observed intensity has been normalised using a standard vanadium calibration. The experiments were performed in the temperature interval 1.3 to 25 K.

Figs. 1 and 2 show the maps of inelastic neutron scattering (where the intensity is colour coded) measured in the low-temperature phases of $Ni_3V_2O_8$ and $Co_3V_2O_8$ around their respective magnetic zone centres. For $Ni_3V_2O_8$ (see Fig. 1) the measurement is performed along the [h 3 0] direction passing through the magnetic Bragg peak at (1 3 0). At least two excitation branches are clearly seen at $T = 1.3$ K. The lower energy branch (observed around 1 meV) is much more intense than the upper branch at about 3.5 meV. Background measurements performed at $T = 20$ K (the ordering temperature in this compound is 9.1 K [1]) have confirmed that both of these branches are of magnetic origin. Our attempt to find the spin-waves in the high-temperature incommensurate phase of $Ni_3V_2O_8$ was less successful, as the scans performed at $T = 7.5$ K around the (0.73, 3, 0) magnetic Bragg peak have not revealed any excitations of significant intensity.

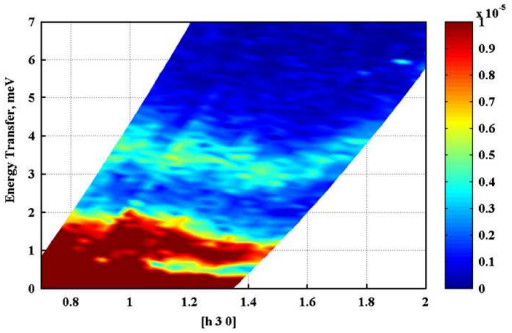

Fig. 1. Map of the inelastic neutron scattering intensity measured at $T = 1.3$ K in a single crystal of $Ni_3V_2O_8$ around a magnetic zone centre (1 3 0).

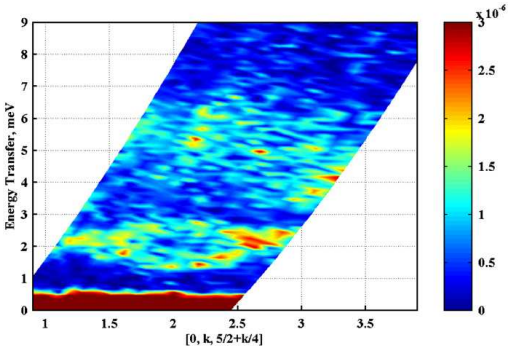

Fig. 2. Map of the inelastic neutron scattering intensity measured at $T = 1.3$ K in a single crystal of $Co_3V_2O_8$ around a magnetic zone centre (0 2 3).

According to the single crystal neutron diffraction measurements [3,5], the low-temperature ground state of $Ni_3V_2O_8$ is a commensurate canted antiferromagnet with the magnetic moments described by a mixture of two irreducible representations. It would be interesting to compare the observed excitation spectrum in this state with the theoretical predictions based on the proposed model of hierarchy of magnetic forces in $Ni_3V_2O_8$ [3,5], which includes nearest and next-nearest exchange, easy-axis anisotropy and Dzyaloshinskii–Moriya interactions.

For $Co_3V_2O_8$, the scans were performed either in the [0 k k] direction around the magnetic (0 4 0) peak or in the direction parallel to the [0 k k/4] line [6] and passing through the ferromagnetic Bragg peak at (0 2 3) (as shown in Fig. 2). According to our powder neutron diffraction measurements [7], the magnetic structure of $Co_3V_2O_8$ at temperatures below 6 K is nearly ferromagnetic with magnetic moments aligned along the a-axis and perhaps slightly tilted (by about 5°) along the c-axis. A peculiar feature of the magnetic ground state is the observed splitting of the two Co^{2+} sites according to the value of average magnetic moment they possess. Two thirds of the Co ions are located in the position $(\frac{1}{4}, y, k/4)$, where $y \approx 0.13$. These ions are labelled as the "spine" sites in Ref. [3] and carry a magnetic moment of 3.1 μ_B. The remaining Co ions reside in the position (0, 0, 0) and are labelled as the "cross-tie" sites. They carry a magnetic moment of only 1.8 μ_B. It is therefore not surprising that the excitation spectrum of $Co_3V_2O_8$ consists of more than one branch. In fact Fig. 2 suggests that four branches of the spin-waves may exist in this compound. For the lowest branch the observed gap at the zone centre is about 1.3 meV. The highest energy of this branch is 2.3 meV at the zone boundary. The relatively small amplitude of the energy variation compared to the gap suggests that the strength of exchange interactions in this compound is comparable with the single-ion anisotropy. This observation is consistent with the results of our earlier measurements of magnetic susceptibility in $Co_3V_2O_8$ [4], where the unusually large difference (up to a hundred times) in $\chi(T)$ was found for different directions of magnetic field.

At intermediate temperatures between 6 and 12 K, $Co_3V_2O_8$ is an incommensurate antiferromagnet with the ordering vector close to $(0\ \frac{1}{2}\ 0)$ [7]. Measurements of the excitation spectrum were attempted at $T = 9$ K around the Bragg peaks (0 2.5 1) and (0 1.5 2). Although the magnetic excitations are still visible, their energy is significantly lower when compared to the ferromagnetic phase, making it difficult to separate the inelastic and quasi-elastic signals. Measurements on an instrument with improved energy resolution would be required for a detailed study of excitations in the antiferromagnetic phase of $Co_3V_2O_8$.

We are grateful to L.C. Chapon for useful discussions. This work is supported by the EPSRC. NRW is grateful to the International Conference on Magnetism 2006 and to

the Institute of Physics C R Barber Trust Fund, Magnetism Group, and Condensed Matter and Materials Physics division for their financial support.

References

[1] N. Rogado, et al., Solid State Commun. 124 (2002) 229.
[2] G. Lawes, et al., Phys. Rev. Lett. 95 (2005) 087205.
[3] M. Kenzelmann, et al., Phys. Rev. B 74 (1) (2006) 014429.
[4] G. Balakrishnan, et al., J. Phys. Condens. Matter 16 (2004) L347.
[5] G. Lawes, et al., Phys. Rev. Lett. 93 (2004) 247201.
[6] It would be more natural to perform a scan along the $[0k0]$ rather than $[0kk/4]$ direction. This scan is however prohibited by the PRISMA instrument's geometry.
[7] N.R. Wilson, O.A. Petrenko, L.C. Chapon, cond-mat/0610098.

Bibliography

[1] J. Needham and W. Ling. *Science and Civilisation in China*, volume 4 part 1 section i. Cambridge University Press, Cambridge, 1962.

[2] J. B. Carlson. *Science*, 189:753, 1975.

[3] S. Blundell. *Magnetism in Condensed Matter*. Oxford University Press, Oxford, 2003.

[4] A. Abragam and B. Bleaney, editors. *Electron Paramagnetic Resonance of transition ions*. Clarendon Press, Oxford, 1970.

[5] D. Craik, editor. *Magnetism principles and applications*. Wiley, Chichester, 1995.

[6] C. Kittel. *Introduction to Solid State Physics*. Wiley, New York, 1986.

[7] I. Dzyaloshinsky. *J. Phys. Chem. Solids*, 4:241, 1958.

[8] J. Goldstone, A. Salam, and S. Weinberg. *Physical Review*, 127(3):965, 1962.

[9] A. P. Ramirez. *Annu. Rev. Mater. Sci.*, 24:453, 1994.

[10] M. F. Collins and O. A. Petrenko. *Can. J. Phys.*, 75:605, 1997.

[11] J. E. Greedan. *J. Mater. Chem.*, 11:37, 2000.

[12] S. T. Bramwell and M. J. P. Gingras. *Science*, 294:1495, 2001.

[13] M. J. Harris, S. T. Bramwell, D. F. McMorrow, T. Zeiske, and K. W. Godfrey. *Phys. Rev. Lett.*, 79(13):2554, 1997.

[14] S. Nagata, P. H. Keesom, and H. R. Harrison. *Phys. Rev. B*, 19(3):1633, 1979.

[15] V. Cannella and J. A. Mydosh. *Phys. Rev. B*, 6(11):4220, 1972.

[16] C. Dekker, A. F. M Arts, and H. W. Wijn. *J. Appl. Phys.*, 63(8):4334, 1988.

[17] S. F. Edwards and P. W. Anderson. *J. Phys. F: Metal Phys.*, 5:965, 1975.

[18] A. S. Wills. *Phys. Rev. B*, 63:064430, 2001.

[19] M. G. Townsend, G. Longworth, and E. Roudaut. *Phys. Rev. B*, 33(7):4919, 1986.

[20] T. Inami, S.Maegawa, and M.Takano. *J. Magn. Magn. Mater.*, 177:752, 1998.

[21] A. S. Wills, A. Harrison, C. Ritter, and R. I. Smith. *Phys. Rev. B*, 61(9):6156, 2000.

[22] G. Balakrishnan, O. A. Petrenko, M. R. Lees, and D. McK Paul. *J. Phys.: Condens. Matter*, 16:L347, 2004.

[23] Y. Chen, J. W. Lynn, Q. Huang, F. M. Woodward, T. Yildirim, G. Lawes, A. P. Ramirez, N. Rogado, R. J. Cava, A. Aharony, O. Entin-Wohlman, and A. B. Harris. *Phys. Rev. B*, 74(1):014430, 2006.

[24] R. Szymczak, M. Baran, R. Diduszko, J. Fink-Finowicki, M. Gutowska, A. Szewczyk, and H. Szymczak. *Phys. Rev. B*, 73:094425, 2006.

[25] M. Kenzelmann, A. B. Harris, A. Aharony, O. Entin-Wohlman, T. Yildirim, Q. Huang, S. Park, G. Lawes, C. Broholm, N. Rogado, R. J. Cava, K. H. Kim, G. Jorge, and A. P. Ramirez. *Phys. Rev. B*, 74(1):014429, 2006.

[26] N. Rogado, G. Lawes, D. A. Huse, A. P. Ramirez, and R. J. Cava. *Solid State Comm.*, 124:229, 2002.

[27] G. Lawes, M. Kenzelmann, N. Rogado, K. H. Kim, G. A. George, R. J. Cava, A. Aharony, O. Entin-Wohlman, A. B. Harris, T. Yildirim, Q. Z. Huang, S. Park, C. Broholm, and A. P. Ramirez. *Phys. Rev. Lett.*, 93:247201, 2004.

[28] G. Lawes, A. B. Harris, T. Kimura, N. Rogado, R. J. Cava, A. Aharony, O. Entin-Wohlman, T. Yilidrim, M. Kenzelmann, C. Broholm, and A. P. Ramirez. *Phys. Rev. Lett.*, 95:087205, 2005.

[29] N. Rogado, M. K. Haas, G. Lawes, D. A. Huse, A. P. Ramirez, and R. J. Cava. *J. Phys.: Condens. Matter*, 15:907, 2003.

[30] N. Qureshi, H. Fuess, H. Ehrenberg, T. C. Hansen, C. Ritter, K. Prokes, A. Podlesnyak, and D. Schwabe. *Phys. Rev. B*, 74:212407, 2006.

[31] E. Morosan, J. Fleitman, T. Klimczuk, and R. J. Cava. *arXiv:cond-mat/0704.1581*.

[32] E. E. Sauerbrei, R. Faggiani, and C. Calvo. *Acta. Cryst.*, B29:2304, 1973.

[33] R. D. Shannon and C. Calvo. *Can. J. Chem.*, 50:3944, 1972.

[34] T. Hahn, editor. *International Tables of Crystallography*. Kluwer Academic Publishers, Dordrecht, The Netherlands, 1995.

[35] N. R. Wilson, O. A. Petrenko, and G. Balakrishnan. *J. Phys.: Condens. Matter*, 19:145257, 2007.

[36] Yusuke Kobayashi, Yukio Yasui, and Masatoshi Sato. *J. Magn. Magn. Mater.*, 310:1160, 2007.

[37] R. Szymczak, M. Baran, R. Diduszko, J. Fink-Finowicki, M. Gutowska, A. Szewczyk, and H. Szymczak. *J. Magn. Magn. Mater.*, 310:094425, 2006.

[38] N. Qureshi, H. Fuess, H. Ehrenberg, T. C. Hansen, and D. Schwabe. *Solid State Comm.*, 142:169, 2007.

[39] Y. Yasui, Y. Kobayashi, M. Soda, T. Moyoshi, M. Sato, N. Igawai, and K. Kakurati. *J. Phys. Soc. Jap.*, 76:034706, 2007.

[40] ZZ. He, T. Taniyama, M. Itoh, and Y. Ueda. *Crystal Growth & Design*, 6:1055, 2007.

[41] N. R. Wilson, O. A. Petrenko, and L. C. Chapon. *Phys. Rev. B*, 75:094432, 2007.

[42] N. R. Wilson, O. A. Petrenko, G. Balakrishnan, P. Manuel, and B. Fåk. *J. Magn. Magn. Mater.*, 310:1334, 2007.

[43] N. Bellido, C. Martin, C. Simon, and A. Maignan. *J. Phys. Condens. Matter*, 19:056001, 2007.

[44] R. P. Chaudhury, F. Yen, C. R. dela Cruz, B. Lorenz, Y. Q. Wang, Y. Y. Sun, and C. W. Chu. *Phys. Rev. B*, 75:012407, 2007.

[45] R. C. Rai, J. Cao, S. Brown, J. L. Musfeldt, D. Kasinathan, D. J. Singh, and G. Lawes. *Phys. Rev. B*, 74:235101, 2006.

[46] A. B. Harris, T. Yildirim, A. Aharony, and O. Entin-Wohlman. *Phys. Rev. B*, 73:184433, 2006.

[47] C. Sudakar, P. Kharel, R. Naik, and G. Lawes. *Phil. Mag. Lett.*, 87:223, 2007.

[48] A. Brooks Harris. *J. Appl. Phys.*, 99:08E303, 2006.

[49] T. Lancaster, S. J. Blundell, P. J. Baker, D. Prabhakaran, and W. Hayes. *Phys. Rev. B*, 75:064427, 2007.

[50] ZZ. He, Y. Ueda, and M. Itoh. *J. Crstal Growth*, 297:1, 2006.

[51] Defa Wang, Junwang Tang, Zhigang Zou, and Junhua Ye. *Chem. Mater.*, 17:5177, 2005.

[52] L. C. Chapon, P. G. Radaelli, G. R. Blake, S. Park, and S.-W. Cheong. *Phys. Rev. Lett.*, 96:097601, 2006.

[53] P. G. Radaelli and L. C. Chapon. *Phys. Rev. B*, 76:054428, 2007.

[54] G. L. Squires. *Introduction to the theory of thermal neutron scattering*. Dover, Mineole, New York, 1996.

[55] L. Dobrzynski and K. Blinowski. *Neutrons and solid state physics*. Ellis Horwood, Hertfordshire, 1994.

[56] H. Dachs, editor. *Neutron diffraction*. Springer, Germany, 1978.

[57] B. D. Cullity and S. R. Stock. *Elements of X-ray diffraction*. Prentice Hall, New Jersey, third edition, 2001.

[58] G. E. Bacon. *Neutron diffraction*. Clarendon Press, Oxford, UK, third edition, 1975.

[59] O. Halpern and M. H. Johnson. *Phys. Rev.*, 55:898, 1939.

[60] G. Cicognani, editor. *The yellow book 2005*. ILL, Grenoble, 2005.

[61] G. Kádár and L. Rosta, editors. *Lecture notes on neutron scattering Introductory course to ECNS'99*. Budapest Neutron Centre and European Neutron Scattering Association, Budapest, 1999.

[62] F. Akeroyd, G. Cross, S. Hills, P. King, S. Payne, D. Sivia, A. Terry, D. Clements, and S. Howells. *The ISIS Facility*. CCLRC, Oxfordshire, UK, 2006.

[63] S. M. Bennington, editor. *Introduction to neutron scattering*. ISIS Facility, Chilton, OXON, 2006.

[64] W. Schäfer, E. Jansen, F. Elf, and G. Will. *J. Appl. Cryst.*, 17:159, 1984.

[65] A. C. Hannon. *Nucl. Instrum. Methods Phys. Res., Sect. A*, 511:88, 2005.

[66] M. J. Harris and M. J. Bull. *PRISMA Single Cold Neutron Spectrometer & Diffractometer User Manual*. ISIS Facility, Oxfordshire, second edition, 1998.

[67] H. M. Rietveld. *J. Appl. Cryst.*, 2:65, 1969.

[68] J. Rodriguez-Carvajal. *Physica B*, 192:55, 1993.

[69] LLB. *Experimental facilities*. CEA and CNRS, Saclay, France, 2003.

[70] J. Laugier and B. Bochu. *Orient Express V3.3*.

[71] Ian M. Watt. *The principles and practice of electron microscopy*. Cambridge University Press, Cambridge, 1997.

[72] P. J. Goodhew and F. J. Humphreys. *Electron microscopy and analysis*. Taylor & Francis, London, second edition, 1992.

[73] M. McElfresh. *Fundamentals of Magnetism and Magnetic Materials*. Quantum Design, 1994.

[74] G. R. Stewart. *Rev. Sci. Instrum.*, 54 (1):1, 1983.

[75] A. Nord, G. Aberg, T. Stefanidis, P. Kierkegaard, and V. Grigoriadis. *Chem. Scr.*, 25:212, 1985.

[76] E. S. R. Gopal, editor. *Specific heats at low temperatures*. Heywood Books for Iliffe Books, London, 1966.

[77] O. V. Kovalev. *Irreducible Representations of the Space Groups*. Gordon and Breach, New York, 1965.

[78] C. Wilkinson, H. W. Khamis, R. F. D. Stansfield, and G. J. McIntyre. *J. Appl. Cryst.*, 21:471, 1988.

[79] L. D. Cussen. *J. Appl. Cryst.*, 35(5):615, 2002.

[80] H. T. Diep, editor. *Magnetic systems with competing interactions (frustrated spin systems)*. World Scientific, Singapore, 1994.